Department of Physics and Astronomy
University of Heidelberg

Diploma Thesis in Physics

Submitted by
Ellen Simmat
born in Berlin, Germany

2009

Infrared Properties of the Halo, Bulge and Disk of the Edge-On Galaxy NGC 7814

This diploma thesis has been written by
Ellen Simmat

at the
Max-Planck-Institut für Kernphysik

under the supervision of
Prof. Hofmann

Infrared Properties of the Halo, Bulge and Disk of the Edge-On Galaxy NGC7814

Abstract

Highly resolved images of the edge-on galaxy NGC 7814 from 2MASS and Spitzer were used to extract the morphologies and spectral energy distributions (SEDs) of the disk, bulge and halo components of this galaxy over a wavelength range from 1.25 to 24 μm. This represents the first direct determination of the mid-infrared emission of the bulge and halo components of a galaxy other than the Milky Way. The SEDs of all three structures imply the presence of emission components from direct stellar light and from at least one further component. For the disk, this further component is interpreted as dust emission having properties typical of star forming disks. The emission from the bulge and the halo is very significantly in excess of that from an extrapolation of the near infrared emission from stars. This excess has a flat spectrum between 8 and 24 μm bands and has an unknown origin. I discuss potential explanations such as dust emission in an interstellar medium, galactic winds, star forming regions and circumstellar dust, as well as emission from brown dwarfs. Further analysis is needed to test these hypotheses.

Zusammenfassung

Die hochaufgelösten Bilder der edge-on Galaxie NGC 7814 von 2MASS und Spitzer wurden verwendet, um Morphologien und SEDs (spectral energy distributions) der Disk, des Bulges und des Halos dieser Galaxie über einen Wellenlaengenbereich von 1.25 bis 24 μm abzuleiten. Dies stellt die erste Detektion der Bulge- bzw. Halokomponente einer anderen Galaxie als der Milchstraße im mittleren Infrarot dar. Die SEDs aller drei Strukturen weisen zum einen auf die Emission von direktem Sternenlicht hin, zum anderen auf das Vorhandensein von mindestens einer weiteren Emissionsquelle. Im Fall der Disk wird diese weitere Emissionsquelle als Staubemission mit typischen Eigenschaften für eine Disk mit Sternentstehung interpretiert. Die Bulge- und Haloemission liegt deutlich über der Extrapolation des Sternenlichts aus dem NIR in den MIR Bereich. Diese zusätzliche Emission hat ein sehr flaches Spektrum zwischen den 8 und 24 μm Bändern und hat eine unbekannte Quelle. Ich diskutiere potentielle Erklärungen wie Staubemission eines interstellaren Mediums, in galaktischen Winden, in Sternentstehungsgebieten oder von sternumhüllenden Staubschalen, als auch die Emission von Braunen Zwergen. Weitere Untersuchungen werden benötigt um die genannten Hypothesen zu verifizieren.

Contents

List of Figures

List of Tables

Chapter 1

Introduction

1.1 Infrared Properties of Galaxies

Due to the limited angular resolution of the infrared (IR) space observatories, IR properties of galaxies are usually analyzed looking at the integrated emission of the whole galaxy (e.g. Dale et al. 2005; Draine et al. 2007). The IRAS, ISO and Spitzer missions have shown that spiral galaxies are dominated by stellar light in the near infrared (NIR; 1-3μm), by thermal dust emission and molecular line emission, such as polycyclic aromatic hydrocarbons at 8μm, in the mid infrared (MIR; 3-30μm) and by thermal dust emission in the far infrared (FIR; 30-300μm). (For reviews for observational and theoretical studies of IR dust emission based on IRAS, ISO and Spitzer see Soifer et al. (1987), Sauvage et al. (2005) or Soifer et al. (2008).)

Elliptical galaxies have little or no neutral or molecular interstellar medium (ISM), traced by radio line emission from HI and molecules such as CO, even though there is evidence for interstellar dust in some objects (Temi et al. 2008). Therefore, they are dominated in all wavelengths by direct stellar light in the optical and the NIR, extending far into the MIR, though there is evidence for an emission component from circumstellar dust as well as collisionally heated dust in the coronal component of the ISM.

Concerning the morphology, spiral galaxies are typically composed of a bulge and a disk component in the optical. The IR counterpart of the disk is well known, while almost nothing is known about the IR bulge. A traditional operational definition of the bulge of a galaxy is a centrally-concentrated stellar distribution with a smooth appearance. This definition excludes all components apart from stars, e.g. dust, gas and even star forming regions, and assigns these phenomena to the central parts of the disk. However, another definition for bulges is the light excess above an inward extrapolation of a constant scale height exponential disk. This definition is not necessarily limited to stellar light only, but can include emission from other sources as well (Wyse et al. 1997).

Bulges are generally believed to be old and metal-rich, as is the case for elliptical galaxies. They are traditionally fitted with a de Vaucouleurs profile ($R^{1/4}$-law). McDonald et al. (2009) made a bulge-disk decomposition in the NIR for 65 Ursa Minor cluster spiral galaxies. They found a wide range of bulge shapes, parameterized with the Sersic parameter n (see Sect. 3.1.1), from bulges in low surface brightness galaxies with $n \lesssim 0.5$ to bulges in the most massive galaxies with $n \gtrsim 6.0$, concluding that the $R^{1/4}$-law (i.e. $n = 4.0$) only holds for few prominent bulges. Fisher et al. (2009) analyzed a sample of face-on nearby galaxies in the MIR and found ongoing star formation towards the bulges for all galaxies in their sample. The orientation of Fisher's sample prevented however a

statement of whether the star formation was really associated with the spheroid structure, or whether it was located in the inner disk. Nevertheless, Fisher's work demonstrates that the traditional view of bulges as being devoid of non-stellar MIR emission may be too naive and must be reviewed.

Moreover, many galaxies show evidence for a third morphological component besides the disk and the (central) bulge. Optical star counts in our Galaxy, such as presented by Larsen & Humphreys (1994), indicate the presence of a more diffuse component, i.e. an outer bulge or halo, extending perpendicular to the plane above the thick disk, which falls off much more shallowly than predicted from traditional bulge profiles. I refer in this thesis to such a component as the "halo". In one instance, there is evidence for a MIR counterpart to an optical halo: Burgdorf et al. (2007) reported a MIR emission above the mid plane of the galaxy NGC 891 which extended out to 20kpc above the plane of the galaxy in their 16μm and 22μm images, which indicates a MIR emission component in the halo.

1.2 Aim of this Thesis

Morphological Bulge-disk decomposition has long been a common tool in the optical regime (e.g. MacArthur et al. 2003; Kent 1985). In the infrared, this technique is by contrast rather uncommon, partly because angular resolution is much poorer, and partly since the bulge emission is traditionally expected to be negligible at these wavelengths due to the lack of an ISM. consequently, while there are several models for the physics behind MIR disk emission (e.g. Popescu & Tuffs 2010, and references therein), the MIR properties of bulges or halos are unknown.

In this thesis, I will make a halo-bulge-disk decomposition of images of a well resolved edge-on galaxy at a series of wavelengths in the NIR and MIR range. From this, I will construct the NIR/MIR spectral energy distributions (SEDs) of each of these components. Finally, I will qualitatively interpret these SEDs in terms of possible sources of the measured emission and I will show that the general assumption of dust-less bulges and halos is not supported for the galaxy studied.

For this work, I choose the galaxy NGC 7814 since I need a highly resolved edge-on disk galaxy in order to morphologically separate the halo, the bulge and the disk at each individual wavelength without making any assumptions of the spectral energy distribution (SED). The edge-on view afforded by NGC 7814 enables me to analyze structure above and below the disk without assuming anything about the disk or the bulge. The high resolution makes it possible to analyze small scale structures such as the central bulge of the galaxy.

1.3 NGC 7814

The galaxy NGC 7814 is an edge-on disk galaxy which has been investigated several times in the optical and the NIR (e.g. Lequeux et al. 1995; Peletier & Knapen 1992; van der Kruit & Searle 1982; Wainscoat et al. 1990; Eskridge et al. 2002). It's equatorial coordinates (J2000.0) are longitude = 0.812042 and lattitude = 16.145417 (Ra: 00h 03m 14.890s, Dec: +16d 08m 43.50s). This galaxy is almost perfectly edge-on, within less than a few tenths of a degree of 90° inclination (van der Kruit & Searle 1982). It has a large,

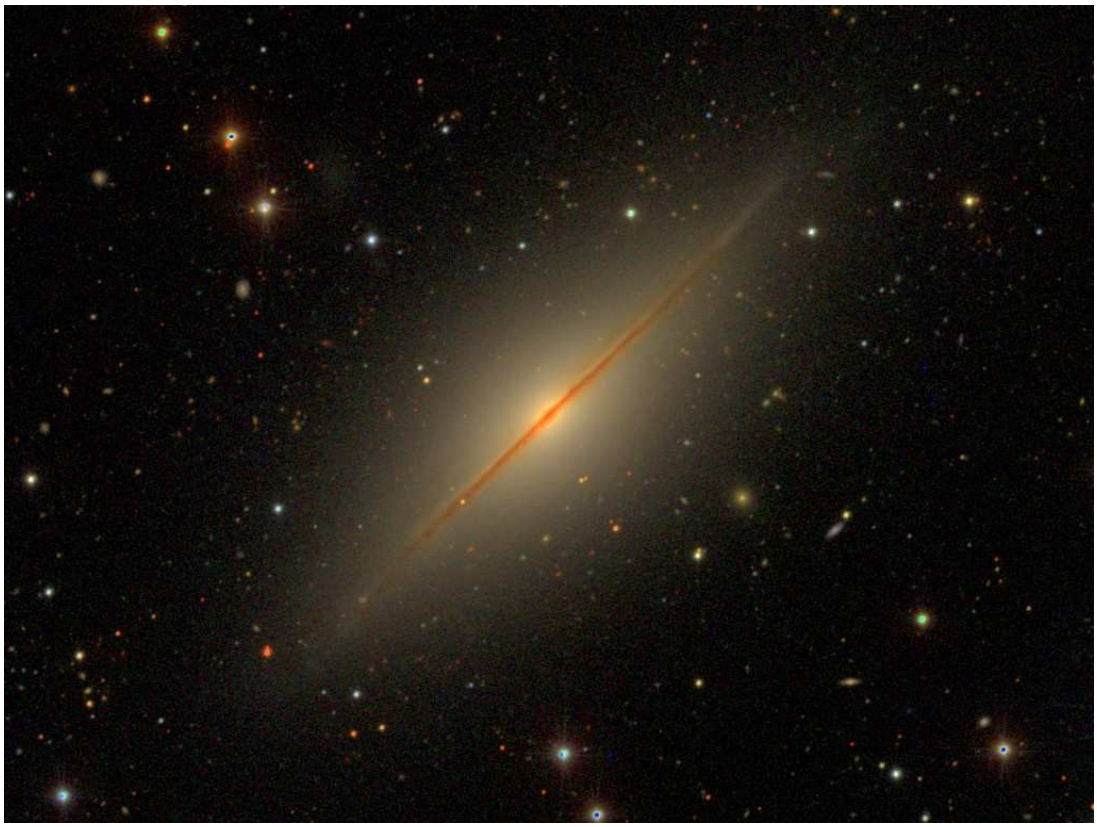

Figure 1.1: SDSS False Color Image of NGC 7814

This false color image of NGC 7814 shows a dusty disk, a central bulge and a diffuse extended "halo".

flattened halo[1] and an active galactic nucleus. Absorption features from the dust lane in the disk can easily be seen in optical images (Eskridge et al. 2002). Fig. 1.1 shows an SDSS (optical wavelengths) false color image of the galaxy NCG 7814.

Due to its edge-on orientation, a Hubble classification is difficult. The large bulge and halo disfavors a Sc classification; the presence of a dust lane, i.e. the presents of a disk prohibits a S0 classification. Wainscoat et al. (1990) refer to it as S0 or Sa, whereas Lequeux et al. (1995) classify it as a Sab galaxy.

Several distance measurements have been done using different techniques. Jensen et al. (2003), for example, analyzed the surface brightness fluctuation and derived a distance of 12.2 Mpc, while Tonry et al. (2001) found 13.2 Mpc using the same technique. Terry et al. (2002) derived a distance of 17.9 Mpc using the Virgo cluster infall velocity. The mean value of the measured distances is 14.6 ± 2.5 Mpc [2] and I adopt this in this work. Due to the proximity and the large linear size of this galaxy, it is highly resolved and can be studied in great detail.

The disk scale lengths assuming an exponential profile was found by van der Kruit & Searle (1982) using optical and jband images to be $h = 8.4$ kpc and the scale height (sech^2 model) $z_0 = 2.0$ kpc, which is significantly larger than the scale height of the thick disk of our Galaxy in the solar neighborhood ($z_0 = 0.7$ kpc). The rather red optical colors of the disk could either be due to an old stellar population or could indicate reddening

[1] I use the name of the morphological component in the definition of this thesis, even though Eskridge et al. used the term "bulge" in their paper.

[2] NASA/IPAC extragalactic database

by dust. The scale height of the main dust band in the disk is about a factor 2 smaller than the disk's scale height (van der Kruit & Searle 1982; Peletier & Knapen 1992). this dust band is thought to trace the gas layer associated with the young stellar population, which has a much smaller scale height than the old population. About 10 kpc away from the galaxy center, Lequeux et al. (1995) detected a skewed warp in the disk.

The large spheroidal component referred to e.g. by van der Kruit & Searle (1982) is split into two components, i.e. an inner bulge and a halo (or outer bulge), by some authors (e.g. Lequeux et al. 1995). In this thesis, I will refer to the three morphological components "disk", "bulge" and "halo". While van der Kruit & Searle (1982) found the spheroidal, i.e. combination of bulge and halo, to follow the de Vaucouleurs $R^{1/4}$-law (see Sect. 3.1.1), Peletier & Knapen (1992) and Wainscoat et al. (1990) found departures from this law at large radii. Moreover, Lequeux et al. (1995) found a very red color in the halo of the galaxy. They concluded the halo to be dominated by very low mass, very red stars of about 0.3 solar masses.

The Hα image presented by Hameed & Devereux (2005) shows a disk, which is obscured by the main dust lane. There is no obvious halo Hα emission. A detailed analysis must be done in order to state whether the brighter central emission is purely due to disk emission or whether there is a contribution from the bulge.

Wunderlich & Klein (1991) quote IRAS 60 and 100μm flux densities of 1.81 $\pm$ 0.23 Jy and 4.90 $\pm$ 0.46 Jy, respectively, for the galaxy, while there is no detection by the Effelsberg 100-m telescope at 6.3cm, which gives an upper limit of 5.9 mJy (Hummel et al. 1991). Measurements by Spitzer at these wavelengths with a resolution high enough to do a halo-bulge-disk decomposition in the FIR are not available.

The thesis is organized as follows: Chapter 2 gives a detailed description of the preparation of the pipeline data before the actual analysis. The modeling of the galaxy and its components will be explained in Chapter 3. The NIR/MIR SEDs are presented and discussed in Chapter 4. A summary and an outlook will be given in Chapter 5. A glossary with all the abbreviations is given in Chapter 6. The theoretical background on maximum likelihood parameter estimation, including the parameter error estimation, and general statement on model assessment are given in the Appendix A.

Chapter 2

Data Preparation

In order to analyze the infrared properties of the galaxy NGC 7814, it is necessary to take a close look at the pipeline products of the different observation instruments. Several preparatory steps need to be made in order to remove non-galaxian emission from the pipeline images and to prepare them for the further analyses described in chapter 3 and 4. It is especially important to achieve a good background subtraction to avoid a bias in the characterization of faint structures in the outer region of the disk and the halo in chapter 3.

In Sect. 2.1, I will give a brief description of the original pipeline products. Each preparation step of the data will then be described one by one: Star masking is described in Sect. 2.2, image alignment in Sect. 2.3, background subtraction including a noise estimate in Sect. 2.4 and artifact removal in Sect. 2.5. The standardization of the units of the pipeline products will be explained in Sect. 2.6. A summary of all these preparation steps and the resulting images will be given in Sect. 2.7.

2.1 The Original Data

The edge-on galaxy NGC 7814 was imaged in the NIR and MIR by the 2MASS survey and the Spitzer telescope, respectively. The main properties of the pipeline products of these facilities described in this section and are summarized in Tab. 2.1.

2.1.1 Pipeline Maps from 2MASS

The 2MASS survey (Skrutskie et al. 2006) was made using 1.3m telescopes on Mt. Hopkins in Chile. The cameras used have 256×256 pixel arrays made of HgCdTe detectors and have three broad-band channels in the JHK bands with central wavelengths of 1.25μm, 1.65μm and 2.17μm, respectively. The data images are sampled[1] at 1×1 arcsec^2 and have a FWHM of the point-spread function[2] of 3.2 arcsec, representing a convolution of the atmospheric seeing and camera optics. The calibration error[1] is stated to be 2%.

The 2MASS archive offers a mosaic tool[3] which extracts a 800×800 pixel mosaic map with the desired coordinates in the center. I downloaded the data files for all three wavelengths from the archive using this tool.

[1]Users Guide: http://www.ipac.caltech.edu/2mass/releases/allsky/doc/sec2_2.html#pscphotprop
[2]http://spider.ipac.caltech.edu/staff/roc/2mass/seeing/seesum.html
[3]http://hachi.ipac.caltech.edu:8080/montage/

2.1.2 Pipeline Maps from Spitzer

The Spitzer satellite was launched on 25. August 2003. It is in an earth-trailing orbit, which lags about 6 days per year (i.e. it looses 0.1 AU/year to the Earth). The telescope has three instruments, the IRAC (Infrared Array Camera), the IRS (Infrared Spectrograph) and the MIPS (Multiband Imaging Photometer for Spitzer), which observe at different wavelengths or take spectra, respectively. I use both the IRAC and the MIPS broad-band imaging data.

IRAC Images of NGC 7814

Images taken in the four IRAC bands (wavelengths 3.6μm, 4.5μm, 5.8μm and 8.0μm) were downloaded from the Spitzer web page[4] using the 'Leopard'-tool , which is also available there. NGC 7814 was observed[5] on 22. December 2005 at 23:37h.

The images are mosaic maps (1295×547 pixel), containing four main raster elements, each consisting of several single images (see Fig. 2.1). The pixel size of the IRAC maps is 1.2×1.2 arcsec^2 (Wainscoat et al. 1989)[6].

These four wavelengths have different qualities. The 3.6μm band has the best signal to noise ratio (see Tab. 2.3), whereas the 5.8μm image has strong mosaicing imperfections and the 8.0μm image has a line artifact (see Section 2.5). Hora et al. (2008) state the calibration errors to be about 5% and the point-spread function (PSF) to have a FWHM of 1.6, 1.6, 1.8 and 1.9 arcsec for the four wavelengths.

MIPS 24μm Image of NGC 7814

The preprocessed 24μm image was downloaded from the Spitzer web page[7]. It was taken[8] on 28. Mai 2007 at 00:40h. The data map has 191×191 pixels and a map sampling of 2.45×2.45 arcsec^2. It has a calibration error of 2% (Engelbracht et al. 2007; SOM 2007) and a FWHM of the point-spread function of 6.0 arcsec. Unfortunately, images of NGC 7814 in the longer MIPS wavelengths which have exposure times long enough to measure the extended galaxy have not been taken.

2.2 Star Masking

The images from the pipelines contain foreground stars, background galaxies and spikes due to unremoved artifacts. These objects contaminate the galaxy's emission and need to be identified and masked, so they are not used in the background estimation in Sect. 2.4 or the morphological fitting in Chapter 3. In practice, it is impossible to identify all faint stars, especially those which are only slightly brighter than the overall noise level (Sect. 2.4).

I use a preimplemented IDL routine by R.J. Tuffs, which finds "stars" using a median filtered image and masks all pixels around a "star" within a user set radius logarithmically increasing with the brightness of the "star". The routine identifies pixels containing a "star" if their emission is above a user specified threshold brightness on the median filtered

[4]http://ssc.spitzer.caltech.edu/irac/
[5]Data Set Identification for ADS/journals: ads/sa.spitzer#0014481920
[6]IRAC Handbook
[7]http://ssc.spitzer.caltech.edu/mips/
[8]Data Set Identification for ADS/journals: ads/sa.spitzer#0018291456

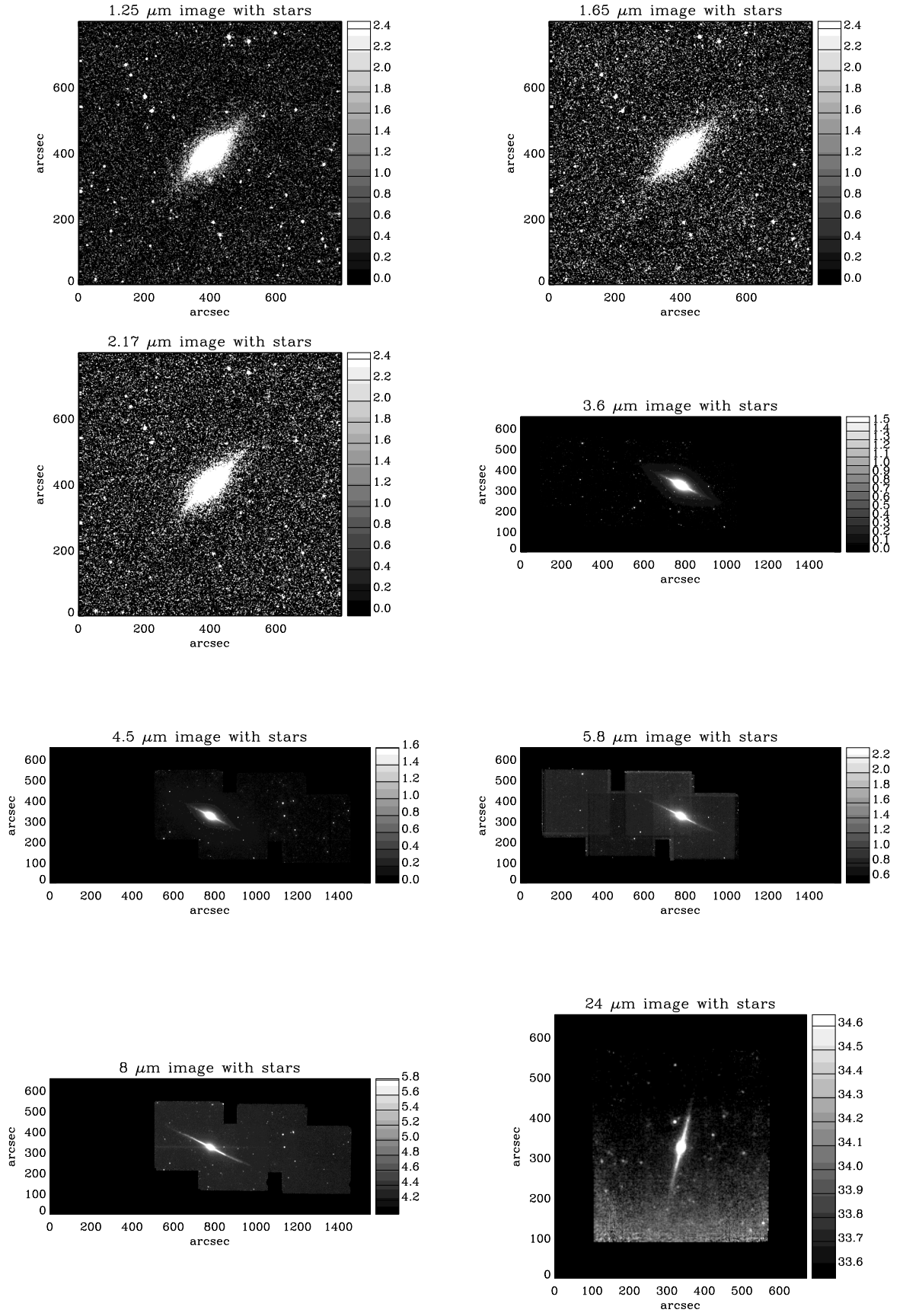

Figure 2.1: Original Pipeline Data

These images are the data as downloaded from the facilities archives or mosaicing tools. The grey scale units are in instrument units for the 2MASS data and in MJy/sr for the Spitzer data.

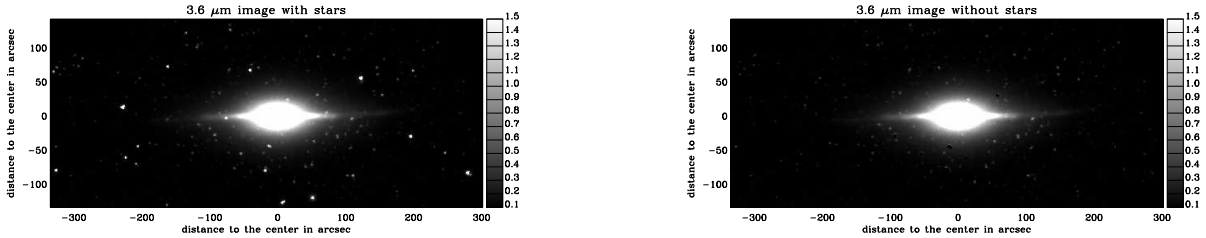

Figure 2.2: 3.6μm Image: Star Masking Before and After
These images show the 3.6 μm maps before and after star masking. All bright stars visible in the left image are masked on the right one. Note the interpolated star in the disk. The images have been rotated such that the disk plane is aligned with the X-Axis.

image. The masking is done on the original pipeline images. However, for this, the routine does not distinguish between emission from compact sources within the galaxy, like HII regions, above the threshold brightness and emission from background sources. Therefore, no automatic star masking is accepted in the region of the galaxy and suggested "stars" in these regions are investigated by eye. In case the routine misidentified parts of the galaxy itself, no masking is done. In case there really is a star in the inner regions, a simple masking of these pixels would cause an underestimate of the galaxy emission, particularly at galactocentric radius. In these cases, for each pixel row parallel to the plane of the galaxy, the brightness underneath the star is interpolated from the surrounding area with the 1D spline IDL function such that the smooth underlying galaxy emission is restored.

No point like source at the nucleus of the galaxy was detected in the different wavelengths. This implies that the active galactic nucleus hosted by this galaxy as stated by (Eskridge et al. 2002) is not prominent in the IR wavelengths.

Table 2.1 lists the number of stars detected. The generally decreasing trend of the star number with increasing wavelength is broken for the 8μm image. This is most likely due to point source like background galaxies, having strong disk emission at 8μm.

Fig. 2.2 shows the example of the 3.6 μm image (after alignment, see Sect. 2.3) before and after the star masking. All bright "stars" have been reliably removed and the disk has been interpolated to remove one foreground "star" on the left side of the galaxy center. Some faint stars, too faint to be detected by the star detection routine, are still left in the image.

2.3 Image Alignment

The galaxy has different positions and orientations in the images of the different instruments. For the later analysis, i.e. background subtraction (Sect. 2.4) and especially the 1D radial fit (Sect. 3.4), it is convenient to align the disk along the X-axis. Even though rotation in pixel space causes repixellation, this is not of crucial importance, since first, the galaxy is highly resolved and second, an even greater effect would be caused creating the 1D radial profile (see Sect. 3.4.1) without alignment.

To find the right rotation angle, I consider a rotationally invariant circular area around the galaxy center, which leaves out a smaller inner circle for the bulge. For rotation angles

Band [μm]	1.25	1.65	2.17	3.6	4.5	5.8	8.	24.
Instrument	2MASS	2MASS	2MASS	IRAC	IRAC	IRAC	IRAC	MIPS
Band Range [μm]	1.11-1.40	1.52-1.78	2.00-2.31	3.20-3.90	4.00-5.05	4.95-6.40	6.40-9.10	21.5-26.
Map sampling	1.0"	1.0"	1.0"	1.2"	1.2"	1.2"	1.2"	2.45"
orig. Map Size	800x800	800x800	800x800	1295x547	1295x547	1295x547	1295x547	191x191
# stars & spikes	100	96	137	80	77	64	95	38
Transf.Fact.[$\times 10^{-5}$]	0.686	0.741	0.612	3.385	3.385	3.385	3.385	14.108

Table 2.1: Map Properties

between $-90°$ and $90°$ in $1°$ steps, the pixel values inside this area are summed over x, creating a profile in y direction. All profiles have a peak at the pixel row which contains the galaxy's center. The profile with the highest peak is the one with the disk best aligned with the x direction, since the integration over the whole disk in one pixel row is only done for the case of alignment. A second run around the found angle is done in $0.1°$ steps to increase the precision. The warp of the disk (see Sect. 2.4) was not taken into account. Since all images of the same instrument were taken simultaneously with the same rotation angle (see Fig. 2.1), the found rotation angles are averaged over all wavelengths of the same instrument. This gives the final rotation angles, which are less sensitive to remaining stars or noise effects.

The resulting rotation angles are $44.2°$, $-27.4°$ and $76.3°$ (positive angle means clockwise) for 2MASS, IRAC and MIPS images, respectively. Fig. 2.7 shows the images of all eight wavelengths after all preparation steps. It is obvious that the image alignment routine finds the correct rotation angles for each instrument.

2.4 Background Subtraction

For any analysis of an object's emission, it is crucial to eliminate fore- or background contamination, e.g. residual atmospheric emission in the NIR or thermal emission of foreground zodiacal dust. Only after a reliable background subtraction, the analysis of structures out to faint levels is possible.

The removal of the contamination due to foreground stars has been described in Sect. 2.2. I will show that the background is dominated by zodiacal light (Sect. 2.4.5) in the IRAC and the MIPS 24μm range. This background is smooth, but varies significantly over the area of the map. Therefore, in this section, I will explain a flexible method to subtract background light with a slowly varying position dependency from an image. To do this, I will first define the area in the images used for the background estimation in Sect. 2.4.1 and then explain the actual background subtraction method in Sect. 2.4.2. The bias in this method and it's correction are explained in Sect. 2.4.3. Finally, I will estimate the background noise in Sect. 2.4.4 and compare the found background level with the foreground expectation from pure zodiacal light in Sect. 2.4.5 to check the overall calibration of the instrumental response to extended emission.

2.4.1 Background Area

Before I can determine the actual background, I have to define the region containing the galaxy emission, i.e. which cannot be used for background estimation. To do this, I define a region above and below the galactic plane.

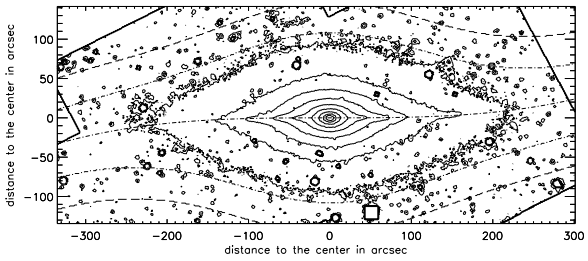

Figure 2.3: Background Area
The area around the galaxy used for the background calculation is shown for the 3.6μm image. The warp of the disk is accounted for by the galactic plane (central dashed-dotted line) being a cubic function rather than a straight line. The central region enclosed by the outer dashed-dotted lines is dominated by the galaxy, therefore only the area between the outer two lines on both sides of the galaxy is considered for the background.

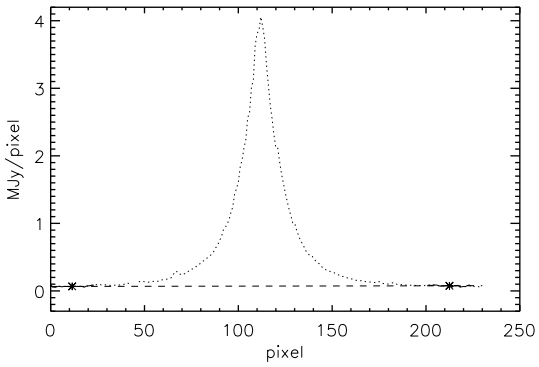

Figure 2.4: Background Definition
For any data pixel column perpendicular to the disk (dotted line), a small region on both sides (solid) is used to calculate the median of the background in these regions (asterisk). Then, a straight line (dashed) is placed through these two points in the middle of the two regions, which represents the background for the whole pixel column.

This region must take into account a slight warp in the galaxy's disk, found by van der Kruit & Searle (1982) at optical wavelengths. I find clear evidence for a warp in the disk in the near and mid infrared, too. The disk is almost flat in the central regions and the warp becomes more significant in the outer parts. For all future analyses, including the background routine described below, I used a cubic function instead of a straight line to define the locus of the galactic plane (see Fig. 2.3, central line).

To define the outer limit of the geometrical shape of the galaxy region, I use a Gaussian function of the radial distance to the galactic center to define the perpendicular distance to the galactic plane, which includes the warp. For large radii, where the perpendicular distance derived with this Gaussian is very small, I use a constant minimum distance to the galactic plane instead. Both functions and their parameters were adjusted by eye.

The outer boundary of the galaxy region includes roughly all galaxy emission significantly above the noise level (estimated in Sect. 2.4.4). However, some faint emission is still outside these boundaries and will cause the background to be biased, which will be discussed in Sect. 2.4.3. Since the IRAC data covers only a small area above and below the central region, this definition of the galaxy region is good compromise in order to have enough pixels outside this area to estimate the background from.

2.4.2 Background Subtraction Method

In order to estimate the background of an image, I use a method which derives the background for each pixel column separately. In this way, I can correct for changes in the level of the background at different galactocentric radii. For example, the background can have a tilt in x- or y-direction and even a twist in x-direction. This way, it can represent a structure in a fore- or background much better than just a constant background for all pixels, which would not be able to account for the obvious slope of the background,

Wavelength [μm]	1.25	1.65	2.17	3.6	4.5	5.8	8.0	24.
First Backgr. Est.	-0.029	-0.031	-0.0400	0.106	0.298	2.526	9.013	33.647
False Halo Backgr.	0.039	0.020	0.042	0.007	0.005	0.004	0.003	0.001
Corrected Backgr.	-0.068	-0.050	-0.082	0.099	0.293	2.522	9.010	33.646
Syst. Calibr. Error [%]	2	2	2	5	5	5	5	2
$\delta_{\text{Background}}$	0.0022	0.0036	0.0036	0.0001	0.0001	0.0002	0.0001	0.0007

Table 2.2: Background with Errors

The tables shows the different steps of the background determination. All values, if not stated differently, are in MJy/sr. The $\delta_{\text{Background}}$ is the random error in the background estimate due to pixel noise.

especially prominent in the 24 μm data (see Fig. 2.1). This procedure is facilitated by the alignment of the disk with the X-axis (see Sect. 2.3).

I will use the pixel column at a distance of 40 arcsec from the center of the galaxy of the 3.6μm image (Fig. 2.4) as an example to illustrate the background method. On both sides above and below the galaxy region (defined in Sect. 2.4.1, solid line in Fig. 2.4), a fixed number of pixels is used to calculate the background, i.e. the area between the dashed and the dashed-dotted line in Fig. 2.3. Bad pixels, which might be masked stars or pixels without data coverage, are not taken into account. The median value on both sides of the galaxy area is calculated separately and assigned to the center of the background area on each side (asterisks in Fig. 2.4). A median gives less weight to the unmasked faint star emission than the mean would do. Finally, the two median values are interpolated with a straight line (dashed line in Fig. 2.4), which represents the background of that pixel column including the area of the galaxy. Doing this for all pixel columns, the background surface is derived. It is possible that some pixel columns at the edges of the image have only bad pixels in the background area, i.e. do not have data coverage. In that case, the whole pixel column was declared as bad pixel.

The backgrounds of the IRAC images are rather flat, whereas the background of the MIPS data has the strong tilt expected from Fig. 2.1, due to the very strong zodiacal emission seen in the 24μm band. Virtually no background is found for the 2MASS data, since they have been background corrected previously in the 2MASS pipeline. Since the pipeline routine used a different area to define the background and since it included the foreground stars, the background values found by my routine must be negative. The mean background level is presented in table 2.2 for all eight wavelengths.

The error of the mean background level for each wavelength is estimated by Gaussian error propagation of the noise of the pixels (Sect. 2.4.4) used to derive the background. Since the background is averaged over a large number of pixels (from about 21.000 for MIPS to about 128.000 for 2MASS), the pixel noise affects the background estimation only slightly. The error of the background estimation was not included as an additional error of the data in the further analyzes, since the noise used for this error estimate is still on the data and will dominate the error budget. Systematic errors such as instrument calibration (see Sect. 2.1.1 and Sect. 2.1.2, Tab. 2.2) are not considered in the background error.

Wavelength [μm]	1.25	1.65	2.17	3.6	4.5	5.8	8.0	24.
Noise [MJy/sr]	0.677	1.144	1.154	0.034	0.027	0.066	0.044	0.082
Signal to Noise Ratio	292	200	195	1439	1105	396	579	56

Table 2.3: Noise Level and Signal to Noise Ratio after Background Subtraction

2.4.3 Correction for the Background Bias

It is necessary to get as close to the galaxy as possible in order to have a large area to estimate the background from and thereby to minimize random noise error in the estimate of the background at the position of the galaxy. However, using data too close to the galaxy would cause the background to be systematically overestimated, i.e. biased high, due to the galaxy's emission. This has to be corrected for in order to avoid a systematic bias in the fitting of the geometrical shapes in chapter 3.

Since the original data in the IRAC bands cover only a small area around the galaxy, this bias is unavoidable due to the limited data above and below the galaxy center, leaving a small galaxy emission in the area of background calculation. This results in a bias of the background itself of about 7%, 2%, 1% and 1% for the IRAC bands 3.6μm, 4.5μm 5.8μm and 8μm, as estimated from simulations.

Due to the shape of the background area, which is particularly constricted at low galactic radii, this bias affects mainly the bulge region. The disk will be analyzed in the outer regions (Sect. 3.4), where the background routine is less biased. The halo is a very large structure out to large radii. In the fitting area (see Sect. **??**) of the halo, only a small the fraction of pixels is biased and therefore, only a minor low bias on the halo estimate is to be expected. The bulge, however, is completely embedded in the region with background bias.

Since the source of this bias is known, it can be corrected for through simulations. Specifically, after the halo model has been fitted to the data (described in Sect. 3.3), a second background run is done on a simulated image. This time, the "data" is the derived noiseless model for the outer region of the galaxy, i.e. the halo model (see Sect. 3.3.1). The background found in the second run is a good estimate of the galaxy's contamination in the first background subtraction, since the halo is the only part of the galaxy which extends into the background region. This false background is then added back to the halo removed data (for the mean background level see Tab. 2.2).

This procedure cannot be done iteratively, because it is not guaranteed that the iteration would converge. In the first step, the halo emission is used to make the background smaller than the first estimate. In each further step, the halo emission would rise due to a smaller background subtracted. This would cause each time a higher false background estimation, which again leads to an even smaller total background. Therefore, the halo removed data are false background corrected and not the data of the whole galaxy. The background bias has a negligible influence on the halo fit for the reasons mentioned above.

The error of the total background is an estimate from the propagated pixel noise (see Sect. 2.4.4) of the pixels which were averaged for the background determination. It does not include possible systematic errors or biases.

2.4.4 Noise Estimation

The standard deviation ($\sigma = \sqrt{\frac{1}{N-1}\sum_{i=1}^{N}(x_i - \overline{x})^2}$) was estimated directly from the data for all the wavelengths using all defined pixels in the region of background calculation.

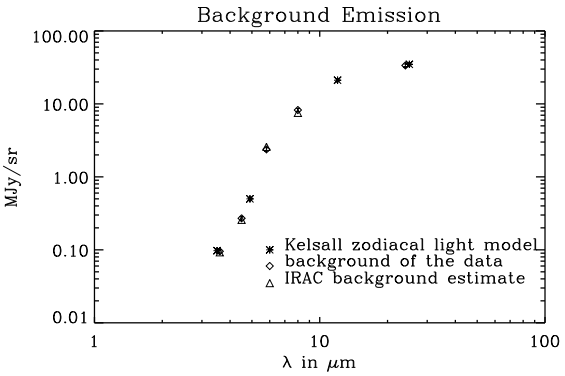

Figure 2.5: Zodiacal Light Model
Comparison of the brightness of the five spaceborne image backgrounds (color corrected) in MJy/sr with the zodiacal light model by Kelsall et al. (1998) and with the Spitzer estimate, one can see a good agreement between the data and the models. The IRAC points include the zodiacal light removed by the telescope team.

This assumes a pure Gaussian noise.Table 2.3 shows the standard deviations for all eight wavelengths.

The signal used to derive the signal to noise ratio (S/N) is the total flux of the galaxy, i.e. total galaxy emission integrated over the whole image. The random noise in this case is the Gaussian propagated noise from all the pixels in this integration. The S/N values are presented in Tab. 2.3 as well. The IRAC data has a good S/N of 1439 and 1105 for the 3.6μm and the 4.5μm images. The S/N at 5.8μm and 8μm is somewhat lower; at 5.8μm a contributory factor to this is the mosaicing artifact (see Sect. 2.5). As is to be expected, the ground based 2MASS data have a comparably low S/N of 200-300 due to atmospheric noise. The 24μm band has an even lower S/N of 56 due to a small galaxy signal, a smaller number of pixels in the integration area and a greater standard deviation per map pixel.

2.4.5 Zodiacal Light

In the mid infrared, the dominant component of the foreground emission is the zodiacal light, i.e. scattered light and thermal emission from the interplanetary dust in our solar system. Minor contributions come from foreground dust in our galaxy and the cosmological population of galaxies. Therefore, a comparison between the estimated background level of the data (Sects. 2.4.2 & 2.4.3) and a zodiacal light prediction be used to check the overall calibration.

In order to compare the background of the data with the zodiacal light, I used the model of Kelsall et al. (1998)[9], which was derived from COBE data. They used a dust density distribution composed of three components: a smooth cloud, three asteroidal dust bands and a circumsolar ring near 1AU. The model brightness is evaluated as an integral in the line of sight of the product of a source function and this dust-density distribution.

The model derives the foreground emission coming from the zodiacal light for a given date and pointing direction for the COBE wavelengths (i.e. 1.25μm, 2.2μm, 3.5μm, 4.9μm, 12μm, 25μm, 60μm, 100μm, 140μm and 240μm). Since the Spitzer telescope is not in a geocentric, but Earth-trailing orbit, the zodiacal light is not identical for the telescope and the Earth. The main difference is the date, i.e. the position in the orbit. The 'Earth date' must be translated to 'Spitzer date', since Spitzer has a drift rate of 0.1 AU per year from the Earth, which translates to a date shift of about 6 days/year. The different position in the Earth's resonant dust ring causes a different amount of dust in the line of

[9]An IDL software implementation of this model was downloaded from http://lambda.gsfc.nasa.gov/product/cobe/dirbe_zodi_sw.cfm .

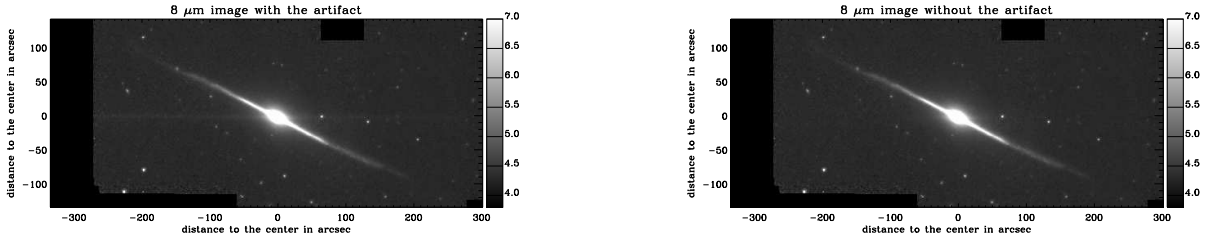

Figure 2.6: 8μm Image: Line Artifact Before & After
The image on the left side shows the 8μm data with the line artifact (horizontal line through the nucleus) and the right image shows the data after the artifact was removed.

sight of Spitzer, which causes a difference of the zodiacal light prediction of up to 5% [10]. This is not considered in the Kelsall model and therefore, it is a systematic error in the model prediction.

The total brightness of the background of the Spitzer data is listed in Tab. 2.2. The 2MASS background cannot be compared with the zodiacal light predictions, since they are ground-based data, with a background dominated by atmospheric effects. The IRAC images have already been partially cleared from zodiacal light, i.e. a constant value of about half of the mean zodiacal light has been subtracted in the pipeline. The subtracted values are given in the image headers and are added to the mean background found by the background routine (Sects. 2.4.2 & 2.4.3) in order to compare the background of the data with the zodiacal light model. The color corrected background values Wainscoat et al. (1989)[11] are shown in Fig. 2.5 (diamond), together with the Kelsall model predictions (asterisk) and the zodiacal light estimate given by the Spitzer/Spot zodiacal light estimator[6] (triangle). The background values of the data agree very well with the Spitzer estimate. The 3.6μm, 4.5μm and 24μm band values are in good agreement with the Kelsall model, as well. A direct comparison of the 5.8μm and 8μm band background with the Kelsall model is not possible since no model values close to these wavelengths are given by the model implementation.

The overall acceptable agreement indicates that the background of the images are the zodiacal light foreground and that the instrumental calibration is accurate within the stated random ans systematic error budget.

2.5 Artifact Removal and Mosaicing Problem

Artifact Removal

Fig. 2.6 shows the 8μm image which exhibits a line artifact through the nucleus. Since this artifact is parallel to the pixel rows and limited to a few rows only, it is most likely an artifact caused by CCD overflow in one of the mosaic elements. The higher emission in these pixels due to the artifact is of the order of the pixel noise. However, it is noticeable, since it is a systematic offset. It was not possible to mask the artifact, since it goes through the center of the galaxy, which would have been masked as well. Therefore,the

[10] http://ssc.spitzer.caltech.edu/documents/background/node3.html
[11] IRAC Handbook p.48

Band	Lambda (μm)	Bandwidth (μm)	F_0 mag (Jy)	$MAGZP$
J	1.235 ± 0.006	0.162± 0.001	1594± 27.8	20.9162
H	1.662± 0.009	0.251± 0.002	1024± 20.0	20.3519
K	2.159± 0.011	0.262± 0.002	666.7± 12.6	20.0927

Table 2.4: 2MASS Configuration Parameters

artifact was removed using the background routine explained in detail in Sect. 2.4.2. Only a small region perpendicular to the row of the artifact was considered. For each pixel row with line artifact, a line representing the offset was placed through the median values of the outer regions, not taking the galaxy itself into account. That way, the effect of the line artifact could be extrapolated to the pixels with galaxy emission. This linear offset was then subtracted from each pixel row.

Since the background subtraction will be done after the artifact removal, the interpolated background level of the neighboring pixel rows has to be added to the artifact cleared pixel rows. The resulting image (Fig. 2.6) is free of the line artifact and still has the same background structure in all pixels.

Having both images at 8μm, with and without artifact, it was possible to evaluate the impact of this artifact by applying the 1D fit (Sect. 3.4) and compare the fit parameters. Both sets of parameters were the same within the one-sigma-errors. Therefore, the impact of this artifact can be considered to be small.

Mosaicing Imperfections

The original 5.8μm image has mosaicing imperfections (see Fig. 2.1). Depending on how many of the single images of the individual pointings overlap, the background offset is different, due to different sensitivity of the individual pointings. This results in a 2D artifact, which would affect the two sides of the galaxy differently. Since the 1D radial profile (Sect. 3.4.1) does not show significantly different profiles on the left and on the right side of the center, this artifact causes only a negligible bias.

2.6 Unit Conversion

In the Chapters 3 and 4, I will compare the integrated galaxy emission of all the eight wavelengths. Integrating over the same area of sky in all eight wavelengths, the pixel sizes need to be considered. The units of the emission saved in each pixel is in MJy/sr for the IRAC and the MIPS data. Converting this unit to Jy/pixel makes the later integration easier since it reduces to a simple summation over all the pixels within the same area of sky. Using the fraction of the solid angle 1sr covered by one pixel, the unit conversion becomes a simple multiplicative factor given in Tab. 2.1, which is identical for all four IRAC bands.

In case of the 2MASS data, the pixel units are not in physical energy units but in data-number units. They need to be changed first to magnitudes, and then to Jy/pixel. Using the equation given on the 2MASS service web pages [12]

$$m = MAGZP - 2.5 \log_{10}(S) \tag{2.1}$$

[12] especially http://www.ipac.caltech.edu/2mass/releases/allsky/faq.html#conversion

where S is the pixel value and $MAGZP$ (see Tab. 2.4) the zero point magnitude given in the header of the images, the magnitude is derived. With the mathematical definition of magnitudes and the zero point flux F_0 (see Tab. 2.4), it is easy to get the flux per pixel F (in Jy / pixel).

$$m = -2.5 \cdot \log_{10} \frac{F}{F_0} \tag{2.2}$$

$$\log_{10}(F) = \log_{10}(F_0) + \log_{10}(s) - MAGZP/2.5 \tag{2.3}$$

$$F = F_0 * S/10^{(MAGZP/2.5)} \tag{2.4}$$

2.7 Summary

The data preparation started with the identification and masking of stars and the removal of artifacts. Then, the galaxy disk in all images was aligned along the x-axis. The background was removed in two steps and finally, the units were converted to Jy/pixel.

Fig. 2.7 shows the images after all the steps described above. A comparison with Fig. 2.1 demonstrates the successful data preparation. The line artifacts in the 2MASS data surrounding the extended region of galaxy emission results from the long interpolation of the background. Noise fluctuations in the background estimate start to become noticeable in the interpolations for large distances away from the background area. However, only the area of sky that has coverage in all eight wavelengths (i.e. up to 134" above and below the galaxy center) will be analyzed in the next chapters. Since these artifacts are outside of this area they are not able to influence or bias the later analyses.

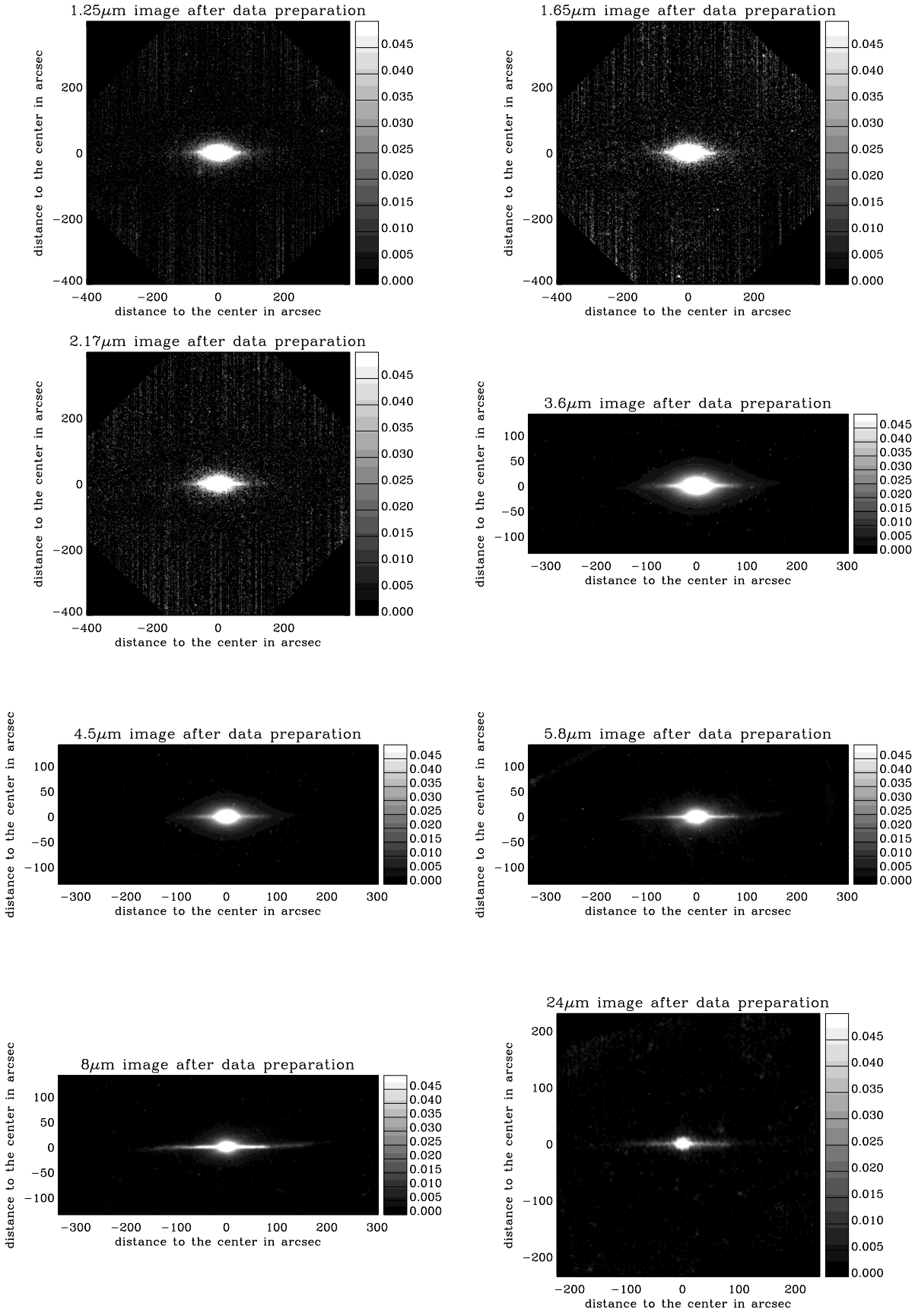

Figure 2.7: Data after Data Preparation

This figure shows all images after the data preparation steps on the same grey scale for all eight wavelengths in units mJy/arcsec^2. The lines in the 2MASS images are caused by the background routine, which has to interpolate each pixel row background over a long distance. Since these image areas will not be used in the later analysis, this does not cause a bias.

Chapter 3

Modeling the Structure of NGC 7814

In order to analyze the different morphological components of the galaxy NCG 7814, it is necessary to develop a model defining these components and to fit this model to the data. The choice of the model will be motivated in Sect. 3.1, while the overall strategy of the galaxy fit is explained in Sect. 3.2. In Sects. 3.3 and 3.4, the 2D fit of the halo and the 1D fit of both the bulge and the disk are described and the results are discussed. Systematic tests of the 1D fit routine for the bulge and the disk are also presented in Sect. 3.4. Finally, in Sect. 3.5, a 2D reconstruction of the data is presented, using the 1D fit results of Sect. 3.4 .

Appendix A derives the theoretical background of maximum likelihood parameter estimation including the derivation of their errors using the Fisher matrix. The difficulty of model assessment is discussed there as well. In this chapter, I will discuss the results obtained by using these methods, not the methods themselves.

3.1 Choice of Galaxy Model

Traditionally, to analyze a galaxy's bulge, a two component bulge-disk-decomposition is done, mostly for optical data (e.g. Kent (1985); Fisher & Drory (2008); McDonald et al. (2009) and MacArthur et al. (2003)). I, too, did a pure bulge-disk-decomposition as described in Sect. 3.4 in the first attempt to fit the edge-on galaxy NGC 7814. However, the very round and extended shape of the faint emission of this galaxy was not possible to be reproduced in the 2D fit (see Sect. 3.5) with only these two components.

The inner region's fit was acceptable for two components, which explains why previous analyses, e.g. done by van der Kruit & Searle (1982) and Wainscoat et al. (1989) which had a lower resolution and a worse signal to noise ratio, restricted themselves to a model with a disk and a de Vaucouleurs' spheroidal. They were not able to analyze their data further out than disk radius = 150". Therefore, they barely reached the low emission regions, where the two component model fails to describe the data. Hence, I choose a more complicated model with a halo as additional third component.

I used a model consisting of linear combinations of a halo, a bulge and a disk. All these components themselves are Sersic functions (see Section 3.1.1), which have nonlinear parameters, namely Sersic index n, scale length R_e and ellipticity *ellip* for each of the three components.

3.1.1 Sersic Function

As model for the different components of the galaxy, I used the Sersic profile (Sérsic 1963, 1968) as radial emission profile, which is

$$I(R) = I_e \exp\left\{-b_n\left[\left(\frac{R}{R_e}\right)^{\frac{1}{n}} - 1\right]\right\} \tag{3.1}$$

where I_e is the intensity at the effective radius R_e which encloses half of the total light from the model (see Graham & Driver (2005) for details). The parameter b_n, which is called Sersic index, is defined by

$$2\gamma(2n, b_n) = \Gamma(2n) \tag{3.2}$$

which can be solved numerically for b_n. The parameter n describes the steepness of the light profile in the center (see Fig. 1 Graham & Driver). Exponential disks have $n = 1$, the de Vaucouleurs' profile has $n = 4$ and a Gaussian profile would have $n = 0.5$. Generally, classical bulges have $n \gtrsim 2$ and pseudo bulges have $n \lesssim 2$ (Fisher & Drory 2008).

The Sersic profile is an experimentally found radial brightness distribution for face-on galaxies, representing the integrated volume emissivity along the line of sight. Since NGC 7814 is an edge-on galaxy, the geometry is slightly different. Bulge and halo are ellipsoids, therefore the Sersic model can be used for all angles of sight, replacing the radius R with an elliptical distance

$$R^2 \longrightarrow x^2 + z^2/ellip^2 \tag{3.3}$$

where $ellip = \frac{b}{a}$ is the ration of the semi minor and semi major axis of the galaxy.

The disk, however, may have a different shape perpendicular to the disk plane than parallel to it. Therefore, the Sersic profile, which is already integrated in z direction, needs to be integrated along the actual line of sight, i.e. y direction since the disk is seen edge-on, reducing the model to one dimension. This means that no ellipticity is needed, since different values for the ellipticity change only the amplitude of the integrated model, not the actual shape (see Sect. 3.4.2).

Small systematic errors will arise, if the true shape of the bulge or the halo is not a true ellipse, but a flattened one, which is rounder at the ends and flatter in the middle. The model has not the complexity to adjust to that shape.

3.2 Strategy of the Galaxy Fit

The three component galaxy model has several nonlinear parameters. Estimating all these parameters simultaneously in a single maximum likelihood fit (see Sect. A.1) would be very time consuming. Moreover, the parameters have mutual degeneracies and the fit is likely to find local minima in the χ^2 hypersurface instead of the global one.

It is always helpful to reduce the number of fitting parameters in one fitting step. In case of this galaxy, it is possible to fit the very extended halo separately from the bulge and the disk in the regions where the other two components do not contribute. The halofit, described and discussed in Sect. 3.3.1, has the three nonlinear fit parameters scale length $R_{e,h}$, Sersic index n_h and ellipticity $ellip$, and the linear amplitude A_h.

MacArthur et al. (2003) discuss the merit of a two-dimensional versus a one-dimensional model for their face-on two component fitting algorithm. They favored the better signal-to-noise ratio of the one-dimensional model, even though the two-dimensional model would have enabled them to consider non axial symmetric features such as rings, bars oder spiral arms. Nevertheless, since NGC 7814 is not a face-on but an edge-on galaxy, none of these features would be visible in a two-dimensional model. Therefore, and since the Sersic model of an edge-on disk does not contain information about the z profile, the bulge and the disk will be fitted as 1D radial profiles. This fit will have two linear Amplitudes A_b and A_d and three nonlinear parameters, i.e. the two scale lengths $R_{e,b}$ and $R_{e,d}$ and the bulge Sersic index n_b. The disk Sersic index is fixed to $n_d = 1.$, assuming an exponential disk. In the 1D reduction, the bulge does not need an ellipticity parameter (see explanation for the disk in Sect. 3.1.1).

I will also perform a 2D reconstruction of the bulge and the disk (Sect. 3.5). This is only done in order to obtain information on the z distribution of the emission from these components. It has no influence on the derived MIR SEDs. This 2D fit requires another three parameters: the bulge ellipticity and two z shape parameters for the disk.

3.3 Fitting the 2D Halo

In this Section, I will first describe the fitting procedure, including fitting area and the special treatment of the 24μm data in Sect. 3.3.1. I will the discuss the fitting results in Sect. 3.3.2 and finally present two easy ways to judge the quality of the halo fit by eye are presented in Sect. 3.3.3.

3.3.1 Fitting Procedure for the Halo

The halo is the most extended morphological component in my model. Therefore, it is possible to define an area in the data maps, where only the halo will contribute to the emission. This area is the same in all eight wavelengths and is shown in Fig. 3.1, left column. It has an area of almost 200 x 98 arcsec^2 on each side of the disk plane, 22 arcsec above the mid plane (i.e. $\sim$1.6kpc for a galaxy distance of 14.6Mpc), with the edges at the disk plane being cut off. This is necessary since the disk extends further in z direction for larger radii (see Sect. 3.5).

Having a pure halo emission area, the model can be reduced to the pure halo model for this fit:

$$F_{\mathrm{halo}}(A_h, R_{e,h}, n_h, ellip) = A_h \cdot e^{b_n} \cdot \exp\left[-b_n \cdot \left(\sqrt{\frac{z^2 + x^2/ellip^2}{R_{e,h}^2}}\right)^{\frac{1}{n}}\right] \tag{3.4}$$

with the fit parameters amplitude A_h (in Jy / pixel), scale length $R_{e,h}$ (in arcsec), Sersic index n_h and ellipticity *ellip*. x and z are the distances from the galaxy center in arcsec, with z taking the warped disk into account. The ellipticity is defined this way for the halo, in order to have the possibility to check the fit for the other parameter by eye at the central pixel column, where x = 0 and therefore the ellipticity does not influence the model for this pixel column.

The best parameter set for the halo was determined in the considered area with a fit routine written by Markwardt (2009) in IDL, which uses the Levenberg-Marquardt technique to solve the least-squares problem. The χ^2-function is

$$\chi^2 = \sum_{i,j} \left(\frac{(F_{\rm halo}(i,j) - data(i,j))^2}{\sigma_{ij}^2} \cdot W_{i,j} \right) \tag{3.5}$$

where i,j are the pixel coordinates, i.e. χ^2 is summed over all pixel, σ_{ij} is the random error on the pixel ij and $W_{i,j}$ is the weight given to the pixel ij. This weight function contains the pixel mask and assigns "good" pixel the weight 1 and "bad" pixel the weight 0. The random error estimates of the parameters were derived with the Fisher matrix (Sect. A.2).

The halo model of each wavelengths is subtracted from the data and the halo removed data will be used for further analyses in Sect. 3.4.

3.3.2 Results of the Halo Fit

The resulting values of the fit parameters are shown in Tab. 3.1 and in Fig. 3.6. The best fit models are shown in Fig. 3.1, second column from the left.

For the wavelengths 1.25μm - 4.5μm, the found ellipticity values are identical within the errors and the mean ellipticity is 1.80. Other measurements of the ellipticity of the whole galaxy by other authors resulted found values of 1.72 (derived by Jensen et al. (2003) with Hubble data) and 1.75 and 2.22 (derived by van der Kruit & Searle (1982) with optical observations obtained at Palomar Observatory using isophotes and isochroms respectively). In order to avoid a possible biases due to the image imperfections in the 5.8μm and 8μm bands, an upper limit of 1.81 for the halo ellipticity was introduced. Tab. 3.1 and in Fig. 3.6 show, that this limit is reached for these two wavelengths. The scale length is similar within the errors for the five shorter wavelengths. The 5.8μm and 8μm band have a slightly higher scale lengths than the shorter wavelengths.

The Sersic index spreads between 1.43 and 2.27 over a relatively wide range. Since the halo parameters were derived in an area further out than one scale length, there is only a small change in the shape due to a different Sersic parameter for the considered area. The difficulty of determining the Sersic index of the halo is the trade-off for the bulge emission free fitting area. The amplitudes show a tendency of decreasing with decreasing wavelength (except for 24μm).

The Fisher matrix (derived from the curvature of the χ^2 hypersurface; see Section A.2) shows high correlations for some of the fit parameters (see Tab. 3.4 for the example of 3.6μm). For all wavelengths, the amplitude and the Sersic index have a high correlation of about 0.9. This is understandable, since the Sersic index varies the shape of the profile (see Graham & Driver (2005), their Fig. 1). The higher the Sersic index, the steeper and sharper is the central peak and the shallower is the slope far away from the central peak. Since the considered region for the halo starts about one scale length away from the center of the galaxy (i.e. 22" away the mid plane), the shape change with the Sersic index is mostly a change in the amplitude. The ellipticity shows small correlations with the Sersic index of about 0.2-0.3 and with the amplitude of about 0.3-0.4. This has similar reasons. Increasing the ellipticity makes the profile steeper in the x direction of the image. This can be slightly compensated by increasing Sersic index and the amplitude. The scale length has very small correlations and can be considered as independent.

Wavelength [μm]	A_h [Jy / pixel]	$R_{e,h}$ ["]	n_h	*ellip*
1.25	$(5.13 \pm 0.24) \cdot 10^{-5}$	22.90 ± 0.51	1.77 ± 0.08	1.80 ± 0.01
1.65	$(6.39 \pm 0.39) \cdot 10^{-5}$	22.12 ± 0.62	1.43 ± 0.08	1.80 ± 0.02
2.17	$(5.51 \pm 0.47) \cdot 10^{-5}$	21.54 ± 0.86	1.92 ± 0.14	1.80 ± 0.02
3.6	$(4.00 \pm 0.06) \cdot 10^{-5}$	21.91 ± 0.16	2.01 ± 0.03	1.81 ± 0.01
4.5	$(2.70 \pm 0.08) \cdot 10^{-5}$	20.98 ± 0.27	2.27 ± 0.05	1.79 ± 0.01
5.8	$(1.67 \pm 0.06) \cdot 10^{-5}$	26.19 ± 0.44	1.61 ± 0.07	1.81 ± 0.01
8.0	$(1.31 \pm 0.07) \cdot 10^{-5}$	24.21 ± 0.64	1.96 ± 0.11	1.81 ± 0.02
24.	$(2.79 \pm 1.29) \cdot 10^{-5}$	21.78 ± 0.13*	2.20 ± 0.15*	1.80 ± 0.01*

Table 3.1: Halo Parameters with Errors

The fit parameters for the halo with their Fisher matrix random errors. Values marked with a * indicate values fixed to the weighted mean values of the five shorter wavelengths, as used in a constrained fit to A_h (see text).

Special Case 24μm Image

The direct fit to the 24μm data gave results with very large uncertainties, due to the small signal and the noise (S/N) of data in the considered area. Therefore, the scale length, the Sersic index and the ellipticity were fixed to the weighted mean μ of the five shorter wavelengths (1.25μm - 4.5μm), since their S/N in the considered area is better that the S/N of the longer wavelengths. The errors are the standard deviation 1σ of the mean μ, and therefore lower than the parameter error of the other wavelengths. The only parameter left for the fit is the amplitude. The large error in the amplitude expresses the low S/N in the outer regions of the image used for the halo fit.

$$\mu = \sum_i \frac{R_i}{\sigma_i^2} / \sum_i \frac{1}{\sigma_i^2} \qquad \frac{1}{\sigma^2} = \sum_i \frac{1}{\sigma_i^2} \tag{3.6}$$

The annulus emission and curve of growth in Fig. 3.1, discussed in detail in Sect. 3.3.3, suggest a much smaller error of the amplitude fit as listed in Tab. 3.1. The curve of growth shows a very good fit to the data for small radii, but an underestimation of the data for large radii. This underestimation of the data at large radii, which have negligible emission as proved by the annulus emission, causes a systematic overestimation of the variance, i.e. the variance is too large. Therefore, the large error listed in Tab. 3.1 does not represent the quality of the fit in the halo emission itself. However, this value will be used in the error propagation, lacking an error estimate for the amplitude for the inner regions only.

3.3.3 Annulus Emission and Curve of Growth

In order to get a better impression on how well the halo model fits the data, two other ways of presenting the data are considered. First, the mean emission per pixel in the radius r of the data within the halo area described above is compared with the halo model. For elliptical rings with a width of two pixels, the mean emission per pixel is shown in the column second from the right of Fig. 3.1 (solid line). Masked pixels were not used to derive the mean value of the data or the model. The errors are propagated from the individual pixel noise. The data shows an asymptotic behavior to zero at large radii, indicating no flat background emission is left on the data. The same was done for

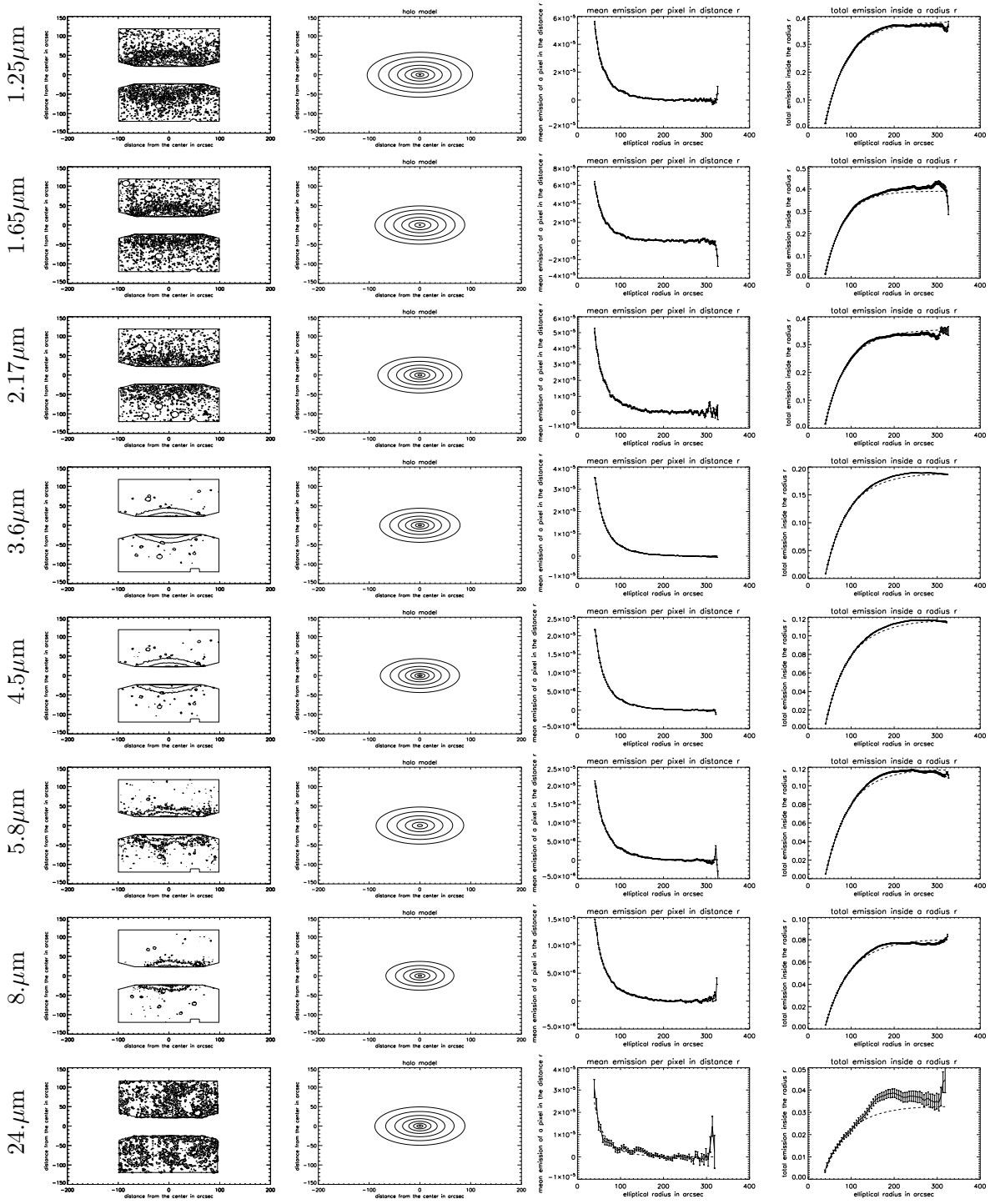

Figure 3.1: Halo Model

Left: contour plot of area to derive the halo model parameters from. The contour level are [0.0025, 0.005, 0.01, 0.02, 0.04, 0.08, 0.16, 0.32]·maximum. Second from the left: The derived halo model with the same contour lines. Second from the right: Comparing the mean emission per pixel in elliptical distance from the galaxy center with model. right: Comparing the curve of growth with the model. For the IRAC and MIPS data, the pixel units are in MJy/sr, for the 2MASS in utility units (see Sect. 2.6 for conversion to Jy / pixel area).

the halo model (dashed line). For all eight wavelengths, the model is matching the data perfectly.

Second, the curve of growth is shown in the right column. It represents the total emission inside an elliptical radius. Masked pixels or the area outside the halo area were accounted for by a factor to the emission in the defined area. The graphs show a good agreement of the model (dashed line) with the data (solid line) in the inner regions.Towards larger radii, where the data has no signal anymore and only noise, variations of the overall background level within the image become visible. This will cause the data to fluctuate around the true value of the emission enclosed inside the radius considered. For all wavelengths but 24μm, these variations are negligible, In case of the 24μm band, these deviations from the model are due to the noise in the data and possible background fluctuations. The fluctuations in the largest radii sampled are due to the bad statistics (i.e. for large radii, only very few or even only one pixel was within the halo area and could therefore been used for this plot). For all eight wavelengths, the model is matching the data very well.

3.3.4 Extraction of the Halo SED

The value for the halo spectral energy distribution (SED, see Fig. 4.1) is the total emission of the halo model in the biggest area which has coverage in all wavelengths (which is 445"×268", with the galaxy center in the center). Even though a little fraction of the emission might be cut off that way, the same bias is applied to all wavelengths. A much bigger bias would be caused by integrating the halo model over the different sizes of the data maps of the different wavelengths. The error of the SED value is derived from the errors of the fit parameters (see Sect. A.2).

3.4 Fitting 1D Radial Profiles for the Bulge and the Disk

In this Section, I will discuss the model and the fit method of the 1D bulge and disk fit. In Sect. 3.4.1, I will explain how the data was reduced to a one dimensional radial profile. The one dimensional model is described in Section 3.4.2. Actual fit routine is described in Sect. 3.4.3 and tests are presented in Sect. 3.4.4. The redundancy of an offset parameter is shown in Sect. 3.4.5. The found fit parameter set is discussed in Sect. 3.4.6.

3.4.1 1D Radial Brightness Profile

The 1D profile of the measured galaxy emission $F_{1D}(i)$ is derived by summing over the emission of the halo-subtracted map inside the galaxy's area (see Sect. 2.4 and Fig. 2.3) in each pixel column, i.e. perpendicular to the disk plane:

$$F_{1D}(i) = \sum_j data(i,j) * W(i,j) \tag{3.7}$$

where the weight function $W(i,j)$ give the weight 1 to all unmasked pixel inside the galaxy's area and 0 to the other. The right side of Fig. 3.2 shows a sketch of this reduction. If the galaxy would not have been aligned as described in Sect. 2.3, an integration bin

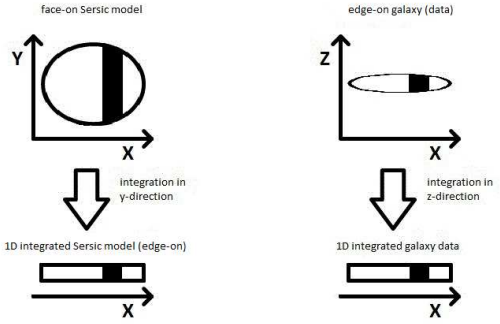

Figure 3.2: Sketch of the Data and Model Reduction from 2D to 1D
The plot shows the halo reduced data for 3.6μm and the 1D fit models with and without an offset.

would not be a simple pixel column, but would have to be defined in a complex way, assigning parts of pixels to different bins. With or without alignment, the image looses sharpness due to the repixellation at some point. Alignment is the much more comfortable and less time consuming way.

The data to both sides of the galaxy center (i.e. the maximum of the 1D data) are averaged, resulting in a 1D radial brightness profile. Propagating the random error of the individual pixels gives the random error of each point in the radial profile. The signal to noise ratios for the total flux of these profiles are shown in Tab. 3.2, where "signal" is the total flux of the whole radial profile and the "noise" is the propagated noise of each point in the profile. The S/N decreased compared with Tab. 2.3 since the halo model emission was subtracted from the galaxy signal.

The left side of Fig. 3.2 shows the sketch of the 1D reduction of the bulge and disk model. Both Sersic models, specified in Sect. 3.4.2, are for face-on galaxies and are already integrated in z direction, as explained in Sect. 3.1.1. Since NGC 7814 is seen edge-on, the models need to be integrated in the line of sight, i.e. y direction, in analogy to the summation of the data in z direction. The cutoff radius for this integration was chosen to be 400 pixels, i.e. the length of the longest radial profile (2MASS data). After this integration, this profile is then averaged on both sides of the center. Doing this, I obtain a 1D radial Sersic model S_{1D} with the same projected radius as the 1D radial profile of the data has.

3.4.2 The 1D Fitting Model

The Sersic model defined in Sect. 3.1.1 have each the parameters amplitude A (in Jy / pixel), scale length R_e (in arcsec), Sersic index n and ellipticity *ellip*. Since I will use the

Wavelength [μm]	1.25	1.65	2.17	3.6	4.5	5.8	8.0	24.
Signal to Noise Ratio	64	53	68	526	351	174	312	37

Table 3.2: Signal to Noise Ratio for 1D brightness profile

The Signal to Noise decreased compared with Tab. 2.3. This is due to the halo removal, which reduced the total flux, but not the noise.

1D projection of these models described in the previous Section, it is suitable to chose a circular Sersic model to create the one-dimensional model from. The Sersic parameter and the scale length in x direction derived for the circular case holds for all other ellipticities as well. Since

$$x^2 + z^2/ellip^2 = const \Rightarrow z^2 = ellip^2 \cdot (const - x^2); \tag{3.8}$$

it is obvious that the ellipticity does not change the shape of the 1D profile. Since all pixel values are simply multiplied with the same factor, a change in the ellipticity will cause only a change in the amplitude for the 1D profile, not in the other fit parameters. This means, a simultaneous fit of both, scale length and ellipticity, is not necessary in the 1D fit. The ellipticity can be fitted later on in the 2D reconstruction (Sect. 3.5), which makes the fit process much easier and saves computation time.

Assuming an exponential disk, the Sersic parameter of the disk is fixed to $n_d = 1$. Therefore, there are five Sersic fit parameters left: the two linear amplitudes A_b and A_d, the two nonlinear scale lengths $R_{e,b}$ and $R_{e,d}$ and the nonlinear Sersic index of the bulge n_b. Including an possible offset o in the model, the galaxy model is:

$$G_{1D} = S_{1D,bulge}(A_b, R_{e,b}, n_b) + S_{1D,disk}(A_d, R_{e,d}) + o \tag{3.9}$$

where $S_{1D,bulge}$ and $S_{1D,bulge}$ are the in analogy to Eq. 3.7 defined 1D radial profiles of the Sersic model bulge and disk, respectively.

3.4.3 1D Fit Method

The 1D fit determines the amplitudes and the scale lengths of the bulge and the disk and the Sersic index of the bulge.

I wrote a routine, which searches a grid of bulge Sersic index values in a range from 0.8 to 4.0 with 0.1 step width. The scale lengths are found iteratively to a precision of 0.1 pixel and the amplitudes are calculated analytically for each grid point, by minimizing the χ^2-function:

$$\chi^2 = \sum_i \frac{G_{1D}(i) - F_{1D}(i))^2}{\sigma_i^2} \tag{3.10}$$

where i is the pixel coordinate (i.e. projected radius), σ_{ij} is the random error on the pixel i. Parameter combinations with negative amplitudes or a bulge scale length greater than the disk scale length are rejected, even if the χ^2 would be smaller for these parameter sets. A disk scale length greater than 300 pixel was rejected, too, since that exceeds the data of IRAC and MIPS, which clearly contain the whole disk (see Sect. 3.4.4 for the derivation of the acceptance criteria).

The starting values for the scale lengths are random and can be reset up to twenty times if no valid parameter set was found. The random errors for the disk scale lengths derived using the Fisher matrix (see Sect. A.2) are larger than 0.1 pixel and a finer determination is not useful since the data is binned in 1 pixel steps.

An iterative approach for the search of the bulge Sersic index is not possible. Since a change in the Sersic index by one step width causes a more drastic change in the model than any other parameter, a final parameter set representing only the local minimum for

this specific Sersic index value would be likely. MacArthur et al. (2003) used a similar fit routine for their analysis. They, too, used an outer loop for the Sersic index for the same reason.

The radial profile of the 5.8μm and the 8μm band show a significantly lower emission at larger radii, which might be due to a shorter disk in these wavelengths (i.e. the emission source does not extent to larger radii). In order to avoid a bias, the 1D fit was only done out to a radius of 180" for these bands. A cutoff radius as additional fit parameter was not introduced in order to keep the model as simple as possible.

3.4.4 Tests of the 1D Fit Method

In order to test the reliability of the 1D fit method, several fits with artificial data are made and the resulting parameter sets are analyzed. The acceptance criteria mentioned in Sect.3.4.3 are developed during these tests. Sect. 3.4.4.1 describes the test with models that have different combinations of the components bulge and disk. The influence of noise on the fit results is analyzed in Sect. 3.4.4.2.

3.4.4.1 Noiseless Artificial Data and acceptance criteria

The functioning of the fit routine itself is checked in several steps. In the first test, the bulge Sersic index is not a fit parameter, but given to the fit method as fixed value, in order to check whether the routine finds the best scale lengths and amplitudes for a fixed bulge Sersic index. In a second step, the routine is then tested with the bulge Sersic index being a fit parameter.

Bulge Sersic index as fixed parameter:

For each 20 different parameter sets, models with a pure Offset, an offset with a disk and an offset with bulge and disk were created with a fixed Sersic index $n = 3.0$. The other model parameters were random (amplitudes between 0 and 1, disk scale length between 0 and 50 and bulge scale lengths between 0 and 10).

All 20 models with a pure offset were found correctly, having amplitudes of the bulge and disk components less than 10^{-9}.

Three of the 20 models with a disk and an offset were not within an amplitude interval of 0.001 and an offset interval of 0.02. A detailed investigation showed that in these cases, the bulge component was fitted in such a way, that it either had the same scale length as the disk or a very high scale length resulting in a more or less constant model value for all radii. In all these cases, the disk scale length was found correctly within the step width of 0.1.

For all 20 models with bulge, disk and offset, the offset was determined correctly within 0.1, for 6 models even within .01. Five models found a scale lengths, that was not within the step width of 0.1 of the true value, however, two of these were only off by 0.11 and 0.13. In case of the other three models, the true bulge amplitude was very small. Therefore, the difference between the true model and the fit with the disk and the offset due to the step widths of the parameter was larger than the bulge itself. The bulge scale length was consequently fitted in a way that the bulge component makes up for the difference in the other two components.

To verify the fit capability for other bulge Sersic indices than $n = 3$, ten models with a random Sersic index ranging between 0.5 and 5.0 were fitted, giving the fit routine the

true Sersic index value as input parameter. The parameter for nine out of the ten models were found correctly. In case of the one model not found, the routine tried to exchange the scale lengths of bulge and disk component and found a local minimum in the χ^2-space.

Bulge Sersic index as fit parameter:

200 models with bulge, disk and offset were analyzed, now the bulge Sersic index being a fit parameter. The input offset was 100%-200% of the total flux of bulge and disk.

For 13 fits, a negative disk amplitude was found which compensated for too high offset values at a local minimum in the χ^2-space. 16 fits found bulge Sersic indices which were more than 0.5 away from the true values. In eleven of these cases, the input bulge flux was less than 15% of the disk flux, therefore the inaccuracy in the disk component due to the step width of the scale length was compensated for by the bulge component. Another ten fits found Sersic indices which were more than 0.1 away from the true values.

These tests with artificial data show drastically that the χ^2-space does have several local minima and that the 1D fit routine is likely to fall into one. This is unacceptable for future analyses of galaxy profiles. Therefore, prior knowledge was installed into the fit routine in form of the following acceptance criteria for fit parameter combinations:

Acceptance criteria

- No negative values for the amplitudes of the disk or the bulge are accepted, not even as intermediate iteration steps.
- The bulge scale length must be smaller than the disk scale length and the maximum value of the disk scale length is 300 pixels.
- New random starting points are used (up to 20 times) if no valid parameter combination was found for the initial parameter set.

All of the misidentified models mentioned above were fitted again. Now, 47 of the 49 models have been identified correctly as a result of these limitations. The remaining two models had a bulge flux of less than 2% and even only 0.03% of the disk flux.

These tests showed the necessity of the acceptance criteria and demonstrated the limit in the detectability of too faint components. They proved the reliability of the 1D fit routine including these criteria for noiseless data.

3.4.4.2 Test with Noisy Artificial Data

After showing that the fitting routine works for noise free data in Sect. 3.4.4.1, I test how the fit results are affected by noise in this section. To do this, I choose the model parameter to be close to the fit results for the 3.6μm data (see Tab. 3.3) in order to test the routine for realistic parameters. For ten different S/N, i.e. the ratio of the integrated galaxy signal and the propagated pixel noise (S/N = 500, 300, 128, 64, 32, 16, 8, 6, 4 and 2), 100 different noise realizations are added to the model and the fit routine estimates the parameters. The mean parameters and their 1σ errors are shown in Fig. 3.3, the solid line in each graph is the true model value.

For all five parameters, the error bars increase with decreasing S/N, as is to be expected. Only the results for S/N=4 and S/N=2 show a severe spread, S/N=8 and S/N=6

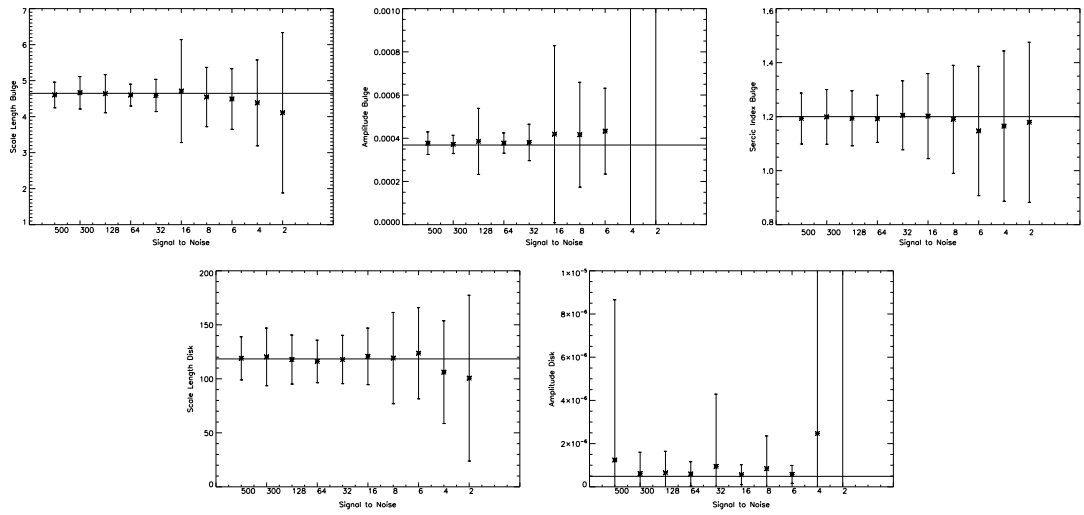

Figure 3.3: Spread of the 1D Fit Parameter with Different Signal to Noise Values These plots show the mean 1D fit parameters found for 100 different noise realizations for ten different signal to noise levels. The straight line represents the true model value.

are somewhat acceptable. The not constant error bars for the high S/N indicate a too small number of different noise realizations for a good statistic. Outliers have a too strong effect on the mean and the error, even though they are just one or two in 100. A test with 1000 different noise realizations per S/N would give clearer results with smaller error bars, since they would be less affected by outliers. However, the test with 100 realizations took already three weeks of computational time, therefore it was unfeasible to increase the number of realizations any further.

Fig. 3.3 shows indications for the degeneracies between the fit parameters. While both amplitudes have the tendency to increase with decreasing S/N, the scale lengths decrease. They demonstrate the anticorrelation discussed in Sect. 3.4.6 and Tab. 3.4. The tendency of the amplitudes is most likely due to the fit criteria, which do not allow negative amplitudes. If the spread around the true amplitude is big enough to possibly cause negative amplitudes, an imbalance to the positive side is created, affecting the mean amplitude found. The scale length responds to this imbalance due to the anticorrelation.

All in all, this test shows that the fit routine finds a parameter set which agrees with the true model values within the error bars. Especially for the S/Ns of the data (see Tab. 3.2), the tests confirm that the fit routine finds the global minimum in the χ^2-space.

3.4.5 Redundancy of the Offset Parameter

In order to give the fit routine the capability to fit data including a flat background , an additional offset fit parameter was introduced. For all eight wavelengths, the 1D fit of the halo-subtracted data was done with and without this offset parameter. The result for the example of 3.6μm is shown in Fig. 3.4. Comparing the models with and without offset, the bulge Sersic index changed by 0.1 only in the cases of 5.8μm and 8μm and all bulge scale lengths stayed the same within the step width of of 0.1 pixel, which can be simply caused by different starting points. The integrated bulge emission for the model with offset was identical with the emission for the model without offset. The only significant difference in these two models is the disk scale length, with is higher for the model with offset. The correlation of 0.6 between disk scale length and offset, derived with the Fisher

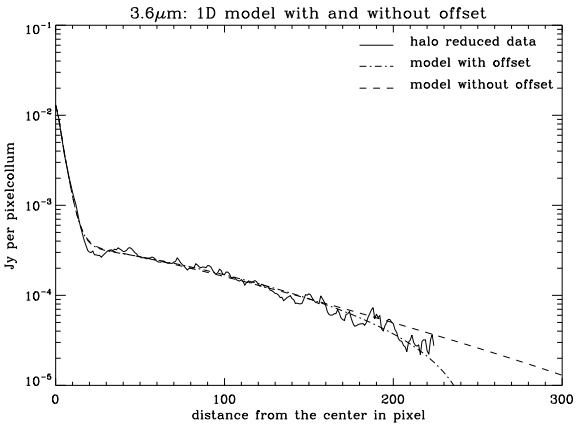

Figure 3.4: 1D Model with and without Offset
The plot shows the 1D halo-subtracted data for 3.6μm and the 1D fit models with and without an offset. Only for large radii is a difference in the two models noticeable, even though it is still of the order of the data noise.

λ [μm]	n_b	$R_{e,b}$ ["]	A_b [Jy]	$R_{e,d}$ ["]	A_d [Jy]
1.25	1.1 ± 0.1	5.94 ± 0.10	$(3.09 \pm 0.08) \cdot 10^{-4}$	176.0 ± 11.2	$(3.41 \pm 0.34) \cdot 10^{-7}$
1.65	1.2 ± 0.1	6.05 ± 0.10	$(5.16 \pm 0.15) \cdot 10^{-4}$	145.2 ± 10.4	$(7.47 \pm 0.9) \cdot 10^{-7}$
2.17	1.2 ± 0.1	5.38 ± 0.10	$(4.78 \pm 0.16) \cdot 10^{-4}$	111.3 ± 7.6	$(8.92 \pm 1.09) \cdot 10^{-7}$
3.6	1.2 ± 0.1	5.46 ± 0.12	$(3.54 \pm 0.02) \cdot 10^{-4}$	144.2 ± 0.9	$(5.04 \pm 0.06) \cdot 10^{-7}$
4.5	1.1 ± 0.1	4.89 ± 0.12	$(2.13 \pm 0.02) \cdot 10^{-4}$	142.0 ± 1.2	$(3.17 \pm 0.05) \cdot 10^{-7}$
5.8	1.1 ± 0.1	5.65 ± 0.12	$(2.24 \pm 0.03) \cdot 10^{-4}$	130.8 ± 3.3	$(4.88 \pm 0.21) \cdot 10^{-7}$
8.0	1.0 ± 0.1	5.88 ± 0.12	$(2.00 \pm 0.02) \cdot 10^{-4}$	110.1 ± 1.0	$(1.01 \pm 0.17) \cdot 10^{-7}$
24	0.8 ± 0.1	7.15 ± 0.25	$(3.00 \pm 0.03) \cdot 10^{-4}$	148.5 ± 18.3	$(1.09 \pm 0.24) \cdot 10^{-6}$

Table 3.3: 1D Fit Parameters with Fisher Matrix Errors to Bulge and Disk of NGC 7814
Table with all 1D fit parameters for all eight wavelengths. The scale lengths are in units of arcsec. The error of the bulge Sersic index and the bulge scale length are the smallest possible steps of the fitting grid. The bulge Sersic index hits the lower fitting limits for 24μm. Therefore, the Fisher matrix does not give an error estimate for the bulge at this wavelength. The error for the bulge amplitude of 24μm was estimated from the value at 8μm and the relation of the disk scale length in 24μm and 8μm.

matrix, explains this change.

There is only a small difference in the models shown in Fig. 3.4 within the area covered by the data. Real differences are only noticeable for large radii with no data coverage, even though these differences are sill in the order of the data noise. Since the model with offset has one fit parameter more, it must have a slightly smaller χ^2. However, the data does not support the need of this additional parameter. Therefore, it was removed from the fit routine (i.e. $o = 0$ in Eq. 3.9) in order to keep the model as simple as possible.

3.4.6 Fit Results for Bulge and Disk of NGC 7814

The fit parameters are presented in Tab. 3.3 and the radial profiles with the fitted models are shown in Fig. 3.6. The models are a good description of the data. Due to the log scale of the Y-axis, the negative data values are not shown in these plots, which gives the wrong impression of an underestimation of the data by the model for long radii.

For the wavelength from 1.25μm - 8μm, the bulge parameters scale length and Sersic index are similar or even identical within the parameter errors. The weighted mean is 1.1 for the Sersic index and 5.6 for the scale lengths. This is well above the FWHM

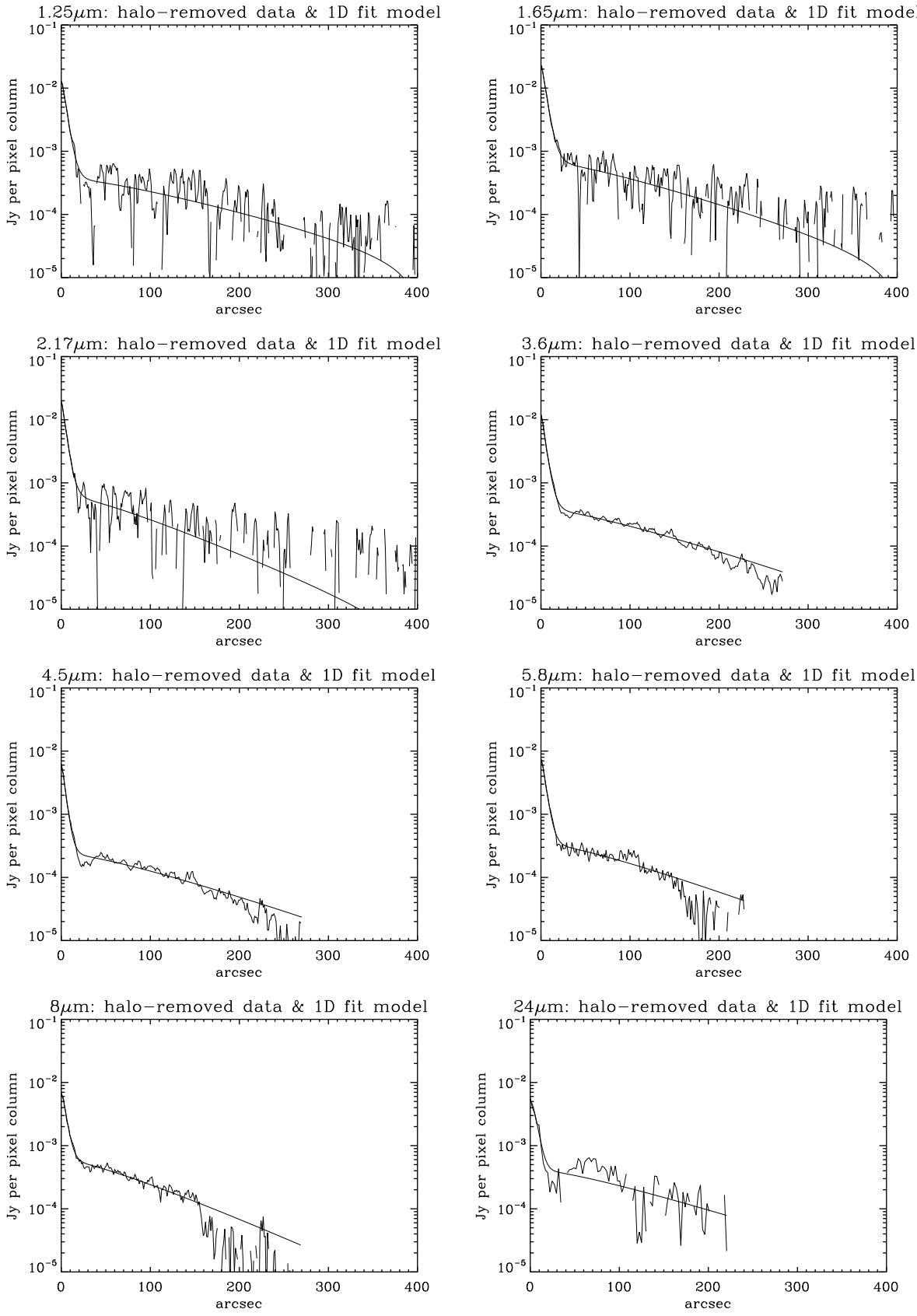

Figure 3.5: 1D Fits to the Halo-subtracted Data

The plots show the halo-subtracted radial profiles for all the eight wavelengths and the fitted model with an exponential disk and a bulge with variable Sersic index. No negative pixel values are plotted due to the log-scale of the y-axis. Especially the 2.17μm therefore looks like a not good fit, even though it is.

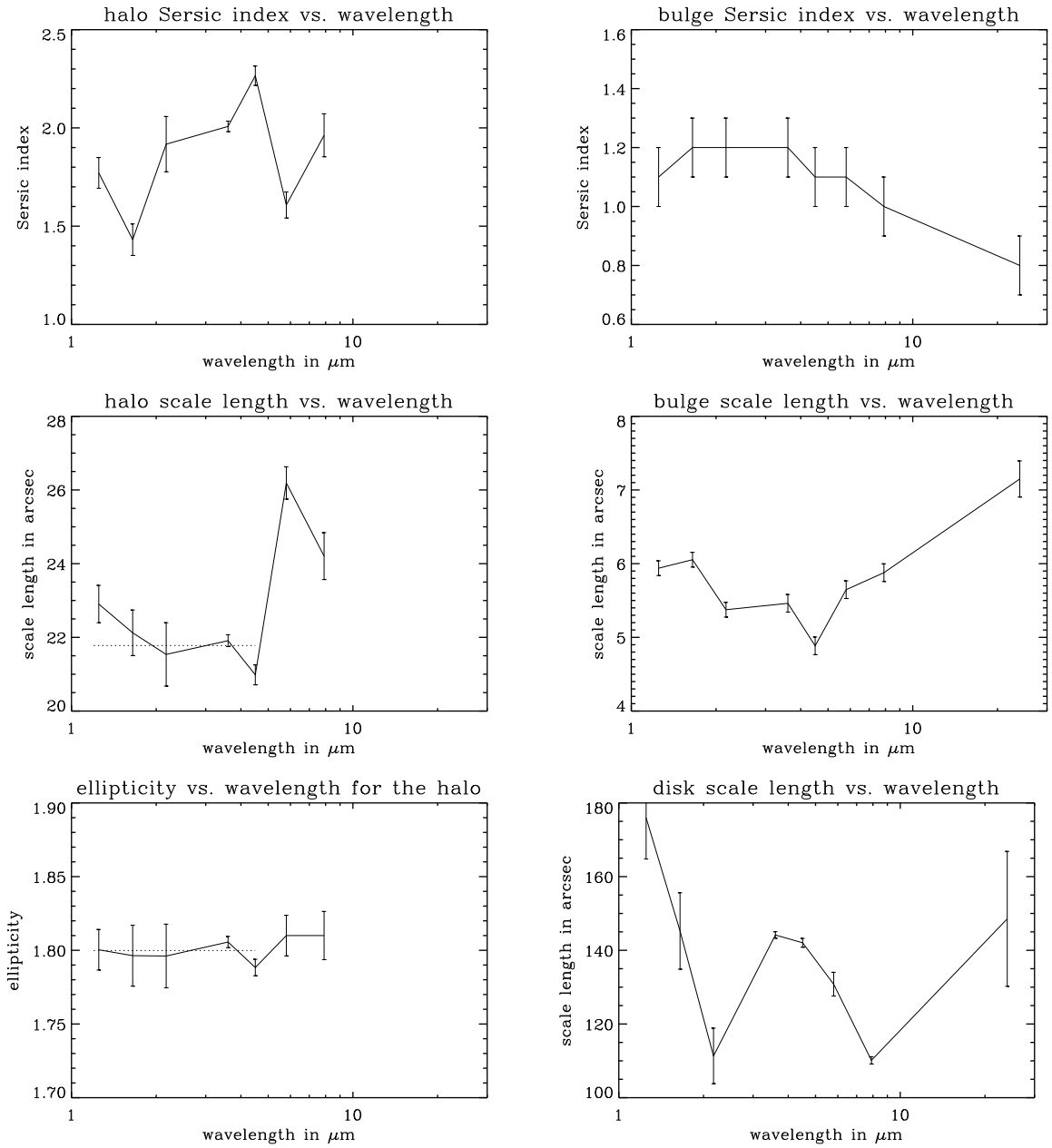

Figure 3.6: 1D Fit Parameter

These plots show the distribution of the 1D fit parameter vs. wavelength. Left column: Sersic index, scale length and ellipticity of the halo. The 24μm parameters are not displayed since a constrained fit for the halo was done at this wavelength (see text). Right column: Sersic index and scale length of the bulge and scale length of the disk. None of these parameters show a clear trend with changing wavelengths.

HALO	$R_{e,h}$	*ellip*	n_h	A_h
$R_{e,h}$	0.160	-0.001	-0.004	$-9.984\cdot10^{-8}$
ellip	-0.001	0.004	0.296	0.395
n_h	-0.004	0.296	0.027	0.918
A_h	$-9.984\cdot10^{-8}$	0.395	0.918	$6.251\cdot10^{-7}$

BULGE & DISK	n_b	$R_{e,b}$	A_b	$R_{e,d}$	A_d
n_b	0.006	$-5.204\cdot10^{-6}$	$-1.106\cdot10^{-9}$	0.001	$-9.22\cdot10^{-12}$
$R_{e,b}$	$-5.204\cdot10^{-6}$	0.007	-0.911	0.260	-0.325
A_b	$-1.106\cdot10^{-9}$	-0.911	$1.04\cdot10^{-6}$	-0.237	0.300
$R_{e,d}$	0.001	0.260	-0.237	0.740	-0.947
A_d	$-9.22\cdot10^{-12}$	-0.325	0.300	-0.947	$5.238\cdot10^{-9}$

Table 3.4: Random Errors and Correlations for 3.6μm Estimated with the Fisher Matrix These matrices derived from the Fisher matrix have the 1σ error of the parameters in their diagonal and their correlations (not covariances as in the Fisher matrix!) in their off diagonal elements. Note the sigma scale length is in units of pixel (i.e. 1.2 arcsec for IRAC data).

of the PSF for 2MASS and IRAC (see Sects. 2.1.1 and 2.1.2) and therefore, the bulge model is fitted to not a a resolved bulge rather than to a point source. However, the PSF of the 24 μm MIPS band is with 6" significantly larger than the PSF of the IRAC bands. The high scale length and the low Sersic index for the are due to this high PSF, making the bulge broader and less sharp in the center. The parameter error, derived from the curvature of the χ^2 hypersurface using the Fisher matrix, are dominated by the step width of the fitting algorithm. The scale lengths of the disk exhibits a larger spread in these wavelengths. Due to the large error, the most of the values are still similar and the weighted mean is 132". The scale length derived by van der Kruit & Searle (1982) from optical and j band data is 115" and lies within the spread of these fit results.

The correlations (see Sect. A.2) between the parameters for the bulge and the disk are almost identical in all wavelengths (see Tab.3.4 for the example for 3.6μm). Both, disk and bulge scale length have a high anticorrelation of -0.95 and -0.91, respectively, with their amplitudes. An increase in the scale length increases the model value at each pixel, especially in the outskirts, which is then compensated by a lower amplitude. It is evident from Tab. 3.3 as well. Therefore, it is not meaningful to interpret the scale length itself or its change with wavelength without considering the amplitude at the same time. The correlations of the parameters of bulge with the disk parameters are weaker (about 0.3). There is an anticorrelation between the scale length of one and the amplitude of the other component, since both scale lengths and amplitudes have a positive correlation with the same parameter of the other morphological component. The bulge Sersic index has almost no correlations and can be considered as independent.

For the fit to the 24μm data, the bulge Sersic index hits the lower limit, since a profile which looks more like a Gaussian rather than an exponential at low radii is preferred due to the large PSF. This causes the Fisher matrix to not find a valid value for the bulge parameter errors, since the matrix does not take into account the parameter limits and therefore does not recognize this minimum in the χ^2 space. The error in the bulge Sersic index and the scale lengths are still determined by the fitting grid, and the error in the bulge's amplitude was estimated from the IRAC bulges amplitude errors. The disk fit is not affected by the PSF of the image, since the disk is extends to large radii.

Wavelength	halo [Jy]	bulge [Jy]	disk [Jy]
1.25	0.749 ± 0.051	0.136 ± 0.008	0.113 ± 0.016
1.65	0.783 ± 0.069	0.245 ± 0.014	0.178 ± 0.031
2.17	0.724 ± 0.086	0.179 ± 0.011	0.130 ± 0.024
3.6	0.386 ± 0.009	0.095 ± 0.006	0.080 ± 0.002
4.5	0.249 ± 0.010	0.044 ± 0.003	0.049 ± 0.002
5.8	0.209 ± 0.011	0.062 ± 0.004	0.063 ± 0.005
8.0	0.153 ± 0.012	0.057 ± 0.004	0.098 ± 0.003
24.	0.066 ± 0.031	$0.028 \pm 0.005*$	0.042 ± 0.015

Table 3.5: Total Emission of the Components with Errors

This table lists the total flux of each of the morphological components of NGC 7814. All three have a clear detection in all the wavelengths. The 24μm components have higher errors, but are still detected. Errors marked with * were estimated from the IRAC wavelengths, see text for detail.

The total flux of all three morphological components are listed in Tab. 3.5 and shown in Fig. 4.1. All three components are clearly detected in all wavelengths. These values will be discussed in Sect. 4.1 in particular and further analyses will be done in Chapter 4.

3.5 2D Image Reconstruction of the Bulge and the Disk from the 1D Fits

In Sect. 3.3 and 3.4, the parameters for the 2D halo model and the 1D bulge and disk model were derived. In this section, I will make a brief 2D reconstruction of the bulge and the disk from these 1D fit parameters. This reconstruction has only the purpose to get a first impression of the vertical (z-direction) structure of the disk. It is not needed to derive the MIR SED. Therefore, a very simple model is adopted.

In Sect. 3.1.1, I presented the Sersic profile and its parameter: the Sersic index, the scale length, the ellipticity and the amplitude. For the bulge and the disk, I already derived the values of both Sersic indices, both scale lengths and both amplitudes. The disk does not need an ellipticity, since NGC 7814 is an edge-on galaxy. However, I must adopt a model for the vertical structure of the disk. Wainscoat et al. (1989) discuss the merit of an exponential vertical profile for a disk vs. a $sech^2$ vertical profile in general and specifically for the galaxy IC 2531, favoring the exponential model. I chose to use an exponential model, following Wainscoat et al. As the images show some evidence for flaring of the disk, I allowed the scale height to vary linearly with projected galactocentric radius. A constant scale height would cause the inner regions, which have a higher emission, to extend much further above the disk plane than the outer regions, resulting in a more or less diamond shape in z rather than a flat disk. This too large extent in z direction is avoided with the assumption of a increasing scale height with radius. Saha et al. (2009) report in their study the 4.5μm emission from edge-on galaxies with Spitzer data, that they could not reproduce their observations with an exponential z profile of the disk for ten galaxies with warped disks, but needed a model with a flaring disk.

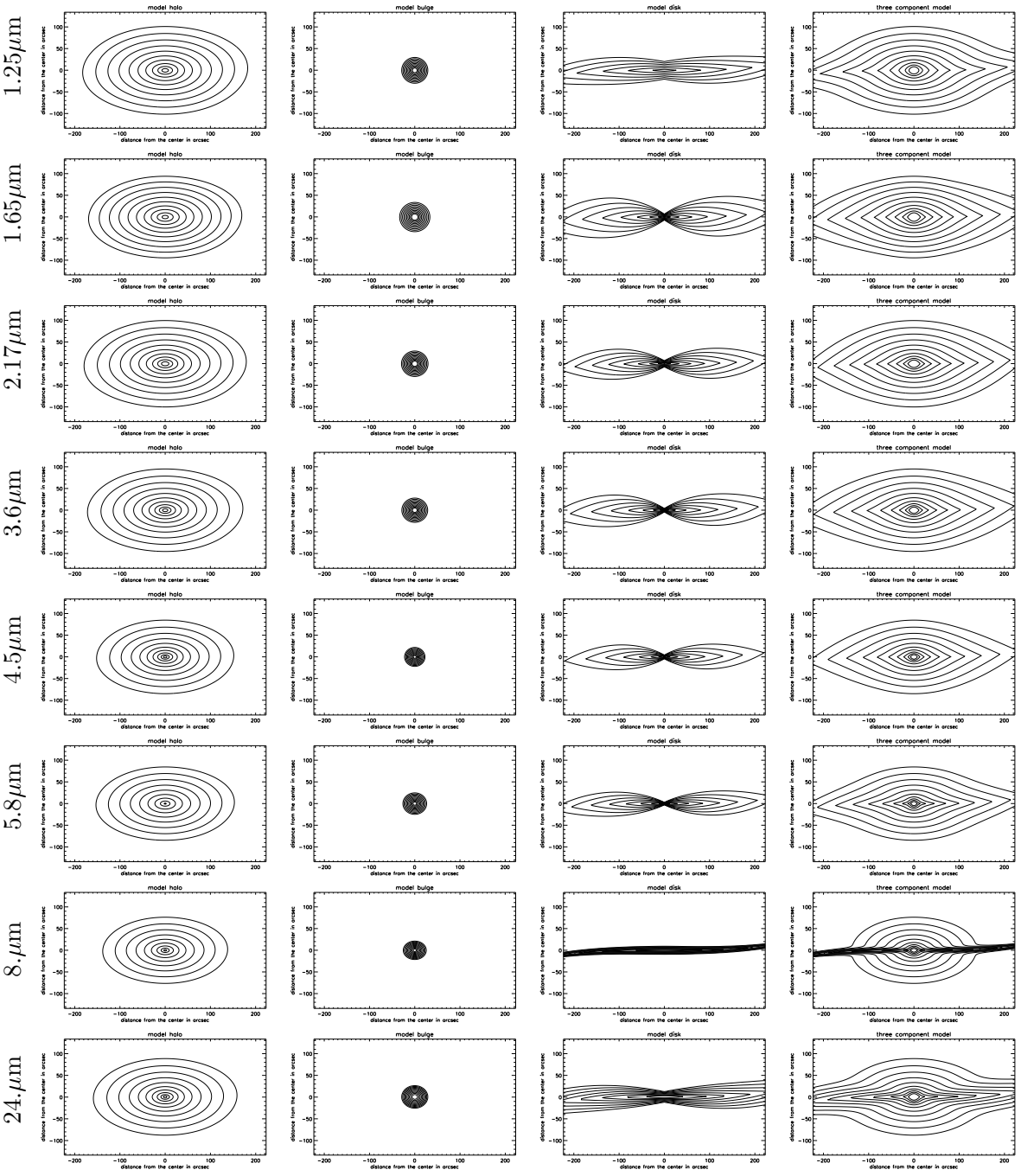

Figure 3.7: 2D Fit Model Components

This is a 2D reconstruction of the three model components in each wavelengths: left the halo, second from the left the bulge, second from the right the disk and on the right the whole model. The same logarithmic contours levels are plotted in all plots with the highest contour of 0.32*max(halo 1.65μm) and a logarithmic factor of two. The halo was directly derived in 2D. The 2D bulge has only the additional parameter ellipticity compared to the 1D bulge. The disk model assumes an exponential z profile with increasing scale height with increasing radius. The models were fitted to the data still convolved with the PSF.

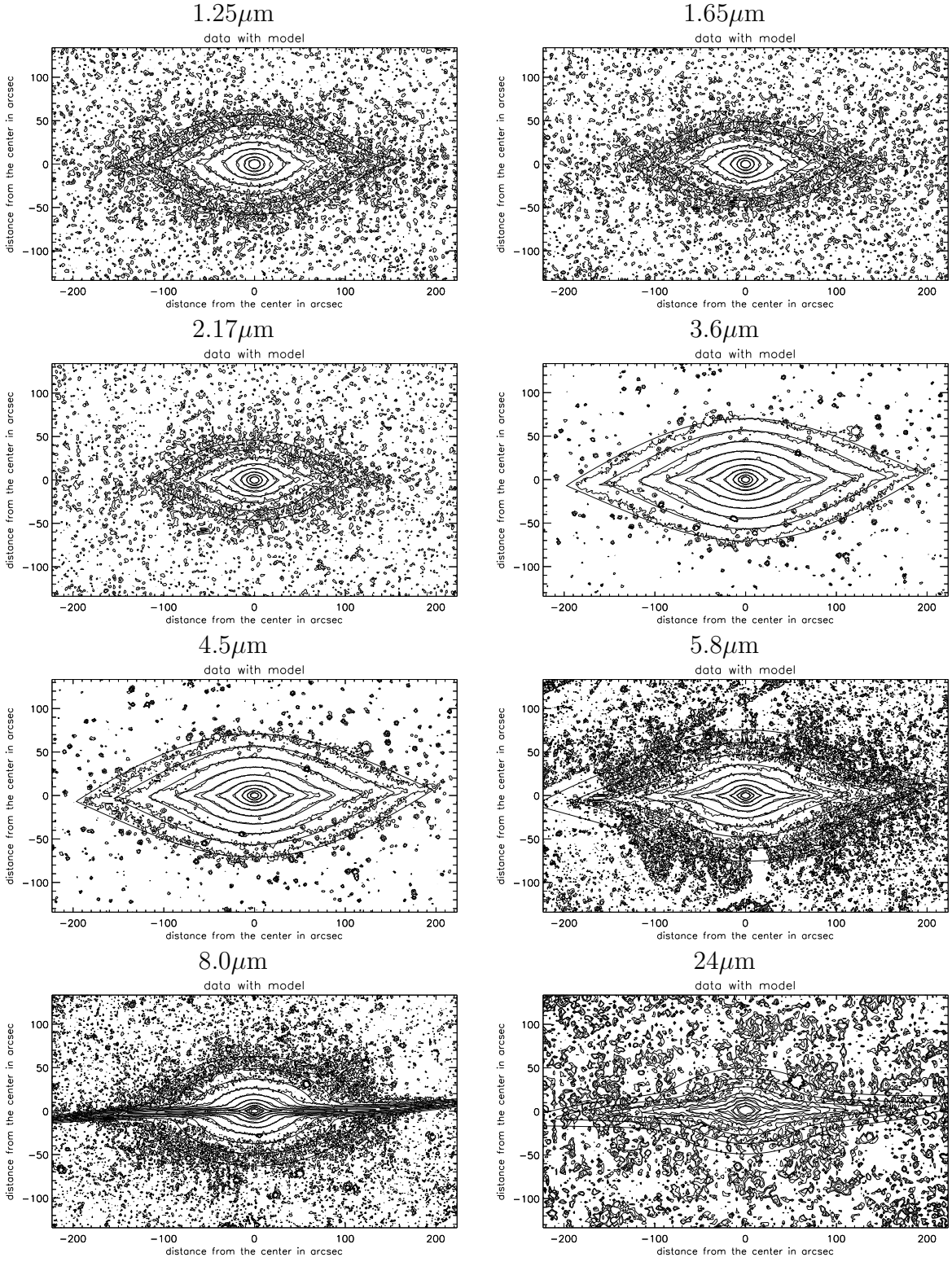

Figure 3.8: Data with 2D Model Reconstruction

These plots show the data with the 2D model for logarithmic contour level in fractions of the maximum brightness and a logarithmic factor of two. The number of contours depends on the noise level of the data. All eight wavelengths show a good agreement of the fit model with the data.

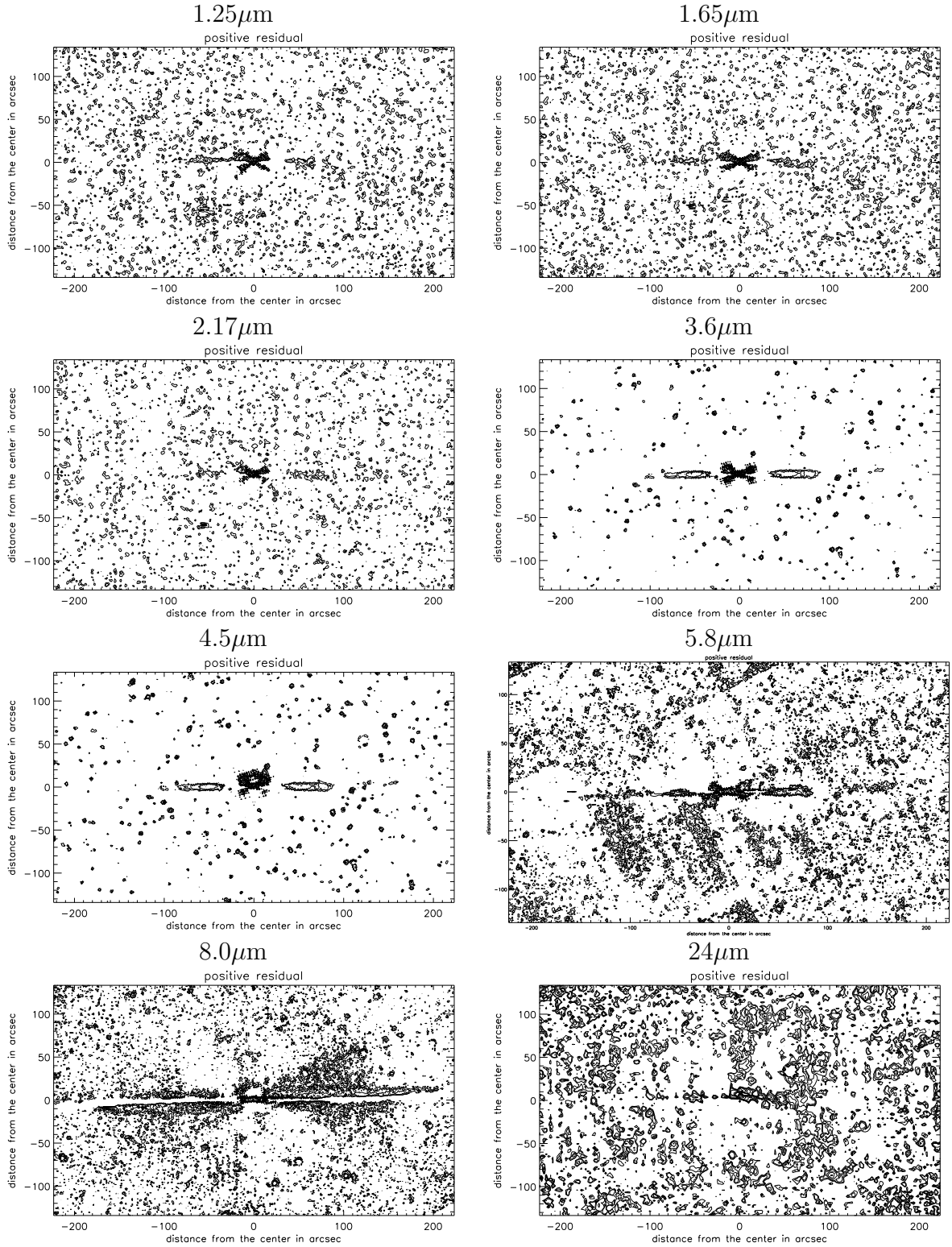

Figure 3.9: 2D Positive Residuals

These images show the positive residuals of the galaxy model and the data. The same contour levels as in Fig. 3.8 are used. It is obvious that the disk model is too bright in the disk plane and that the bulge is not a pure ellipse as the model is. See text for further discussion.

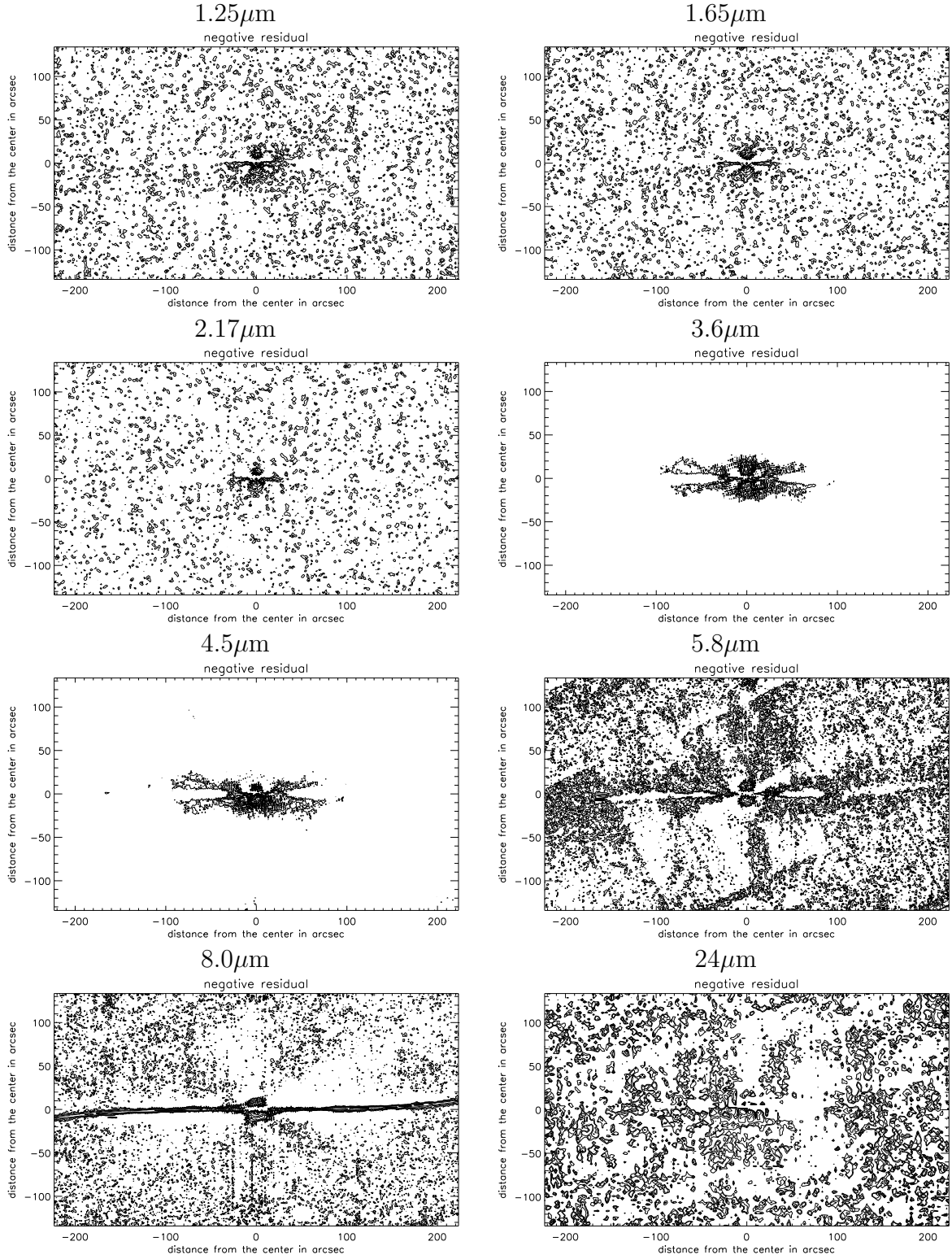

Figure 3.10: 2D Negative Residuals

These images show the negative residuals of the galaxy model and the data, complementary to Fig. 3.9. The same contour levels as in Fig. 3.8 are plotted. Here, it is noticeable that the disk model is too low in the regions above and below the disk plane. Again, it is evident that the bulge is not a pure ellipse as the model is. See text for further discussion.

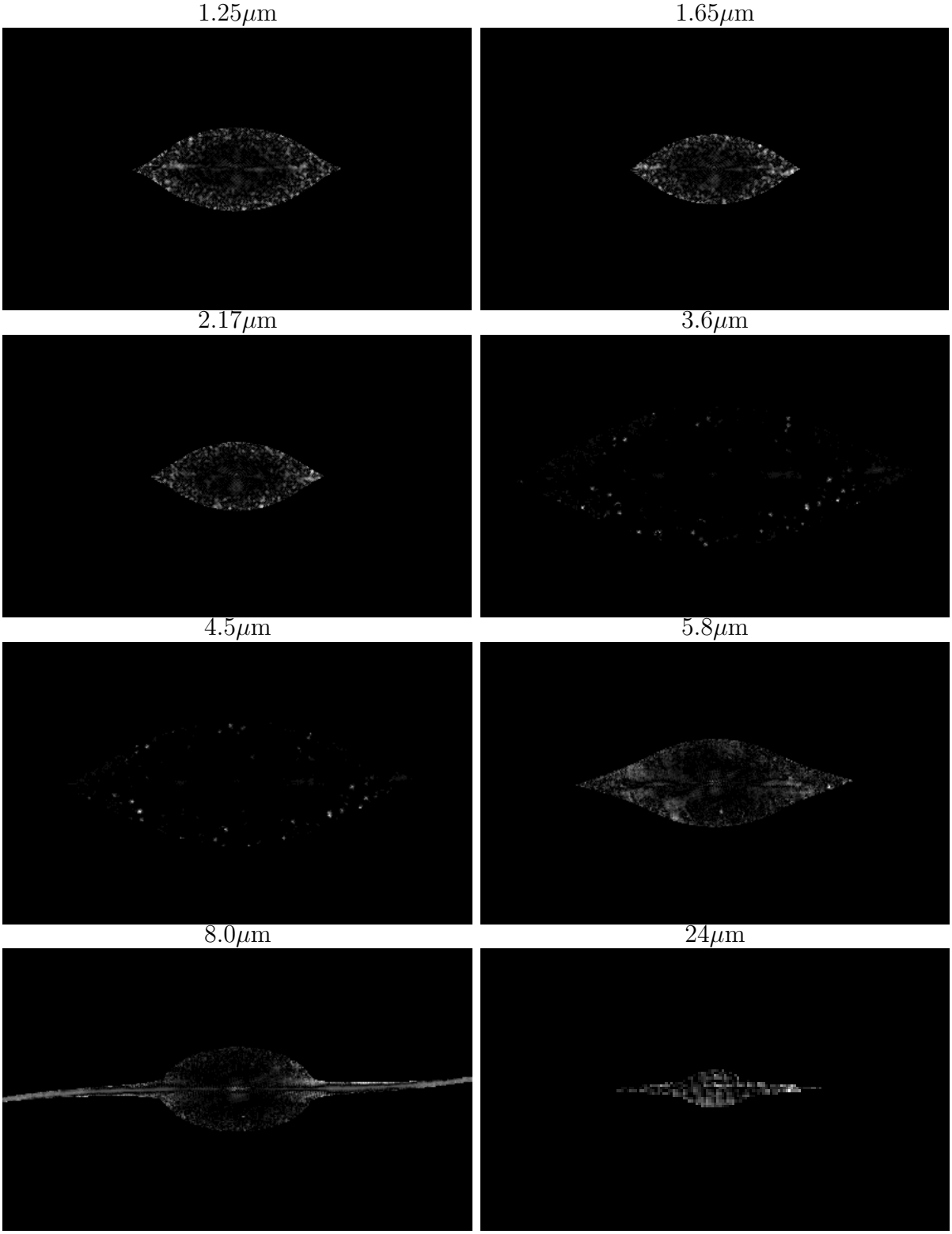

Figure 3.11: 2D Percentile Absolute Residuals

Within a region where the galaxy model is larger than three times the pixel noise, the percentile difference between the data and the galaxy models is shown. The percentile difference is dominated by the noise features for all wavelengths. The maximal difference in each image is white, no difference is black.

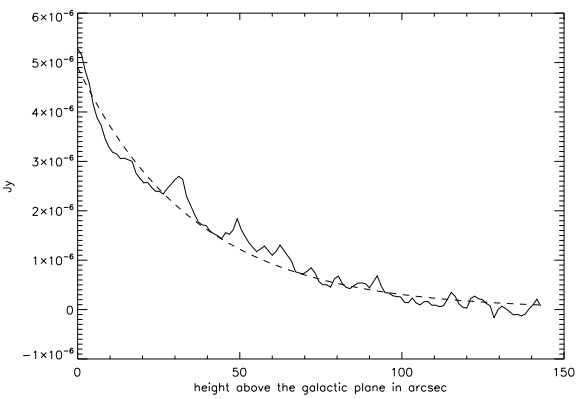

Figure 3.12: Z Structure of the Disk at 3.6μm
The z structure of the disk is presented by the solid line, which represents the coadded pixel rows of the map after subtraction of the halo at 3.6μm. The coadding is done in the range 120" - 240" in distance from the center to avoid contamination with bulge light. The dashed line is the exponential with a scale height of 36" (1.2", i.e. 1 pixel, corresponds to 85pc), which was used as z profile in the disk model. It is obvious that this is only an insufficient description of the data for small heights.

The amplitude of the bulge and disk emission was already derived in the 1D fits (Sect. 3.4). Therefore, the integrated emission of each z-profile is fixed to the emission derived from the 1D fit at the same projected radius. Using this model, there are three unknown fit parameters in the 2D reconstruction: the disk scale height, its variation in projected galactocentric radii and the ellipticity of the bulge. The halo was already derived in 2D (Sect. 3.3). This model is fitted to the background-subtracted data, minimizing a χ^2-function (see Sect. A.1). A convolution of the model with the PSF was not done.

Fig. 3.7 displays synthetic images of the best fit of the three model components and of their summation. The contour lines are logarithmic with the highest level being 0.32 times the maximum of the halo component in the 1.65μm band and a logarithmic factor of two. The galaxy model, being the summation of the three components halo, bulge and disk, is shown in the right column. In the left row, one can see very well the decreasing flux of the halo component with wavelength. The bulge shown in the second column from the left has a very sharp peak and only a small spatial extent. At all wavelengths, the bulge is very round, unlike the halo.

The disk models are presented in the second column from the right. For galactocentric radii around 50", the disk scale height is about 700pc for the small wavelengths, increasing linearly with radius. The scale height decreases slightly with wavelengths from 1.25μm to 5.8μm and drops significantly at 8μm. While the shorter wavelengths are dominated by emission from stars, which have a higher scale height h_s ≈400pc (mean value found by Xilouris et al. (1999)), the 8μm and the 24μm bands are dominated by the emission from dust, which has scale heights of 200pc (Xilouris et al. 1999). The PSF (Hora et al. 2008) at this wavelength has a FWHM of 1.9" (∼135pc), which is of the order of the disk scale height found in the 2D fit at this wavelength. The fit to the 24μm image has a much larger disk scale height, since the PSF in this image is 6" (SOM 2007), causing the dust lane to be unresolved. While the disk has about the same extension as the bulge at short wavelengths, the fit to the 8μm image shows a bulge which extends clearly above the disk.

Fig. 3.12 shows how the averaged emission decreases with height above the disk. The emission was averaged over a range of projected galactocentric radii of 120" to 240" to both sides above and below the disk plane for the halo-subtracted data at 3.6μm (solid line). In these averages, I applied weights according to the S/N in each pixel column. In this range, the bulge emission is negligible. The dashed line is the fitted exponential with a scale height of 36", i.e. 2.5kpc. It is obvious, that the exponential profile used underestimates the profile directly in the disk plane, overestimates it at a height around

20". This demonstrates that a single exponential is an insufficient representation for the vertical structure of the disk at small heights. A model with two exponentials or a combination of an exponential and a Gaussian, physically representing a thick stellar disk and a thin disk of ISM or just two stellar disks, might be a better choice. Nevertheless, the fit of the exponential shown in Fig. 3.12 suggests a good first approximation.

Fig. 3.8 shows the galaxy fits with the data as logarithmic contour lines (fractions of the galaxy's maximum in each band). The fits look very good. Figs. 3.9 and 3.10 show the positive and negative residuals, respectively. The inner region, i.e. the region of the bulge, exhibits too high model values in the diagonal directions and too low model values above and below the galaxy plane. This indicates that the true shape of the bulge is not elliptical, but rather more elongated in z direction and more edgy. The difficulties in reproducing the z profile of the disk was already discussed above.

To place these imperfections in the context of the good global fit, Fig. 3.11 shows the percentile differences of galaxy model and data for regions with model values higher than three times the noise level. The different sizes of the considered area result from the different noise levels of the data. For all wavelengths, the highest percentile variances are due to pixel noise. The model deficiencies are noticeable in the percentile differences as well. However, Fig. 3.11 suggests an acceptably small effect on the galaxy fit. Since the 2D reconstruction is not used in the later analysis and was only done to give an impression on the 2D halo-bulge-disk decomposition, another z profile for the disk was not considered. The deficiencies of the 2D reconstruction do NOT effect the reliability of the model parameters and fluxes previously derived in Sects. 3.3 and 3.4. They result from the z model used for the bulge and the disk only.

Chapter 4

Analyzing the Spectral Energy Distribution

I have completed the halo-bulge-disk decomposition in Chapter 3. In this chapter, I will analyze the resulting spectral energy distributions (SEDs) of the three morphological components. In Sect. 4.1 I will briefly describe the SED. In order to draw preliminary conclusions about the physical origin of the emission in the galaxy components, the direct star light must be subtracted which will be described in Sect. 4.2. The resulting residual SEDs will be presented in Sect. 4.3 and possible sources of the residual emission will be discussed.

4.1 SEDs of Halo, Bulge and Disk

The decomposition of the structure of the galaxy results in the SEDs shown in Fig. 4.1. The bulge and the disk components have emission components of similar luminosity. Both exhibit a bimodal distribution, with one peak at 1.65 μm and the other at 8 μm (disk) and 5.8 μm (bulge). The minimum is at 4.5μm. While the short wavelength peak of the bulge is higher than for the disk, the long wavelength peak of the disk is higher. This bimodality indicates the presents of at least two different physical processes, which can have different strength for the disk and the bulge. The halo has only a single peak at 1.65 μm, with the SED values falling off towards the long wavelengths gradually. This indicates different physical conditions in the halo than in either the bulge or the disk. The halo emission is approximately a factor five higher than the bulge or the disk emission in the four shorter wavelengths. In the long wavelength range, where the bulge and the disk have their second peak, the halo emission is roughly twice the emission of the bulge or the disk, decreasing with increasing wavelength.

All three morphological components are clearly detected in all wavelengths. In the 24μm band, where the spatial resolution and the detector performance are less good, the error bars are much larger than in the other bands. However, even here, the SED values are clearly NOT compatible with zero. Remarkably, the 24/8 μm colors of all three morphological components are comparable.

The galaxy emission is composed of a stellar component, which is dominating at shorter wavelengths, and a second component, dominating at longer wavelengths. In case of the disk, this second component is commonly considered (e.g. Soifer et al. (2008)) to be interstellar dust emission. Both the bulge and the disk SEDs are reddened by dust, in particular in the J-band, which may explain the redder J-H colors seen in the bulge

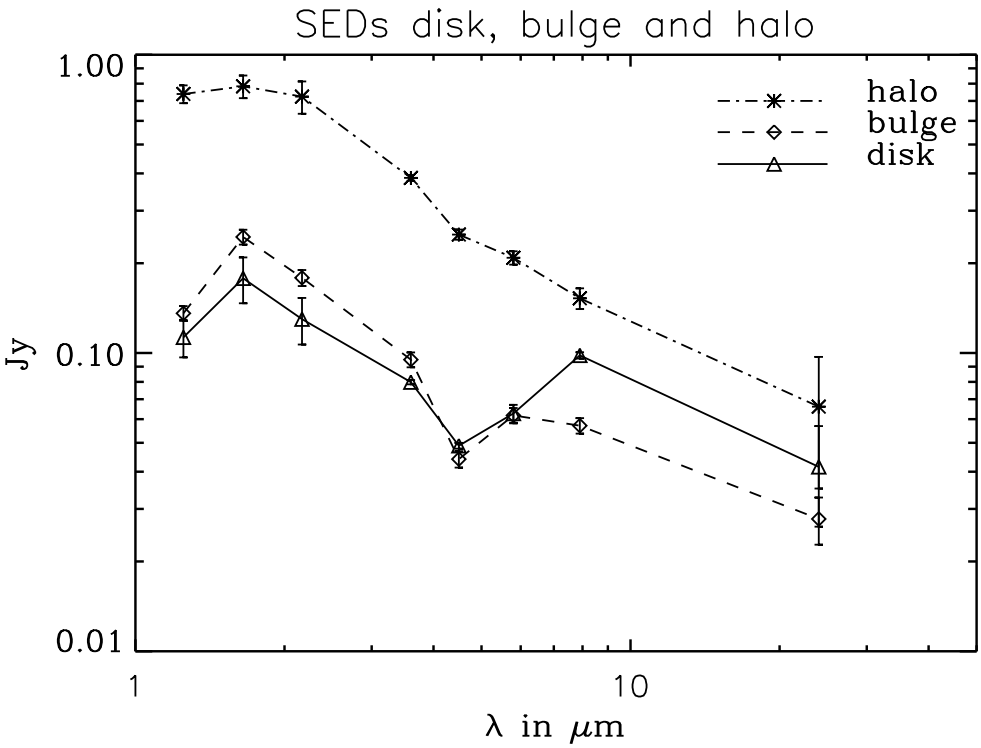

Figure 4.1: SED of Halo, Bulge and Disk
This figure shows the change of the total emission of each morphological component with wavelength. The bulge and the disk show a similar behavior with two peaks and a minimum at 4.5μm. The Halo exhibits only a single peak without a prominent minimum at 4.5μm.

and the disk in comparison with the halo. Neither the halo nor the bulge SED exhibit a Rayleigh-Jeans-behavior at long wavelengths, which rules out the hypothesis of a pure stellar emission from stars hotter than ∼1000K causing their SED. The bulge and the halo are believed to have little or no interstellar medium, since neither component has an obvious HI counterpart (Hameed & Devereux 2005). In order to analyze the unknown second component of the SEDs, the stellar component must be subtracted carefully from each SED individually.

4.2 Removal of the Starlight

The analysis of the unknown non-stellar component[1] in the SEDs in Fig.4.1 depends on the quality of the starlight removal. The basic strategy to remove the starlight is to use a model for this emission component derived from population synthesis calculations. The short wavelength (NIR) measurements are used to fix the amplitude of the model for all wavelengths.

There are obstacles which need to be considered along the way: First, the dust in the galaxy absorbs and scatters a fraction of the starlight, complicating the assessment of the amplitude of the stellar emission component. Section 4.2.1 describes how this effect is

[1]In the following, I will refer to 'stellar' and 'non-stellar' as denoting emission from the photosphere of stars. For example, 'non-stellar' emission could include emission from circumstellar dust, even though this component is physically related to the stars.

wavelength [μm]		1.25	1.65	2.17	3.6	4.5	5.8	8.0	24.0
bulge	τ =0.25	0.389	0.298	0.190	0.075	0.048	0.033	0.050	0.032
bulge	τ =1.00	0.862	0.734	0.468	0.185	0.118	0.082	0.122	0.079
bulge	τ =4.00	1.406	1.511	0.963	0.381	0.243	0.169	0.252	0.163
disk	τ =0.25	0.149	0.084	0.053	0.021	0.013	0.009	0.014	0.009
disk	τ =1.00	0.420	0.307	0.196	0.078	0.050	0.034	0.051	0.033
disk	τ =4.00	0.865	0.797	0.508	0.201	0.128	0.089	0.133	0.086

Table 4.1: Bulge and Disk Reddening (Δm in Magnitudes) for Different B-band Disk Optical Depths τ at all Wavelengths

corrected for and the original galaxy emission without dust attenuation is reconstructed. Second, the choice of the specific stellar model for the population synthesis calculation is important, including parameters such as stellar age and metallicity. It is not enough to just subtract a Rayleigh-Jeans-law representing the blackbody tail of the stellar light, which would be a too rough approximation of the stellar spectrum in the NIR. Rather, I used a population synthesis stellar light model developed by Cordier et al. (2007), discussed in Sect.4.2.2.

4.2.1 Correction for Dust Attenuation

Dust present in the line of sight absorbs or scatters part of the light emitted. Since the distribution of emitters is extended, the wavelengths dependence of the attenuation differs from the extinction curve for a point source. Therefore, the decrease of the galaxy emission due to dust with respect to geometry is referred to as "attenuation", rather than as "extinction".

The dust in the disk affects the disk and the bulge light. Since the halo was derived above and below the disk only (see Sect. 3.3.1), no diffuse disk dust is expected to be in the lines of sight which could cause attenuation. Even if halo dust is found in the later analysis, the halo will still be an optically thin medium with negligible attenuation due to its size and the resulting low density of the dust. Therefore, only the disk and the bulge need to be corrected for dust attenuation.

The short wavelengths (i.e. 2MASS data) suffer most from dust absorption; IRAC data will only have small attenuation loss. Tuffs et al. (2004) derived the attenuation of the bulge and the disk emission of spiral galaxies for different inclinations and optical depths of the disk. The intrinsic flux density S^0_λ can be restored using their Eqs. 7 and 10:

$$\Delta m_\lambda = -2.5 \cdot \log_{10} \frac{S_\lambda}{S^0_\lambda}$$

$$S^0_\lambda = S_\lambda \cdot 10^{\frac{\Delta m_\lambda}{2.5}} \tag{4.1}$$

where S_λ is the apparent flux density of a galaxy or of its component, and Δm_λ, containing the information about the attenuation, is tabulated in the paper.

I used their (nonpublic) routine which provides dust attenuation values for specific wavelengths, inclinations and optical depths. In the wavelength interval of the galaxy's data, attenuation values are only provided for $\lambda \leq 2.17\mu$m. Therefore, the values for the

attenuation of the IRAC and MIPS bands longward of K band were interpolated

$$\frac{\Delta m_\lambda}{\Delta m_{(2.17\mu m)}} = \frac{c_\lambda}{c_{(2.17\mu m)}} \tag{4.2}$$

using the extinction distribution values c of Weingartner & Draine (2001) derived for the Milky Way and the attenuation value of the longest wavelength given by Tuffs et al. Using extinction rather than attenuation in this extrapolation is a good approximation as scattering is negligible at these wavelengths, as we are in an optically thin regime. Since the corrections are multiplicative, the errors of the SEDs were changed in the same way. Using the results for edge-on galaxies (i.e. inclination $i = 90°$), correction factors for different optical depths τ were derived (see Tab. 4.1). In this thesis, τ refers to the face-on B-band optical depths (see Tuffs et al. (2004)).

Tuffs et al. (2004) tabulate a τ range between $\tau = 0.1$ for extremely optically thin and $\tau = 8.0$ for moderately optically thick cases. I used $\tau = 0.25$, $\tau = 1.0$ and $\tau = 4.0$ to demonstrate the effect of this parameter on the SEDs. As I will show later on in Sect. 4.2.3 and Fig. 4.4, the τ of NGC 7814 lies in this lower τ range.

4.2.2 Specifying the Shape of the Stellar SEDs in the NIR/MIR

In this section, I will first introduce the stellar model by Cordier et al. (2007) and explain which stellar age template was used for the three morphological components. I will further describe how the stellar template is convolved with approximated filter functions for 2MASS, IRAC and MIPS and how the model is finally fitted to the SEDs. The effect of the parameters 'metallicity of the stellar model' and 'optical depth' will be discussed as well.

4.2.2.1 Single Age Stellar Population Model for Bulge and Halo

Sophisticated population synthesis (PS) models as introduced by Cordier et al. (2007), which is the model used here, or by other authors such as Bruzual & Charlot (2003), employ evolutionary tracks and isochrones (i.e. lines in the Hertzsprung-Russell diagram occupied by stars of different masses and colors but the same age) to develop a model of stellar spectra for different ages and metallicities and extended their templates beyond 10μm assuming a Rayleigh-Jeans-law. They derive single age templates with a distribution of stellar masses between $0.1M_\odot$ and $120M_\odot$. The templates offer sets for several metallicities (see Sect. 4.2.3.3). Single age stellar population (SSP) models, in which all star formation (SF) has occurred at one epoch in the past, is appropriate for the bulge and the halo, which have little to no ongoing SF.

The question, which of the SSP templates, i.e. which age, should be used for the bulge and the halo was rather easy to answer. Fig. 4.2 shows the color of the SSP templates and compares it with the color range of the data due to the uncertainties. Besides a few SSP templates for young stars, the data is not able to resolve the fine difference, i.e. I cannot discriminate between the models. Apart from the amplitude, the difference in the SSP templates for old stars are smaller than the data error. Therefore, the choice of the SSP is not critical to this work. I use an SSP template of 7Gyrs for the bulge and the halo component, assuming an old, single burst stellar population and the effect of possibly different stellar ages between 3.5Gyr and 15Gyr is accounted for in the error bar (see Fig. 4.3).

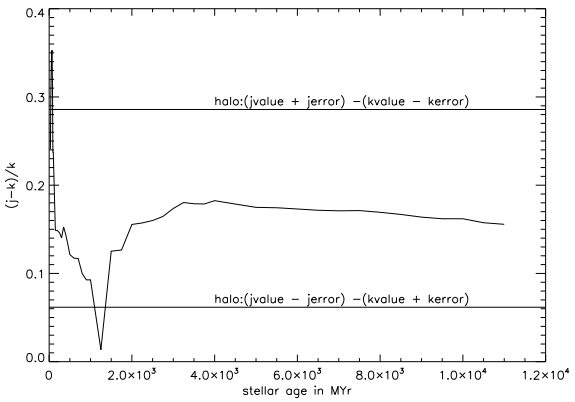

Figure 4.2: J-K Color of Single Stellar Population vs Age
This plot shows the NIR color of the SSP templates for different stellar ages. A comparison of the color interval of the halo admitted by the SED errors and the color range of the templates shows clearly that it is not possible to determine the age of the halo stellar population on the bases of the measured NIR colors.

An important element of the predictions from the stellar SED is the behavior of the starlight in the beyond 10μm. Kraemer et al. (2002) observed 900 Milky Way stars in the range from 2.4 to 45.2μm and analyzed and classified their spectra. Their results for naked stars, i.e. without dust shells, agree with the Rayleigh-Jeans-law assumed in the SSP templates for $\lambda \leq 10\mu$m (see their figures for stellar spectra of different dust shells and emission lines). It is important to note that even though the SSP templates include pure stellar light of AGB stars, they do not include the according circumstellar dust shells.

4.2.2.2 Population Synthesis Model for the Disk

Since disks have ongoing star formation, contrary to the halo and the bulge, the disk is assumed to have a continuous star forming rate (SFR) which is exponentially increasing going back with time. I assumed a galaxy age of 10 Gyr, following Gonzalez (1993). The SFR is therefore defined as

$$SFR(t) = SFR(t=0) * e^{\frac{t}{t_{\rm exp}}}$$

where t=0 is today,$t_{\rm exp}$ =5Gyr the decay timescale and t runs from 0 to 10Gyr.

4.2.2.3 Stellar Model Seen through the Band Filter

The example of two SSP templates age 1.75Gyr and 7Gyr is shown in Fig. 4.3. In order to compare the SSP template with the data SED, I convolved the stellar emission template SEDs with a top-hat function in the range of the data bands (see Tab. 2.1, horizontal lines in Fig. 4.3) as an approximation of the filter response function. The error of the model values in each band is derived from the total flux difference of the different ages (between 1.Gyr and 3.5Gyr for the SSP template age 1.75Gyr and between 3.5Gyr and 15Gyr for the SSP template of 7Gyr). Since the true filter function[2] is not a top-hat function (see Hora et al. (2008)), the quoted frequencies may be not exactly in the middle of the band. In case of the 24μm band, there were not enough sampling points of the template in the band range. Therefore, a value was interpolated from the neighboring model points at 20μm and 40μm, assuming a Raleigh-Jeans decay (λ^{-2}).

The comparison of the SSP SEDs of different age (vertical bars) shows clearly that the general infrared profile does not change within the older age range and only slightly

[2]response function for 2MASS data: http://web.ipac.caltech.edu/staff/waw/2mass/opt_cal/index.html#s10

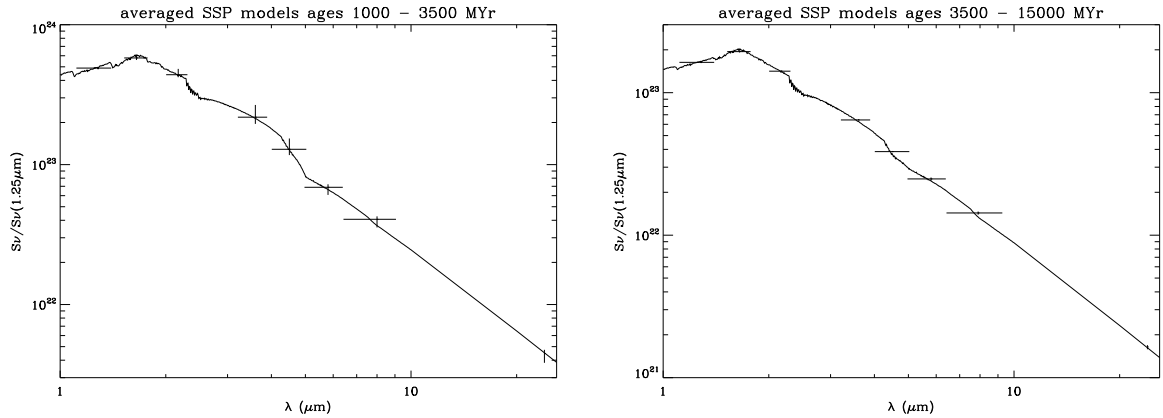

Figure 4.3: Deriving stellar SED from SSP Model
The plots show the example of two SSP model SEDs, age 1750Myr (left) and 7000Myr (right). They are averaged over the range of the 2MASS and IRAC filter functions (horizontal bars). The value for the MIPS filter was interpolated from the neighboring SED points (see text). The vertical bars are the difference in the SSP model SEDs within the age range of 1000 to 3500Myr (left) and 3500 to 15000Myr (right), which were normalized to the 1.25μm emission.

within the younger age range. Therefore, a single older age SED (namely 7Gyr) was chosen to represent the old stellar population for the bulge and the disk.

Color corrections for the stellar light are not necessary, since the correction factors are between 0.5%-1% (see Tab. 5.3 in Wainscoat et al. (1989)). The uncertainty due to the unknown optical depth of the disk or the error of the SED values (see Tab. 3.5) dominate.

4.2.3 Subtraction of the Synthetic Stellar SED from Observed SEDs

In this section, I will first explain the determination of amplitude of the stellar model. Then I will discuss the influence of the optical depths chosen for the disk and the metallicity of the stellar model on the residual SEDs.

4.2.3.1 Fitting the Model Amplitude of the Stellar Model

The SED (Fig. 4.1) consists of an unknown component dominating the long wavelengths and a stellar component dominating the shorter wavelengths. In case of the disk, the 'unknown' component is normally identified with the emission from interstellar dust, which has a negligible amplitude in the three shortest wavelengths (i.e. 1.25μm, 1.65μm and 2.17μm). Therefore, it is favorable to use only the 2MASS bands to constrain the amplitude of the stellar model for the halo, the bulge and the disk.

The amplitude is calculated analytically by minimizing a χ^2 function (see Appendix A.1), summed over the considered wavelengths; the amplitude's error is derived using the Fisher matrix:

$$\chi^2 = \sum_i \left(\frac{A \cdot SSP(i) - data(i)}{\sigma_{\mathrm{data}}(i)} \right)^2 \quad \wedge \quad \frac{\partial \chi^2}{\partial A} = 0 \quad \Rightarrow \quad A = \frac{\sum_i \frac{SSP(i) \cdot data(i)}{\sigma_{\mathrm{data}}(i)^2}}{\sum_i \frac{SSP(i)^2}{\sigma_{\mathrm{data}}(i)^2}} \quad (4.3)$$

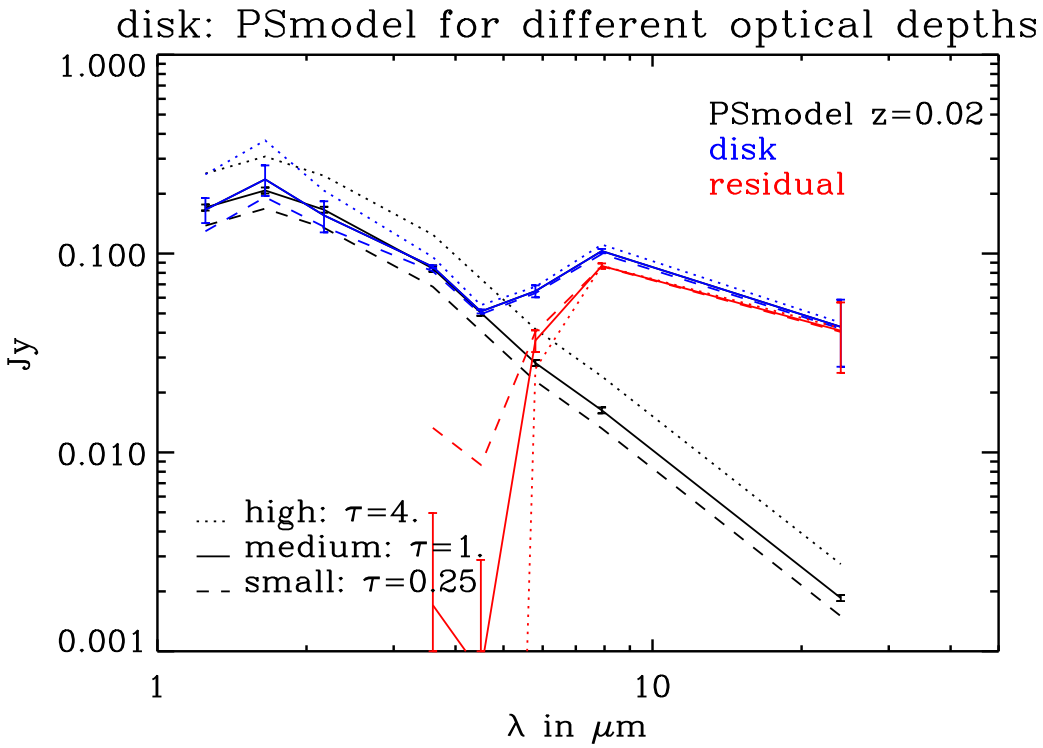

Figure 4.4: Decomposition of Disk SED for Different Trial Disk Optical Depths
Original data, corrected for dust attenuation for $\tau = 1.0$, are shown as the 8 blue points, together with their 1σ uncertainties. The dashed, solid and dotted blue lines represent the observed total disk SED corrected for dust attenuation assuming $\tau = 0.25$,$\tau = 1.0$ and $\tau = 4.0$ respectively. The corresponding black lines represent the predicted SEDs of direct stellar light calculated using the population synthesis model for solar metallicity ($z = 0.02$), which best fits the dust-corrected J, H & K band measurements for the 3 trial optical depths; here the error bars denote the uncertainty in the fitted level of the model SED. The red points are the residual for the $\tau = 1.0$ case, obtained by subtracting the black PS model points from the blue data points; the error bar s represent the propagated errors from both data and model. The dashed, solid and dotted red lines are the derived SEDs from the residual emission for the cases $\tau = 0.25$,$\tau = 1.0$ and $\tau = 4.0$ respectively.

$$\sigma^2_{\text{amplitude}} = -\frac{1}{2} \cdot \left(-\frac{\partial^2 \chi^2}{\partial A^2} \right)^{-1} = \frac{1}{2} \cdot \left(\frac{1}{2 \cdot \sum_i \frac{SSP(i)^2}{\sigma_{\text{data}}(i)^2}} \right)$$

where A is the amplitude, SSP is the filter convolved stellar model used for the morphological component, *data* is the derived SED of the morphological component and σ_{data} the random error of the derived SED. The total uncertainty of the stellar model contains the amplitude error and the uncertainty coming from the unknown stellar age (in case of the bulge and the halo).

$$\sigma_{\text{star}} = \sqrt{\sigma^2_{\text{amplitude}} + \sigma^2_{\text{age}}}$$

4.2.3.2 Influence of the Assumed Disk Optical Depths on the Residual SEDs

As described in Sect. 4.2.1, the galaxy emission is attenuated by the dust present in the disk. Depending on the amount of dust in the line of sight, i.e the optical depths

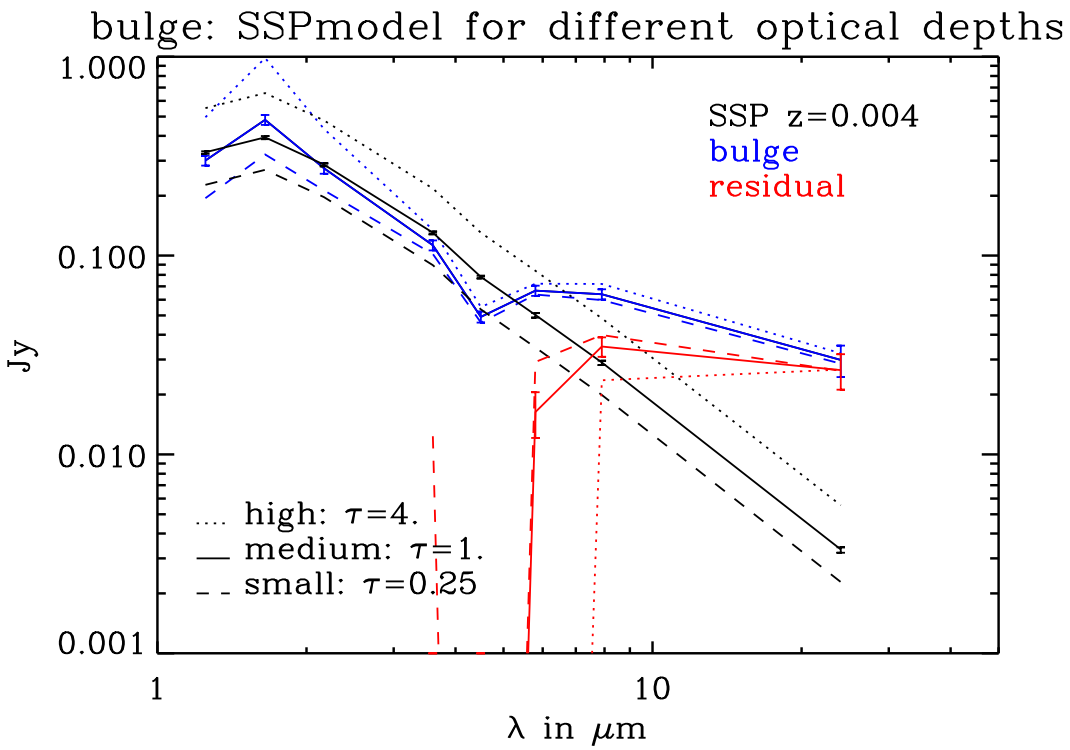

Figure 4.5: Decomposition of Bulge SED for Different Trial Disk Optical Depths
Same as Fig. 4.4, but for the bulge. Here the stellar model used is a single age stellar population (SSP) model with low metallicity z=0.004.

τ, the correction for this attenuation is different, i.e. higher optical depths cause larger the dust attenuation correction. Since shorter wavelengths have a larger correction than longer ones, changing the assumed optical depth τ will slightly change the shape of the attenuation corrected data SED. However, will only change the amplitude of the fitted stellar SED, since that is the only fit parameter.

Fig. 4.4 shows these effects on the disk SED for three different trial values for the optical depths. The blue dashed, solid and dotted lines represent the attenuation corrected data for optical depths values of $\tau = 0.25$,$\tau = 1.0$ and $\tau = 4.0$ respectively. The blue error bars indicate the uncertainties of the attenuation corrected data for $\tau = 1.0$. The corresponding PS models (solar metallicity, z=0.02, see following section) are in black in the same linestyle. The error bars on the PS model for $\tau = 1.0$ show the uncertainty in the amplitude fit of the model. The red lines are the residuals, obtained by subtracting the SP model from the data. The error bars represent the propagated errors from the SPmodel and the data for $\tau = 1.0$.

It is easy to see that the attenuation-corrected data has higher values at the 1.25μm, 1.65μm and 2.17μm wavelengths for high optical depths. The attenuation correction for the long wavelengths is small for all trial values of τ. Therefore, if the trial value for the optical depth is too high, the fitted stellar model will predict higher values in the 3.6μm and 4.5μm bands than the data has. This can be used to constrain the value used for the optical depth for the disk data, since there is the physical requirement that the residual emission must be positive. While the SPmodel underestimates the stellar disk emission in the 3.6μm and 4.5μm bands for the small optical depths trial value $\tau = 0.25$ (dashed line), it clearly overestimates it for the high value $\tau = 4.0$ (dotted line). The estimate

for the intermediate optical depths of $\tau = 1.0$ (solid lines) agree with the attenuation corrected data, i.e. the residuals in these bands are compatible with Zero. Consequently, I used an optical depths of $\tau = 1$ for the later analysis.

Since NGC 7814 is seen edge-on, the attenuation of the bulge light is dominated by the disk dust in the line of sight. For simplicity and in accordance with the models of Tuffs et al. (2004), I assume that there is no diffuse component of dust associated with the bulge that significantly affects the attenuation of light from the bulge. Therefore, the attenuation of the bulge light is calculated in the later analyzes assuming a disk B-band optical depths of $\tau = 1.0$ as was derived for the disk. Fig. 4.5 is the bulge counterpart to Fig. 4.4. Again, the attenuation corrected data is in blue, the stellar model, here SSP model with low metallicity z=0.04, is in black and the residual in red. As for the disk, the low optical depth causes a too low estimate for the stellar emission in the 3.6μm and 4.5μm bands and the high optical depths causes a too high prediction. The intermediate value of $\tau = 1.0$ gives the best estimate out of these three. However, there is still a slight overestimation of the direct star light.

The halo data is not attenuation corrected. As already mentioned, the halo model was fitted above and below the disk, the resulting template is not affected by dust attenuation in the disk.

4.2.3.3 Influence of the Assumed Metallicity on the Residual SEDs

Apart from the stellar age, the other parameter of the SSP model used to derive a model for the direct stellar light is the metallicity of the stars.

Figures 4.6, 4.7 and 4.8 show the stellar models and the residuals for different three different trial metallicities. The color code is again identical with Fig. 4.4. The dashed, solid and dotted lines represent the trial metallicities z=0.004, z=0.02 (solar metallicity) and z=0.04, respectively. Disk and bulge attenuation corrected data used an optical depth of $\tau = 1$, the halo is not attenuation corrected, see previous section.

The difference caused by the different metallicities is very small for all thee morphological components. Only in the 3.6μm and the 4.5μm bands is this difference larger than the data error and that only slightly. Therefore, the decomposition of the SED is not sensitive to the assumed metallicity of the stellar model.

Fig. 4.9 shows the same analyzes of metallicity and optical depths for the sum of the bulge and the halo. Attenuation correction was only done for the bulge. They agree with the results discussed above.

In the final analysis of the residuals (Fig. 4.10), I use solar metallicity (z=0.02) for the disk. The bulge and the halo are older structures, so I attribute lower metallicities of z=0.004 to them.

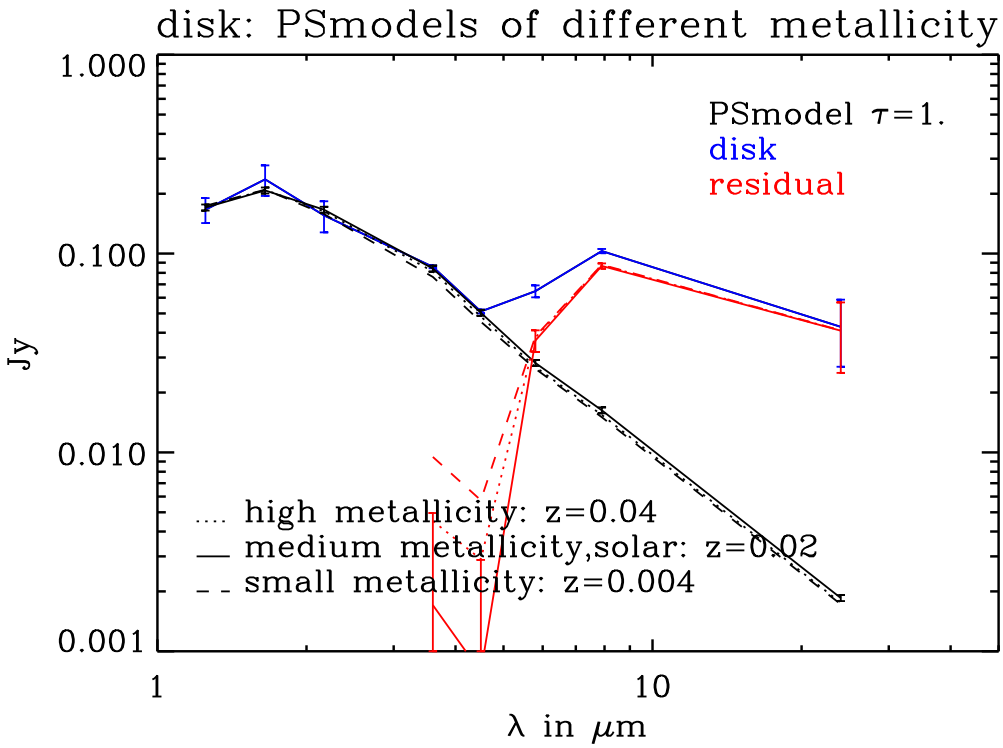

Figure 4.6: Decomposition of Disk SED for Different Trial Metallicities
Fig. 4.6 is the same as Figures 4.4, but the line coding represents the three different trial metallicities used for stellar models: z=0.004, z=0.02 (solar metallicity) and z=0.04. Disk data used an optical depth of $\tau = 1$. The difference caused by the metallicities is larger than the data error only in the 3.6μm and the 4.5μm bands. For details see text.

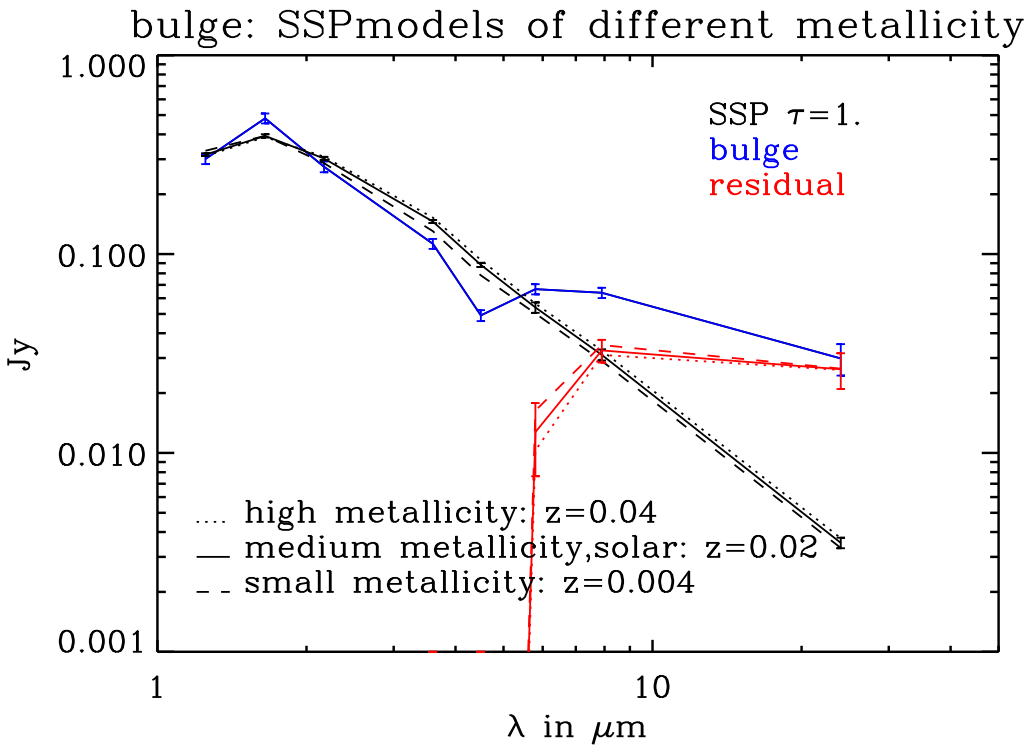

Figure 4.7: Decomposition of Bulge SED for Different Trial Metallicities
Same as Fig. 4.6, but for the bulge.

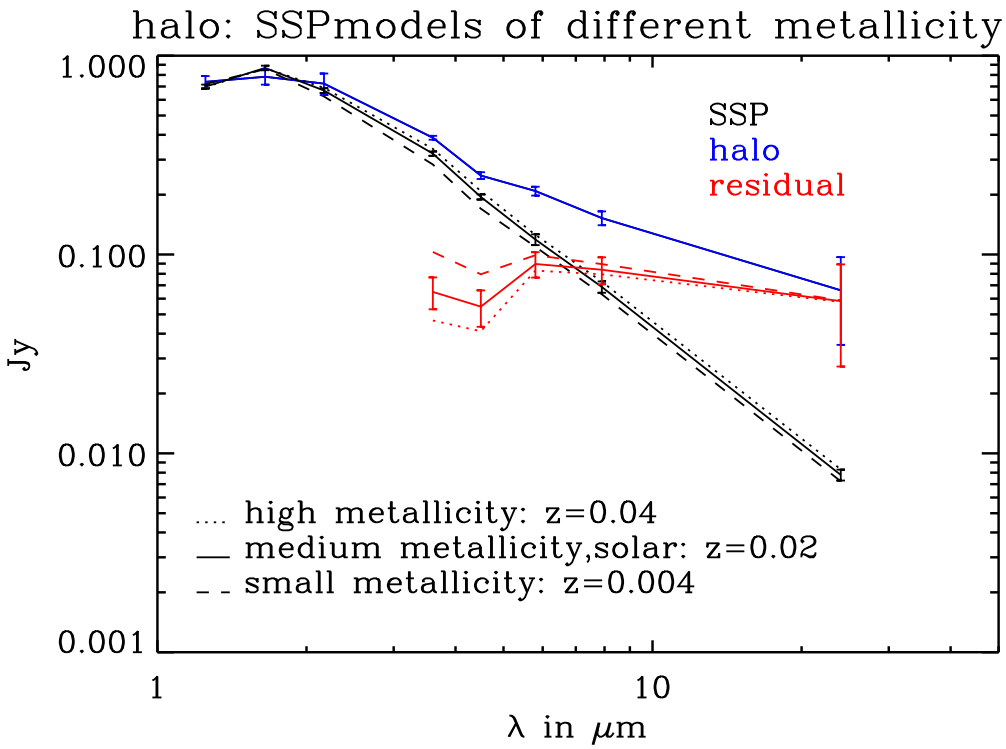

Figure 4.8: Decomposition of Halo SED for Different Trial Metallicities
Same as Fig. 4.6, but for the halo. The halo SED is not attenuation corrected (see text).

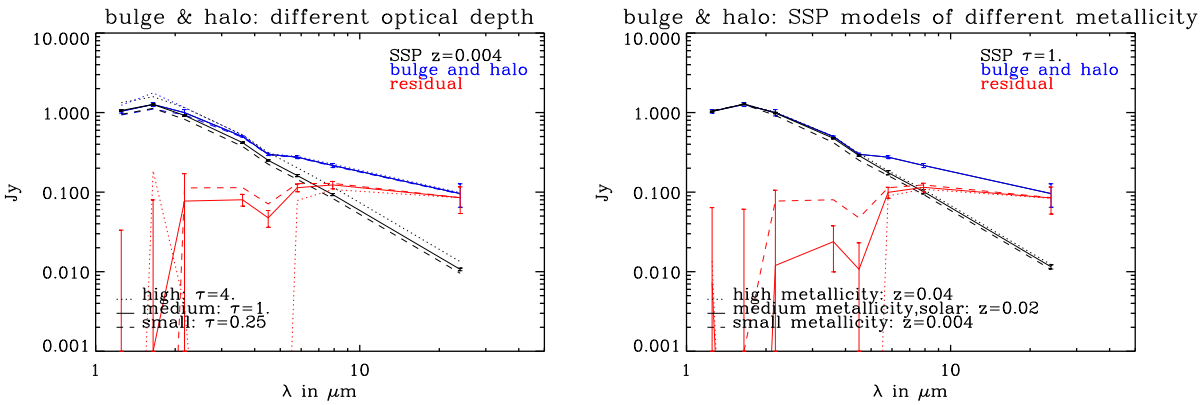

Figure 4.9: Decomposition of the Sum of Bulge and Halo SEDs
Same as Figures 4.5 and 4.7, but for the decomposition of the sum of halo and bulge for different trial disk optical depths (left) and for different trial metallicities (right), respectively. Only the bulge component is attenuation corrected.

4.3 The Residual SEDs

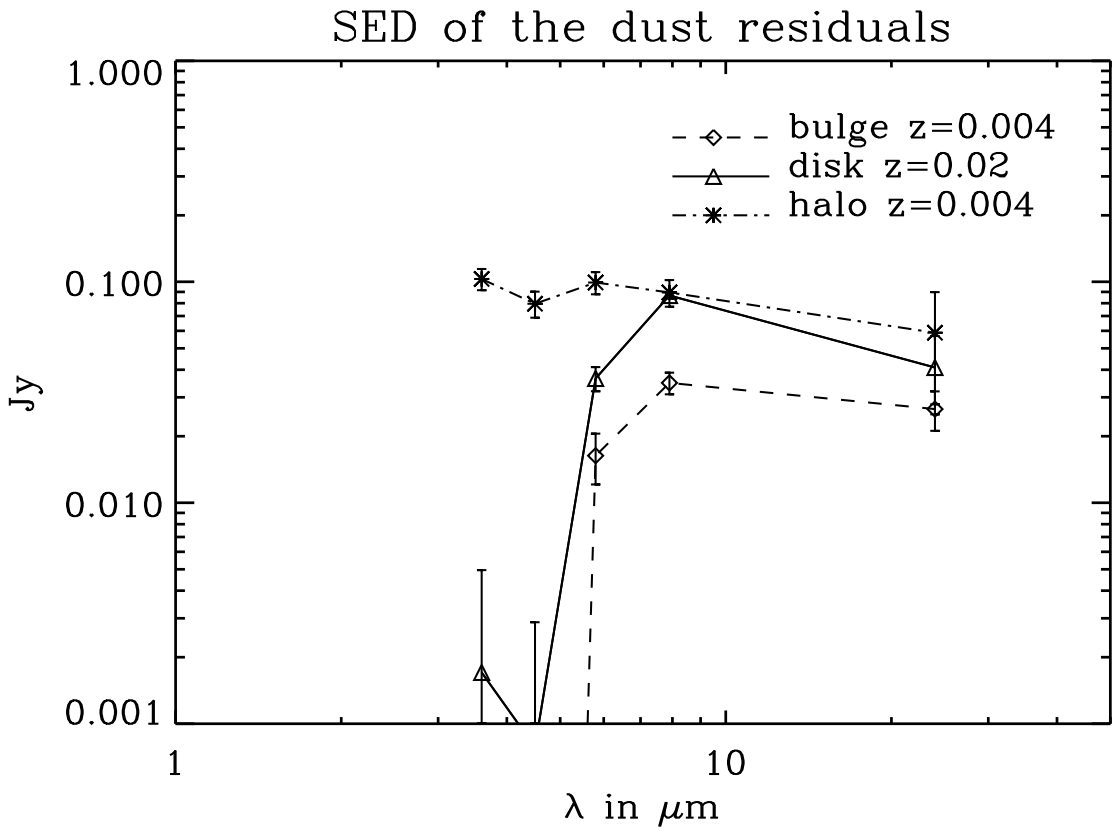

Figure 4.10: Dust Residuals
Comparison of the residuals after stellar model removal (with $\tau = 1$ for the bulge and the disk, solar metallicity z=0.02 for the disk and metallicity z=0.004 for the bulge and the halo): The disk residual emission is between a factor 1.5 and 2 larger than the bulge residual emission. Both have a similar shape with a maximum at 8μm. The halo has a very flat shape in all wavelengths from 3.6μm to 24.μm with residual emission slightly stronger than for the disk.

Fig. 4.10 shows the SED residuals after the subtraction of the predicted emission of the population synthesis models (Sect. 4.2; (using $\tau = 1$ for the bulge and the disk, solar metallicity z=0.02 for the disk and metallicity z=0.004 for the bulge and the halo)) for the halo, bulge and disk.

The disk residual in Fig. 4.10 is consistent with Zero in the short wavelengths up to 4.5μm. The long wavelength bands have significant emission not predicted by the PSmodels, with a maximum in the 8μm band and an only slightly lower emission in the 24μm band.

The bulge residual shows a similar color progression as the disk. The bulge residual SED shows an emission excess in the 5.8μm, 8μm and 24μm bands with a maximum in the 8μm band.The bulge residual emission is roughly a factor two smaller than the disk residual emission.

The halo residual is very flat. Except for the three shortest wavelengths which were used to fit the amplitude of the population synthesis model, all wavelengths show a significant residual emission. This residual is almost constant in all the wavelengths within the errors. For the two longest wavelengths, the halo residual emission is roughly a

Band [μm]	3.6	4.5	5.8	8.0	24.
ratio disk residual / total emission	0.020	0.015	0.565	0.842	0.957
ratio bulge residual / total emission	-0.157	-0.591	0.245	0.546	0.889
ratio halo residual / total emission	0.266	0.319	0.476	0.58	0.890

Table 4.2: Fraction of Residual Emission on the Attenuation-Corrected SEDs
These number are the fraction of the residual emission in the attenuation corrected emission (with $\tau = 1.$) of each morphological component. Negative values indicate an overestimation of the stellar emission in this wavelength.

factor 1.3 stronger than the disk residual emission and a factor 2.4 stronger than the bulge residual emission. All three components have an overall comparable amount of residual MIR emission.

The fractions of the residual emission in the attenuation corrected emission (with $\tau = 1.$) of each morphological component are presented in Table 4.2. Bulge and disk residuals have only small or even negative values, i.e. compatible with zero, in the shorter IRAC bands, therefore their fraction of the data is small. In the longer wavelength, the residuals dominate the data SEDs. The fraction of the halo residuals is much higher in the shorter wavelengths compared to the bulge and disk values, which may be a physical effect or may reflect larger systematic uncertainties due to dust opacity in the estimate of the stellar emission in the SEDs of the bulge and the disk.

I will briefly state the likely origin of the disk residual emission in Sect. 4.3.1. The bulge and halo residuals have uncertain origin. I give a preliminary discussion of potential reasons for these residuals in Sect. 4.3.2.

4.3.1 Origin of the Excess in the SED of the Disk

The residual emission of the disk is caused by interstellar dust. Dust grains in the disk are heated by the radiation field of the surrounding stars and radiate thermally in the MIR and FIR, depending on their temperatures. There have been extensive observational (e.g. Bendo et al. 2008; Muñoz-Mateos et al. 2009) and theoretical studies (e.g. Popescu & Tuffs 2005) of the dust emission from the disk.

Popescu & Tuffs (2010) present synthetic SEDs of galaxies and Fig. 4.11 shows their SEDs for pure disks with various combinations of old and young stellar populations, dust opacities, bulge-to-disk ratios and SFRs. Especially the SEDs for low SFR and $\tau = 1.$ show a similar behavior as the disk residual for NGC 7814. The ratio of IRAS FIR (unresolved) emission is consistent with the model if all the observed FIR emission comes from the disk. The 5.8μm and 8μm bands are dominated by molecular (e.g. polycyclic aromatic hydrogen; PAH) line emission, where the 8μm emission is stronger. The 24μm band is only slightly weaker than the 8μm emission. There is negligible interstellar dust emission at 3.6μm and 4.5μm bands.

4.3.2 Origin of the Excess in the Spectra of Bulge and Halo

In this Section, I will discuss several different potential origins for the excess emission from the bulge and the halo. In the end of this Section, I will give an outlook on desirable future analyzes.

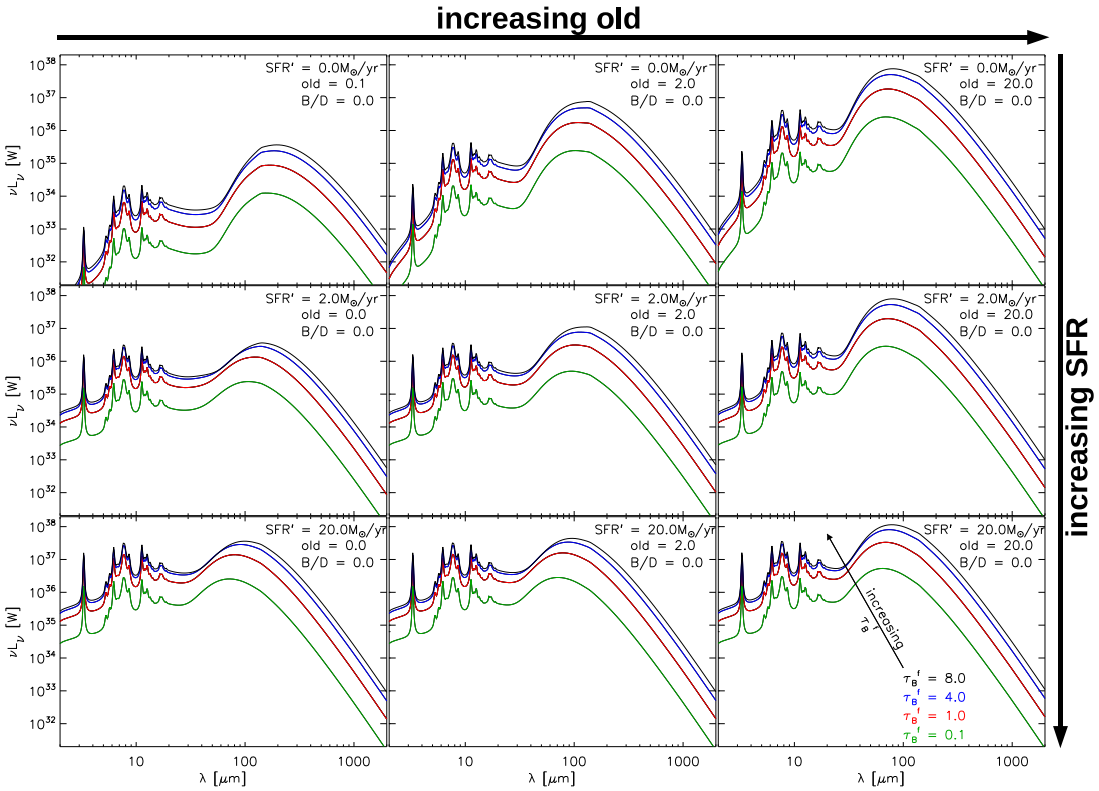

Figure 4.11: SED of Dust Templates for Different Ages and Starforming Rates (taken from Popescu & Tuffs (2010))
Integrated dust and polycyclic aromatic hydrocarbon emission SEDs for model galaxies with different face-on opacities (plotted as different curves in each panel). All models shown in this figure are for pure disk galaxies. From left to right the panels show model galaxies with various levels of contribution from the old stellar populations (old = 0.1 (0.0), old = 2.0 and old = 20.0). From top to bottom the panels show models with various levels of SFR (SFR = 0.0, 2.0, 20.0 $M_\odot$/yr). The color coding is as follows: green is for $\tau_B^f = 0.1$, red is for $\tau_B^f = 1.0$, blue is for $\tau_B^f = 4.0$ and black is for $\tau_B^f = 8.0$.

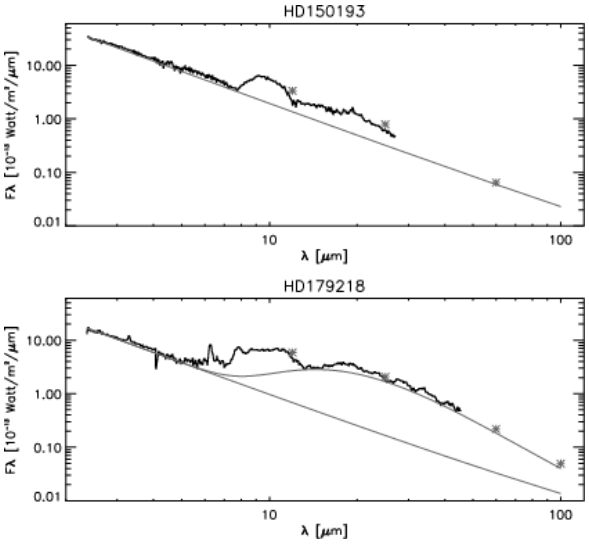

Figure 4.12: Stellar Spectra of two Pre-Main Sequence Stars with Circumstellar Dust
These two spectra are taken from Meeus et al. (2001). They show the spectra of a Herbig B (top) and Herbig n A (bottom) star (i.e. pre-main sequence) taken by ISO Short Wavelength Spectrometer (solid line), with a power-law continuum fit (straight grey line) and a sum of a power-law continuum ans a blackbody (T $\simeq$ 190K; curved grey line in bottom spectrum). The asterisks are color-corrected IRAS fluxes.

4.3.2.1 AGB Stars & Circumstellar Dust

The excess emission of both bulge and halo SEDs indicates the presence of an emission component which is not predicted by the population synthesis model. As described in Sect. 4.2, the stellar model used assumes a Rayleigh-Jeans-law in the MIR. However, very young massive stars (Meeus et al. 2001) and AGB stars (Gail et al. 2009) can have circumstellar dust, which changes the spectra significantly. The former is still embedded in the gas-dust envelopes they formed of. In case of the later, gas is blown out of the star and cools down. Dust grains can condense, which will still be heated, but not vaporized by the parent star. These stars have a much shallower spectral slope than stars without circumstellar dust due to the thermal and molecular dust emission in the MIR and FIR wavelengths. This spectral behavior might agree better with the deduced halo SED than the dust-free stellar model used, which might indicate the need to include circumstellar dust emission in these models. On the other hand, the AGB stars spend most of their lifetime in the Main Sequence and only a small fraction on the AGB. Therefore, their overall contribution to the galaxy emission could be less than the contribution of Main Sequence stars. Massive AGB form from relatively young and massive stars, which have only a short lifetime (typically 1-3 Gyrs). If the excess emission comes from these massive stars, they must have been formed recently in the halo or bulge, or must have been added to the halo or bulge in the course of merger activity with small star-forming galaxies. This is not contradictory with the lack of ongoing star formation on timescales of a few hundred Myr (Eskridge et al. (2002); Hα image see Hameed & Devereux (2005)).

The multiwavelength analysis described in Sect. 3.3 for the halo and in Sect. 3.4.2 for the bulge and the disk found a similar geometrical shape of the halo and bulge emission at all wavelengths. Since circumstellar dust follows the stellar distribution, this similar shape supports the hypothesis of the MIR excess having this origin. This assumption could be tested with FIR data. If the halo SED is dominated by AGBs, the slope observed in the MIR would continue towards longer wavelengths and the FIR emission would be significantly smaller than the MIR emission. No strong emission of cold dust in FIR wavelengths would be expected. However, no FIR images with a resolution high enough for a bulge-halo-disk decomposition are available.

4.3.2.2 Interstellar Dust

Apart from circumstellar dust, another possible source of the MIR emission excess is interstellar dust. As I have already mentioned, this is commonly assumed to be the dominant MIR source in galaxies' disks. Dust grains in the interstellar medium (ISM) are heated by the radiation fields of the surrounding stars and radiate thermally. Typical equilibrium temperatures of grains are 15-30K (e.g. Popescu et al. (2000a)), depending on their position in the disk. However, small grains are heated stochastically and are not in an thermal equilibrium. The energy portion transfered by an UV photon is large enough to heat the grain to high temperatures. This energy will be radiated off and the grain cools until the next photon hits. A small fraction will be hot enough to radiate in the MIR. Line emission of molecules, e.g. PAH, contribute to the dust emission as well. The presence of ISM could be inferred from HI measurements of the bulge and the halo area. Generally, the halo and the bulge are assumed to be dust-free, as they do not contain a cool / warm ISM component. It is this component that carries the large majority of grains in the disk. Even if there were an ISM, a static equilibrium for cool / warm dust at large scale heights of the halo would not be expected.

Even if there were an ISM in the halo or the bulge, the radiation field is weaker than in the disk and is not be intense enough to power significant radiation in the MIR (e.g. Popescu et al. (2000a)). A halo-bulge-disk decomposition of FIR data would be able to rule out or support this hypothesis. If the MIR came from warm grains in the interstellar dust, then the cold grains would radiate in the FIR and a large emission would be expected in these bands.

In case of the bulge, there is another possibility, how interstellar dust can be the source of the MIR excess. The bulge of NGC 7814 is almost completely embedded in the disk and therefore in the ISM of the disk. The additional radiation from the bulge stars increases the local radiation field and thereby enhances the thermal radiation of the dust grains in the disk. My bulge-disk decomposition (see Sect. 3.4.2) determines the disk shape and emissivity in the outer regions of the disk, where the bulge does not contribute to the detected emission. Therefore, it is not able to distinguish on the basis of the 1D profiles between MIR disk emission caused by the bulge radiation field and MIR bulge emission itself. Since the spectral shape of the residual emission is the same for the disk and the bulge (Fig. 4.10), warm interstellar dust in the disk is a possible source of the MIR radiation in the bulge. However, the evidence for a vertical extension of the MIR emission for the bulge, even at 24 μm (see Sect. 3.5), argues that not all the excess emission may be attributed to dust in the plane of the galaxy. There may be dust extended in z above the plane in the bulge.

4.3.2.3 Localized Star Formation in Galactic Fountains and Galactic Winds

Ejections of hot gas from the disk into a galaxy's halo are called galactic fountains and can be seen even at large heights. The hot gas might contain dust grains which will be dragged along. If the gas cool enough, even star formation is possible.

However, these gas clumps come from the galactic plane and eventually will fall back into it due to the disk potential. Their spatial distribution will not fill the whole halo and will especially not follow the stellar distribution in the halo. The additional IR signal would be rather flat above and below the galactic plane. Howk & Savage (2000) detected individual dust bearing clouds up to heights $\sim$ 2kpc above the mid plane in the edge-on galaxy NGC 891. Nevertheless, the Hα image presented by Hameed & Devereux (2005) does not show any Hα emission above or below the disk of NGC 7814. Moreover, even if NGC 7814 had such dust bearing clouds up to the same hight, it would have barely influenced the halo fit, since it did not fit the area below 1.6kpc above the mid plane (see Sect. 3.3.1). Therefore, SFregions from galactic fountains or dust bearing clouds are not accountable for the MIR excess in the halo. The bulge's MIR excess might partially come from this source if the galactic fountains occur in the central bulge region, though the lack of an in situ Hα emission from associated star formation would argue against this.

The same geometrical arguments hold for galactic winds. These winds are hot gas which is blown out the galaxy due to thermal and cosmic ray pressure, which might contain to dust (see e.g. Popescu et al. 2000b). Inelastic collisions between the grains and the plasma particles supply the thermal pressure driving the wind. In these collisions, the grains can be heated as well as destroyed. If gas was blown from the disk into the halo, one would see a very flat distribution around the disk, and not a rather round structure which has the same spatial distribution as the halo stars (Popescu et al. 2000a). The plasma in a wind could be detected in X-ray images of the galaxy. However, this galaxy

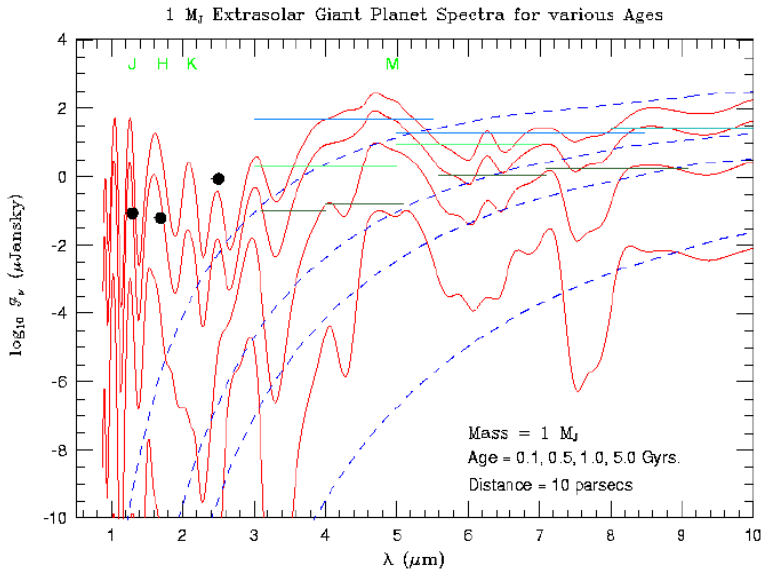

Figure 4.13: SED of a Jupiter-mass Planet (taken from Burrows et al. (2001))
The flux (in μJy) vs wavelength (in μm) from 1.0 to 10 μm for a Jupiter-mass giant planet in isolation at various epochs (0.1, 0.5, 1.0, and 5.0 Gyr) during its evolution. These spectra are compared with the corresponding blackbodies (dashed blue), with T_{eff}'s of 290, 190, 160, and 103 K. Superposed are the approximate sensitivities of NICMOS (black dots; Thompson, 1992), SIRTF (olive lines; Erickson 1992), and Gemini/SOFIA (light green/solid blue; Mountain, Kurz, and Oschman, 1994). A distance of 10 parsecs is assumed. The positions of the J, H, K, and M bands are indicated at the top. For all epochs, the super-blackbody excess at suitably short wavelengths is always large [Colors].

was not seen by ROSAT, i.e. it is not a luminous source in the soft X-ray wavelengths. No soft X-ray data of this galaxy is available (Halderson et al. 2001). A wind explanation of the halo is therefore unlikely.

4.3.2.4 Brown Dwarfs and Jupiters

I removed the stellar component of the galaxy's SED using an SSP model described in Sect. 4.2. Substellar objects, such as brown dwarfs or giant planets ("Jupiters") were not considered in this model.

Young brown dwarfs (for general review see e.g. Burrows et al. (2001) and Burrows & Liebert (1993)) have effective temperatures up to 3500K. They are heated by deuterium fusion, but are not massive enough to start hydrogen burning. For the MIR wavelengths, their spectra look just like the SSP model, since their black body curve peaks at less than 1μm and the longer wavelengths obey the Rayleigh-Jeans law. The contribution of these objects would therefore have been subtracted during the starlight removal step.

Older brown dwarfs cool down as the deuterium in their core is depleted and the fusion stops. Their spectra slowly develop towards the spectra of giant planets, which can have effective temperatures as low as 125K (Jupiter). Fig. 4.13 shows theoretical spectra of a Jupiter-mass planet for different ages and effective temperatures taken from Burrows et al. (2001). The spectra are slightly flatter than the corresponding black body curves, which peak at wavelengths of 10μm or longer.

The Jupiter-mass planet spectra look similar to the starlight removed residuals of the

halo SED (cf. Fig. 4.10). Planets with a few Jupiter masses would be hotter and would peak at slightly shorter wavelengths as the planets shown in Fig. 4.13. On the base of their spectral shape, these objects are good candidates to produce the MIR excess of the halo emission.

However, low-mass objects have a very small luminosity. The mass-luminosity ration ($L \sim M^{3.5}$) holds only for main sequence stars. However, it gives an upper limit for the radiation of substellar objects. Assuming a number density of substellar objects to be equal to the stellar number density, i.e. a mass density of about 10% of the stellar mass density (Chabrier (2002) for the Galactic disk), the intensity of the emission from brown dwarfs and giant planets is far too low to account for the MIR excess in the halo emission.

4.3.3 Summary of Possible MIR Emission Sources and Outlook for Future Investigations

In case of the disk, the source of the MIR emission was considered beforehand to be thermal radiation of interstellar dust. In case of the bulge, the most promising candidate is dust, either or both interstellar and circumstellar. However, it is not possible to say from the 1D profiles, whether it is interstellar dust in the bulge itself or just additional thermal radiation of the dust in the disk stimulated by the stellar emission of the bulge.

There are several candidates for the MIR source in the halo. The promising candidates are circumstellar dust shell, interstellar dust and substellar objects. Which one contributes how much must be analyzed with further data in the FIR, X-Ray and HI. This analysis, however, is beyond the scope of this thesis, and in any case data with the necessary resolution is unavailable.

There are four additional investigations which should be made in the future. Firstly, in addition to the investigations mentioned above, it would be necessary to examine the statistics of stars with excess MIR emission in high resolution MIR surveys of the Milky Way thick disk and halo in order to place constrains on the fraction of the MIR emission from these components which can be attributed to circumstellar dust.

Secondly, it would be useful to incorporate observational knowledge of the incidence and amplitude of circumstellar dust emission as a function of stellar type and age into the population synthesis model. This information is already available from MIR observations of Spitzer, both for dust produced in stellar winds, as in AGB stars, and for interstellar and interplanetary dust originated from debris disks left from the formation of the star. Such models could then be used to test the circumstellar dust hypothesis more quantitatively.

Thirdly, it is clear that similar analyzes, as done for NGC 7814 in this thesis, should be made for other galaxies. Such analyzes should in the future be extended to the FIR, using Herschel Space Observatory, which has a comparable angular resolution in the FIR to the angular resolution of Spitzer at 24 μm. Measurements at these wavelengths would be able to put constraints on the dust mass in a morphological component, on the dust's spatial distribution (i.e. circumstellar or interstellar) and the grain sizes. Since I have found a relatively large fraction of the integrated MIR emission of NGC 7814 in the bulge and the halo, it would be useful to find statistical evidence for the same phenomena from observations of the spatially integrated MIR emission from a large sample of disk galaxies identified to have prominent bulges and / or halos.

Chapter 5

Summary

The galaxy data in eight wavelengths ranging from 1.25μm to 24μm were cleared from foreground stars and zodiacal light. A morphological template of a Sersic profile was fitted to the aligned images in order to identify the halo emission. The remaining galaxy emission was collapsed to 1D and a combination of 1D Sersic profiles for bulge and disk was fitted to the data. All morphological components have been reliably detected in all wavelengths. From the 1D profiles of the bulge and the disk, a 2D reconstruction of the galaxy was derived and compared with the original data.

Using the morphological templates for halo, bulge and disk, SEDs for each component were presented. The bulge and the disk had similar bimodal shapes in the SED, the halo was much brighter with only a single peak in the 1.65 μm band.

The stellar light in the SEDs was identified and subtracted, using the SSP model introduced by Cordier et al. (2007). The emission residuals were analyzed and possible sources discussed. The disk's residual emission is known to be caused by interstellar dust heated by the radiation field of the disk's stars. The bulge's residual might be caused as well by the interstellar dust of the disk which is heated even more in the bulge region due to the stronger radiation field of stars. However, other sources such as circumstellar or interstellar dust, or substellar objects are possible. The true sources for the halo's residual are still uncertain. Good candidates are substellar objects and AGBs with circumstellar dust. Interstellar dust as MIR source cannot be ruled out either, but seems unlikely, as there is no evidence from available data for an ISM associated with the halo.

Chapter 6

Glossary

2MASS	= 2μm All Sky Survey
AGB	= Asymptotic Giant Branch
FIR	= Far Infrared (30-300μm)
FWHM	= Full Width at Half Maximum
IRAC	= Infrared Array Camera on the Spitzer Space Telescope
IRAS	= Infrared Astronomical Satellite
ISM	= Interstellar Medium
ISO	= Infrared Space Observatory
MIPS	= Multiband Imaging Photometer for Spitzer
MIR	= Mid Infrared (3-30μm)
NIR	= Near Infrared (1-3μm)
PAH	= Polycyclic Aromatic Hydrocarbon
PS	= Population Synthesis
PSF	= Point-Spread Function
SED	= Spectral Energy Distribution
SSP	= Single Stellar Population
SFR	= Star Forming Region or Star Forming Rate
S/N	= Signal to Noise Ratio

Appendix A

Theoretical Background About Modelling Data

In this section, I introduce the theoretical background of the fitting methods which optimize the least squares problem. I will first introduce the general concept of maximum likelihood estimation (Sect. A.1) and then explain how the parameter errors can be estimated (Sect. A.2). In Sect. A.3, I will then briefly discuss the problem of how to decide which actual model (rather than parameter set of a single model) best represents the data.

A.1 Maximum Likelihood Parameter Estimation

A good way to find the parameter set of a model for specific data is to use the maximum likelihood estimation (e.g. Barlow (1989); Hastie et al. (2008)).

For each model, there is a pool of the different parameter sets $\vec{p}$, which includes all valid parameter combinations. Instead of asking for the most likely parameter set $\vec{p}$ out of this pool for specific data $\vec{y}$ (i.e. $\mathrm{P}(\vec{p}|\vec{y})$), one can ask which parameter set of a model has the highest probability to produce this data ($\mathrm{P}(\vec{y}|\vec{p})$). Bayes theorem states

$$P(A|B) = \frac{P(B|A) \cdot P(A)}{P(B)} \qquad \text{in our case} \qquad P(\vec{p}|\vec{y}) = \frac{P(\vec{y}|\vec{p}) \cdot P(\vec{p})}{P(\vec{y})} \tag{A.1}$$

The probability of the data $\mathrm{P}(\vec{y})$ is a normalization constant and can be set to 1 during the maximization of $\mathrm{P}(\vec{p}|\vec{y})$. Assuming no prior knowledge about the probability of a parameter set $\mathrm{P}(\vec{p})$, or just a 0 or 1 distribution to indicate "forbidden" and "allowed" parameter sets, it is the same to maximize $\mathrm{P}(\vec{p}|\vec{y})$ or $\mathrm{P}(\vec{y}|\vec{p})$. The probability of the data, given the parameter set, is called likelihood. In case of identically distributed "measurements" (i.e. pixel in this case), the likelihood of the whole data can be considered as the product of the individual pixel probabilities. Assuming Gaussian noise, the likelihood is then defined as

$$\mathrm{lik} = \frac{1}{(2\pi)^{d/2}\sqrt{\det \Sigma}} e^{-\frac{1}{2}(\vec{y}-\vec{f}(\vec{x},\vec{p}))^T \cdot \mathbf{\Sigma^{-1}} \cdot (\vec{y}-\vec{f}(\vec{x},\vec{p}))} \tag{A.2}$$

where $\vec{f}(\vec{x},\vec{p})$ the corresponding model value vector at the position vector $\vec{x}$ for the parameter vector $\vec{p}$. $\mathbf{\Sigma}$ is the pixel covariance matrix, containing the pixel variances (i.e. σ_n^2) on the diagonal elements and covariances of the pixel on the off-diagonal elements.

In case of uncorrelated noise, the off-diagonal elements are Zero. The likelihood then simplifies to

$$\text{lik} = \frac{1}{(2\pi)^{d/2}\sqrt{\det \Sigma}} e^{-\sum_n^{\mathbf{N}} \frac{1}{2}(y_n - f_n(x_n,\vec{p}))\cdot(\mathbf{\Sigma^{-1}})_{nn}\cdot(y_n - f_n(x_n,\vec{p}))} \tag{A.3}$$

$$= \prod_n^{\mathbf{N}} \frac{1}{(2\pi)^{d/2}\sqrt{\det \Sigma}} e^{-\frac{(y_n - f_n(x_n,\vec{p}))^2}{2\sigma_n^2}} \tag{A.4}$$

For simplicity reasons, the log likelihood is generally considered rather than the likelihood directly.

$$\text{loglik} = \sum_{n=1}^{\mathbf{N}} -\frac{(y_n - f_n(x_n,\vec{p}))^2}{2\sigma_n^2} + const \tag{A.5}$$

$$= -\frac{1}{2}\chi^2 + const \tag{A.6}$$

The parameter set which has the highest probability to produce the measured data is the parameter set, with the lowest χ^2 value. The constant term can be neglected for finding this extremum. Therefore, when I speak of a "fit" or "fitting" in this thesis, I mean the minimum or the procedure to find the minimum of this score-function χ^2.

A.2 Error Estimation

The standard method to derive the parameter errors of a model for data with Gaussian noise is the Fisher matrix (for further detail see e.g. Barlow (1989)). In case of independence and identical distribution of the individual measurements (i.e. pixel), this matrix is derived using the second partial derivatives of the logarithmic likelihood function.

In this case, the log likelihood is a Gaussian as derived above and the Hess matrix (matrix of the second partial derivatives) of the log likelihood is the negative inverse of the Fisher matrix F (Eq. A.7). Since all likelihoods can be approximated by a Gaussian distribution near the optimal parameter set $\widehat{\vec{p}}$ (Central Limit Theorem), this holds for all distributions. The Fisher matrix has the variance of the parameters (i.e. $\sigma_{p_i}^2$) in the diagonal elements and the covariance in the off-diagonal. Since partial derivatives always commute, it is a symmetric matrix. For a two-dimensional parameter space, the Fisher matrix is

$$F = \begin{pmatrix} \sigma_{p_1}^2 & covar(p_1p_2) \\ covar(p_1p_2) & \sigma_{p_2}^2 \end{pmatrix} = \begin{pmatrix} -\frac{\partial^2 loglik}{\partial^2 p_1} & -\frac{\partial^2 loglik}{\partial p_1 \partial p_2} \\ -\frac{\partial^2 loglik}{\partial p_1 \partial p_2} & -\frac{\partial^2 loglik}{\partial^2 p_2} \end{pmatrix}^{-1}_{\vec{p}=\widehat{\vec{p}}}. \tag{A.7}$$

Essentially, all one has to do in order to get our parameter errors is to derive the loglik twice, invert the matrix, multiply it with (-1) and take the root of the diagonal elements. In case of numerical fit models, a numerical derivative at $\widehat{\vec{p}}$ is possible, too. If the covariance of the parameter is small compared to each variance (i.e. independent parameters), the matrix of the second derivatives can be considered as a diagonal matrix, which can be inverted by inverting its diagonal elements. This is generally not the case.

The correlation ρ_{12} (Eq. A.8) between two parameters indicates the strength and the direction of a linear relationship, i.e. how does the change in parameter i provoke a change

in parameter j. The correlations are caused by the curvature of the χ^2 hypersurface. The values are in the interval [-1,1]. A correlation of +1 implies the same (factorial) change in both parameters. If parameter one decreases by a certain factor and parameter two increases by the same, then the correlation is -1. These correlations can be derived from the Fisher matrix off-diagonal elements with

$$\rho_{12} = corr(p_1, p_2) = \frac{covar(p_1 p_2)}{\sigma^2_{p_1} \cdot \sigma^2_{p_2}} \tag{A.8}$$

The errors of the fit parameter represent the random noise, which causes a limited accuracy of a fit. The error of the model is then derived through Gaussian error propagation.

$$y = y(x_1, x_2, ...) \quad \rightarrow \quad \Delta y = \sqrt{\left(\frac{\partial y}{\partial x_1} \cdot \Delta x_1\right)^2 + \left(\frac{\partial y}{\partial x_2} \cdot \Delta x_2\right)^2 + \cdots} \tag{A.9}$$

Systematic errors are not included in these errors. Systematic errors such as calibration errors are not Gaussian errors and can therefore not be included in error bars.

A.3 Model Assessment

Modeling a resolved galaxy with its components is a challenging task. The difficulty already arises when one is to decide which model to use. It is not easy to compare models with different number of components or with different spatial dimensions . It is obvious that models which lead to lower residuals are preferable over those leading higher residuals. However, models with few parameter are preferable over those with many, even though they are likely to lead to lower residuals. One needs to employ criteria to assess whether one model is better than another.

In case of linear models, the reduced χ^2 (i.e. χ^2 divided by the degree of freedom) provides a theoretically well justified assessment (e.g. Barlow (1989)). The optimal fit has a reduced $\chi^2 = 1$. A reduced $\chi^2 > 1$ is not an optimal fit and a reduced $\chi^2 < 1$ signals overfitting or overestimated data noise.

However, in the nonlinear case, the reduced χ^2 looses this interpretation. A nonlinear model with smaller reduced χ^2 is not necessarily the better model compared with another nonlinear model. Unfortunately, there is no universal method to assess, which nonlinear model fits the data best. There exist only heuristic methods, e.g. the Bayesian information criterion (e.g. Hastie et al. (2008)) or leave-one-out cross validation. In general, a model with more parameters will lead to lower residuals, which does not necessarily imply a better description of the data. Nonetheless, a minimal χ^2 still indicates the best parameter set for a specific model.

For every model used to describe data, there are errors on the derived model parameter due to the noise of the data (see Sect. A.2). Moreover, there are systematic errors, e.g. how good can the model describe the complexity of the data, a bias, etc. , which are usually hard to identify, if at all. A way to derive the parameter errors and from them the model error will be explained in Sect. A.2.

Danksagung

Ich danke Prof. Werner Hofmann für die Betreuung dieser Diplomarbeit und Prof. Klaus Meisenheimer für die Übernahme der Zweitkorrektur.

Des weiteren danke ich Dr. Richard J. Tuffs für die ständige Beratung, hilfreiche Diskussionen und gute Zusammenarbeit, sowie Giovanni Natale für Tipps und Tricks rund um Fit-Routinen und IDL.

Meiner Büronachbarin und Freundin Ioanna Arka danke ich für ihr Talent für Internetrecherchen und dafür, dass sie immer wusste, wann sich Probleme mit einer heißen Schokolade lösen ließen.

Meinen Eltern danke ich für ihre Unterstützung während des gesamten Studiums, sowohl emotional als auch finanziell.

Zum Abschluss möchte ich meinem Freund René Andrae danken. Er unterstützte mich in diesem Jahr nicht nur mit fachlich Diskussionen und Programmiertipps, sondern auch privat mit viel Liebe und Geduld.

Bibliography

Barlow, R. B. 1989, Statistics: A Guide to the Uns of Statistical Methods in the Physical Science (John Wilson & Sons)

Bendo, G. J., Draine, B. T., Engelbracht, C. W., et al. 2008, MNRAS, 389, 629

Bruzual, G. & Charlot, S. 2003, MNRAS, 344, 1000

Burgdorf, M., Ashby, M. L. N., & Williams, R. 2007, ApJ, 668, 918

Burrows, A., Hubbard, W. B., Lunine, J. I., & Liebert, J. 2001, Rev. Mod. Phys., 73, 719

Burrows, A. & Liebert, J. 1993, Reviews of Modern Physics, 65, 301

Chabrier, G. 2002, ApJ, 567, 304

Cordier, D., Pietrinferni, A., Cassisi, S., & Salaris, M. 2007, AJ, 133, 468

Dale, D. A., Bendo, G. J., Engelbracht, C. W., et al. 2005, ApJ, 633, 857

Draine, B. T., Dale, D. A., Bendo, G., et al. 2007, ApJ, 663, 866

Engelbracht, C. W., Blaylock, M., Su, K. Y. L., et al. 2007, PASP, 119, 994

Eskridge, P. B., Frogel, J. A., Pogge, R. W., et al. 2002, ApJS, 143, 73

Fisher, D. B. & Drory, N. 2008, AJ, 136, 773

Fisher, D. B., Drory, N., & Fabricius, M. H. 2009, ApJ, 697, 630

Gail, H.-P., Zhukovska, S. V., Hoppe, P., & Trieloff, M. 2009, ApJ, 698, 1136

Gonzalez, J. 1993, PhD thesis, Univ. Californua, Santa Cruz

Graham, A. W. & Driver, S. P. 2005, Publications of the Astronomical Society of Australia, 22, 118

Halderson, E. L., Moran, E. C., Filippenko, A. V., & Ho, L. C. 2001, AJ, 122, 637

Hameed, S. & Devereux, N. 2005, AJ, 129, 2597

Hastie, T., Tibshirani, R., & Friedman, J. 2008, The Elements of Statistical Learning: Data Mining, Inference, and Prediction (Springer)

Hora, J. L., Carey, S., Surace, J., et al. 2008, PASP, 120, 1233

Howk, J. C. & Savage, B. D. 2000, AJ, 119, 644

Hummel, E., Beck, R., & Dettmar, R.-J. 1991, A&AS, 87, 309

Jensen, J. B., Tonry, J. L., Barris, B. J., et al. 2003, ApJ, 583, 712

Kelsall, T., Weiland, J. L., Franz, B. A., et al. 1998, ApJ, 508, 44

Kent, S. M. 1985, ApJS, 59, 115

Kraemer, K. E., Sloan, G. C., Price, S. D., & Walker, H. J. 2002, ApJS, 140, 389

Larsen, J. A. & Humphreys, R. M. 1994, ApJ, 436, L149

Lequeux, J., Dantel-Fort, M., & Fort, B. 1995, A&A, 296, L13+

MacArthur, L. A., Courteau, S., & Holtzman, J. A. 2003, ApJ, 582, 689

Markwardt, C. B. 2009, ArXiv e-prints

McDonald, M., Courteau, S., & Tully, R. B. 2009, MNRAS, 393, 628

Meeus, G., Waters, L. B. F. M., Bouwman, J., et al. 2001, A&A, 365, 476

Muñoz-Mateos, J. C., Gil de Paz, A., Boissier, S., et al. 2009, ApJ, 701, 1965

Peletier, R. F. & Knapen, J. H. 1992, The Messenger, 70, 57

Popescu, C. C., Misiriotis, A., Kylafis, N. D., Tuffs, R. J., & Fischera, J. 2000a, A&A, 362, 138

Popescu, C. C. & Tuffs, R. J. 2005, in American Institute of Physics Conference Series, Vol. 761, The Spectral Energy Distributions of Gas-Rich Galaxies: Confronting Models with Data, ed. C. C. Popescu & R. J. Tuffs, 155–177

Popescu, C. C. & Tuffs, R. J. 2010, Modeling the spectral energy distribution of galaxies V, in preparation

Popescu, C. C., Tuffs, R. J., Fischera, J., & Völk, H. 2000b, A&A, 354, 480

Saha, K., de Jong, R., & Holwerda, B. 2009, MNRAS, 396, 409

Sauvage, M., Tuffs, R. J., & Popescu, C. C. 2005, Space Science Reviews, 119, 313

Sérsic, J. 1968, Atlas de galaxias australes (Cordoba, Argentina: Observatorio Astronomico)

Sérsic, J. L. 1963, Boletin de la Asociacion Argentina de Astronomia La Plata Argentina, 6, 41

Skrutskie, M. F., Cutri, R. M., Stiening, R., et al. 2006, AJ, 131, 1163

Soifer, B. T., Helou, G., & Werner, M. 2008, ARA&A, 46, 201

Soifer, B. T., Neugebauer, G., & Houck, J. R. 1987, ARA&A, 25, 187

SOM. 2007, Spitzer Observer's Manual, Version 8.0

Temi, P., Brighenti, F., & Mathews, W. G. 2008, ApJ, 672, 244

Terry, J. N., Paturel, G., & Ekholm, T. 2002, A&A, 393, 57

Tonry, J. L., Dressler, A., Blakeslee, J. P., et al. 2001, ApJ, 546, 681

Tuffs, R. J., Popescu, C. C., Völk, H. J., Kylafis, N. D., & Dopita, M. A. 2004, A&A, 419, 821

van der Kruit, P. C. & Searle, L. 1982, A&A, 110, 79

Wainscoat, R. J., Freeman, K. C., & Hyland, A. R. 1989, ApJ, 337, 163

Wainscoat, R. J., Hyland, A. R., & Freeman, K. C. 1990, ApJ, 348, 85

Weingartner, J. C. & Draine, B. T. 2001, ApJ, 548, 296

Wunderlich, E. & Klein, U. 1991, A&AS, 87, 247

Wyse, R. F. G., Gilmore, G., & Franx, M. 1997, ARA&A, 35, 637

Xilouris, E. M., Byun, Y. I., Kylafis, N. D., Paleologou, E. V., & Papamastorakis, J. 1999, A&A, 344, 868

Erklärung

Ich versichere, dass ich diese Arbeit selbständig verfasst und keine anderen als die angegebenen Quellen und Hilfsmittel benutzt habe.

Heidelberg, den September 28, 2009